AFRL-PR-WP-TR-2006-2189

MAGNETIC META-MATERIALS FOR ELECTROMAGNETIC APPLICATIONS

George C. Hadjipanayis

University of Delaware
Department of Physics and Astronomy
Newark, DE 19716

JUNE 2006

Final Report for 19 June 2001 – 19 May 2005

Approved for public release; distribution is unlimited.

STINFO COPY

PROPULSION DIRECTORATE
AIR FORCE MATERIEL COMMAND
AIR FORCE RESEARCH LABORATORY
WRIGHT-PATTERSON AIR FORCE BASE, OH 45433-7251

NOTICE

Using Government drawings, specifications, or other data included in this document for any purpose other than Government procurement does not in any way obligate the U.S. Government. The fact that the Government formulated or supplied the drawings, specifications, or other data does not license the holder or any other person or corporation; or convey any rights or permission to manufacture, use, or sell any patented invention that may relate to them.

This report was cleared for public release by the Air Force Research Laboratory Wright Site (AFRL/WS) Public Affairs Office (PAO) and is releasable to the National Technical Information Service (NTIS). It will be available to the general public, including foreign nationals.

PAO case number: AFRL/WS 06-1900
Date cleared: 07 Aug 2006

THIS TECHNICAL REPORT IS APPROVED FOR PUBLICATION.

*//Signature//

EARL M. GREGORY
Project Engineer
Power Generation Branch

//Signature//

PAUL N. BARNES
Acting Chief
Power Generation Branch

//Signature//

KIRK L. YERKES, PhD
Deputy for Science
Power Division

This report is published in the interest of scientific and technical information exchange and its publication does not constitute the Government's approval or disapproval of its ideas or findings.

*Disseminated copies will show "//signature//" stamped or typed above the signature blocks.

REPORT DOCUMENTATION PAGE

Form Approved
OMB No. 0704-0188

1. REPORT DATE *(DD-MM-YY)*	2. REPORT TYPE	3. DATES COVERED *(From - To)*
June 2006	Final	06/19/2001 – 05/19/2005

4. TITLE AND SUBTITLE
MAGNETIC META-MATERIALS FOR ELECTROMAGNETIC APPLICATIONS

5a. CONTRACT NUMBER
F33615-01-2-2166

5b. GRANT NUMBER

5c. PROGRAM ELEMENT NUMBER
62203F

6. AUTHOR(S)
George C. Hadjipanayis

5d. PROJECT NUMBER
3145

5e. TASK NUMBER
29

5f. WORK UNIT NUMBER
M4

7. PERFORMING ORGANIZATION NAME(S) AND ADDRESS(ES)

University of Delaware
Department of Physics and Astronomy
Newark, DE 19716

8. PERFORMING ORGANIZATION REPORT NUMBER
PHYS 332116; PHYS 332117
PHYS 332118; BART 332112

9. SPONSORING/MONITORING AGENCY NAME(S) AND ADDRESS(ES)

Propulsion Directorate
Air Force Research Laboratory
Air Force Materiel Command
Wright-Patterson AFB, OH 45433-7251

Defense Advanced Research Projects Agency (DARPA)
3701 N. Fairfax Drive
Arlington, VA 22203

10. SPONSORING/MONITORING AGENCY ACRONYM(S)
AFRL-PR-WP

11. SPONSORING/MONITORING AGENCY REPORT NUMBER(S)
AFRL-PR-WP-TR-2006-2189

12. DISTRIBUTION/AVAILABILITY STATEMENT
Approved for public release; distribution is unlimited.

13. SUPPLEMENTARY NOTES
PAO case number: AFRL/WS 06-1900; Date cleared: 07 Aug 2006. This is the best copy available.

14. ABSTRACT

The most significant achievements of the project are 1) Development of R2Fe14B-based (nano)composite permanent magnets with maximum energy product (BH)m>50 MGOe, 2) Improvement of the magnetic properties of the existing Sm2Co17-type magnets with (BH)m close to their theoretical limit and with higher operating temperatures, up to 500 °C, 3) Development of new (nano)composite permanent magnets based on a hard magnetic phase (e.g., 2:17, 1:5) and a soft magnetic phase (Fe-based), 4) Development of new hybrid permanent magnets based on two hard magnetic phases (combinations between 2:14:1, 2:17 and 1:5), 5) Development of soft magnetic (nano)composites for high temperature (Fe-Co/W) and high frequency (artificial ferrites) applications. The obtained results encompassed the fabrication of new materials with outstanding, enhanced characteristics, as well as the theoretical description and understanding of their magnetic properties. New effects have been also put in evidence and opened up new perspectives in the understanding of the magnetic coupling and hardening mechanism.

15. SUBJECT TERMS
permanent magnets, soft magnetic materials, (nano)composites, exchange coupling, magnetostatic coupling, nanoparticles, nanowires

16. SECURITY CLASSIFICATION OF:			17. LIMITATION OF ABSTRACT:	18. NUMBER OF PAGES	19a. NAME OF RESPONSIBLE PERSON (Monitor)
a. REPORT	b. ABSTRACT	c. THIS PAGE			Earl Gregory
Unclassified	Unclassified	Unclassified	SAR	72	19b. TELEPHONE NUMBER *(Include Area Code)* N/A

Standard Form 298 (Rev. 8-98)
Prescribed by ANSI Std. Z39-18

Table of Contents

MAGNETIC META-MATERIALS FOR ELECTROMAGNETIC APPLICATIONS

1. Terms and Objectives

The research program *Magnetic Meta-Materials for Electromagnetic Applications,* which was supported by DARPA during the period July 2001 - May 2005, pursued the following objectives:

(a) To develop the next generation nanocomposite permanent magnets with up to a twofold increase in $(BH)_m$ (> 60 MGOe).

(b) To significantly improve the magnetic properties of existing advanced magnets with $(BH)_m$ close to their theoretical limit and with higher operating temperatures T_{op}.

(c) To develop soft magnetic nanocomposites for high temperature (Fe-Co/W) and high frequency (artificial ferrites) applications.

(d) To incorporate these magnets into systems/devices, for military and commercial applications.

2. Program Coordination and Participants

Joint efforts of the Meta-Materials team were coordinated by Prof. G.C. Hadjipanayis from the University of Delaware. The participating groups represented:

- Universities
  - University of Delaware (group leaders: G.C. Hadjipanayis, J.Q. Xiao, K.M. Unruh and S.T. Chui)
  - University of Dayton (S. Liu and C.H. Chen)
  - Carnegie Mellon University (S. Majetich)
- National laboratories
  - Naval Research Laboratory (D. Papaconstantopoulos)
- Industry
  - Electron Energy Corporation (J.F. Liu)
  - Advanced Ceramic Research (R. Vaidyanathan)
  - Materials Modification Inc. (T.S. Sudarshan)
  - Nanopac Inc. (W. Mayo)
  - Hamilton Sundstrand (D. Halsey)

3. Research Projects

The Program addressed two most significant groups of magnetic materials, hard and soft. The following specific materials were focused on:

- Hard magnetic materials
  - Nanocomposite magnets consisting of a mixture of hard and soft phases ($Nd_2Fe_{14}B$ / Fe and Sm_2Co_{17} / Fe)
  - Hybrid magnets consisting of a mixture of two hard phases, one with higher magnetization (Nd-Fe-B / Sm_2Co_{17}, Pr-Fe-B / $PrCo_5$ and Pr_2Co_{17} / $PrCo_5$)
  - High-temperature magnets $(Sm,Pr)(Co,Fe,Cu,Zr)_z$

- Soft magnetic materials
  - Artificial ferrites (Fe / SiO_2, Fe / Polymer / SiO_2, amorphous Fe(B) / crystalline Fe(B) and nanocomposites).

4. Approaches and Techniques

4.1. Synthesis Techniques

Amorphous, crystalline and nanocrystalline precursors for hard and soft magnetic materials were produced by the following conventional and novel techniques:

- Arc-melting under Argon,
- Conventional ball milling,
- High-energy ball milling (HEBM) including mechanical alloying,
- Melt-spinning,
- Chemical reduction,
- Sonochemical decomposition of $Fe(CO)_5$.

4.2. Consolidation Techniques

Fully dense nanocomposite and hybrid magnets were obtained (in addition to a conventional sintering) via:

- Hot Pressing,
- RF Rapid Inductive Compaction (UDRI),
- Transformation Assisted Consolidation (Nanopac Inc.),
- Plasma Pressure Consolidation (Materials Modification Inc.),
- Combustion Driven Compaction (Utron, Inc.)

4.3. Texturing Techniques

The following techniques were studied in an attempt to induce or improve *texture* in the nanocomposite magnets:

- Hot plastic deformation of consolidated melt-spun and HEBM alloys (R-Fe-B and R-Co),
- Melt-spinning of R-Fe-B alloys in a magnetic field,
- Magnetic annealing of amorphous melt-spun and HEBM alloys (R-Fe-B and R-Co),
- Stress annealing of melt-spun R-Fe-B alloys,- Directional crystallization of melt-spun R-Fe-B alloys through a laser annealing

4.4. Nanocomposite Hard Magnets

Nanocomposite magnets consisting of high-coercivity and high-magnetization components were manufactured through the following approaches:

(a) Consolidating electroless Co(Fe)-plated Sm-Co powders.
(b) Consolidating blends of Fe and Sm-Co particles.
(d) Hot deformation of R-lean R-Fe-B nanocomposites during phase transformation (R = rare earth).
(e) Search for the additions favoring texture development in R-lean R-Fe-B nanocomposites during hot plastic deformation.
(f) Consolidating and hot-deformation blends of R-lean and R-rich R-Fe-B powders.
(g) Consolidating and hot-deformation blends of Fe and R-rich R-Fe-B powders.
(h) Consolidating and hot-deformation blends of Fe(Co) and R-rich R-Fe-B powders.
(i) Preparation and study of high coercivity bulk FePt by diffusional mixing of an Fe/Pt nanocomposite.

4.5. Hybrid Hard Magnets

Hybrid magnets consisting of dissimilar high-coercivity components were obtained though the following approaches:
(a) Consolidating blends of single-crystalline $(Nd,Dy)_2Fe_{14}B$ and $(Pr,Sm)Co_5$ powders.
(b) Consolidating blends of milled die-upset Nd-Fe-B magnets and milled Sm-Co-Fe-Cu-Zr sintered magnets.
(c) Die-upsetting blends of melt-spun Pr-Fe-B ribbons and $PrCo_5$ nanocrystalline powders.
(d) Die-upsettind RCo_5 / R_2Co_{17} magnets consolidated from HEBM alloys.

4.6. High-temperature Magnets

High-temperature magnets were developed though the following approaches:
(a) Optimization of the heat-treatment of $Sm(Co,Fe,Cu,Zr)_z$ magnets.
(b) Pr-substitution for Sm in $Sm(Co,Fe,Cu,Zr)_z$ in order to increase room-temperature $(BH)_{max}$.
(c) Solidification of $Sm(Co,Fe,Cu,Zr)_z$ alloys in a high magnetic field.
(d) Coercivity studies in $Sm(Co,Fe,Cu,Zr)_z$ magnets.
(e) Coercivity studies in model Sm-Co-Cu, Sm-Co-Fe-Cu and Sm-Co-Fe-Cu-Zr bulk-hardened alloys.
The following approaches were also studied in an attempt to induce magnetic hardness in additions-free (pure binary) Sm_2Co_{17} alloys:
(f) Plasma bombardment by Ar ions,
(g) Sonochemical treatment with high power ultrasonic process,
(h) Neutron irradiation.

4.7. Soft Magnetic Materials

The approaches to obtain advanced soft magnetic materials and metaferrites with high saturation magnetization and low power loss were:
(a) Identifying the role of reactant concentrations, reaction temperature, pH, and mixing rate on the incorporation of B into Fe nanoparticles prepared by $NaBH_4$ reduction of Fe^{2+} ions.
(b) Compacting CoFe, Co, FeNi nanoparticles coated with suitable ferrites or other insulating materials to achieve exchange coupling among metallic nanoparticles.
(c) Controlling the shape of magnetic entities to minimize demagnetization effect and eddy current effect.

5. Results

5.1. The most significant technical achievements in hard magnetic materials

(a) Developed anisotropic *exchange-coupled* $R_2Fe_{14}B$ / α-Fe and $R_2Fe_{14}B$ / Fe-Co nanocomposite magnets with $(BH)_m$ > 50 MGOe. Thus, the achieved maximum energy product of the nanocomposite magnets almost reached that of the best sintered Nd-Fe-B.
(b) Developed anisotropic *magnetostatically coupled* $R_2Fe_{14}B$ / α-Fe and $R_2Fe_{14}B$ / Fe-Co composite magnet with improved $(BH)_m$ made out of coarse (0.04 - 2.0 mm) soft powders. This result proves that, contrary to the common belief, a magnetostatic coupling may play a favorable role in improving magnetic hardness and also it points out the importance of a morphology of soft inclusions in hard / soft magnets.

(c) Discovered a strong effect of a small Cu and Cu-Ga addition on the texture development in die-upset $R_2Fe_{14}B$ / α-Fe nanocomposite magnets and developed anisotropic $R_2Fe_{14}B$ / α-Fe nanocomposite magnet with less than 11.8 at.% R made out of blend of R-lean and R-rich melt-spun alloys. According to the traditional belief, only the alloys with more than 11.8 at.% R are susceptible the texture development.
(d) Developed *anisotropic* Sm_2Co_{17} / α-Fe nanocomposite magnets with $(BH)_m > 31$ MGOe. This result demonstrates the effectiveness of consolidation of a hard / soft powder blend.
(e) Developed *isotropic* Sm_2Co_{17} / Fe-Co nanocomposite magnets with $(BH)_m > 14$ MGOe. Compared to the commercial 2:17 Sm-Co magnets at high temperatures, the nanocomposite magnets have higher Curie temperature, better thermal stability and better mechanical properties, and therefore can be used for applications with special requirements, even for isotropic magnets.
(e) Developed procedures for the reliable and reproducible preparation of elemental nano-crystalline (*nx*) Fe and Pt powders and *nx*-Fe / *nx*-Pt nanodispersions. The goal is to achieve a single hard magnetic phase with an enhanced energy product by exchange coupling.

5.2. <u>The most significant technical achievements in soft magnetic materials</u>

(a) Developed a method of producing large quantity magnetic nanoparticles (Co, Fe-Ni, etc.). The Co particles with the average size 4.7 nm have been obtained by a $NaBH_4$ reduction.
(b) Developed a method of coating metallic magnetic nanoparticles with a thin layer of $NiFe_2O_4$ or SiO_2.
(c) Developed exchange-coupled soft magnetic materials with flat permeability spectrum up to at least 100 MHz. The materials exhibit permeability of about 16, saturation induction of about 1.6 T, saturation field of about 2 kOe, and quality factor around 100.
(d) Developed economical viable process to convert metallic particles into flake structure with lateral dimension of a few to several hundred microns and submicron thickness. The flake structure effectively minimized demagnetization and eddy current effect.
(e) Developed high-frequency, high-power, low-loss soft magnetic composites based on laminated submicron Fe flakes. The composites those surpass all current soft magnetic materials exhibit flat permeability spectra up to about 50 MHz with permeability of about 70, saturation induction of about 1.6 T, and saturation field of about 2 kOe.
(f) Obtained Co nanowire arrays with texture controlled during fabrication. At above 10 GHz, the arrays permeability around 10-20 with loss tangent less than 0.1.
(g) Developed procedures for the reliable and reproducible preparation of elemental *nx*-Fe and nanoamorphous (*na*) Fe(B) powders and two-component *nx*-Fe / *na*-Fe(B) nanodispersions.
(h) Obtained *nx*-Fe / *na*-Fe(B) nanodispersions that exhibit a coercivity lower than either constituent and with a magnetization near that of single phase *nx*-Fe.

5.3. <u>The most significant scientific achievements</u>

(a) Discovered a universal correlation between the magnetic state of $Sm(Co,M)_5$ alloys (M = Cu or Cu-Fe) and the increase of their H_c with a low-temperature aging.
(b) Discovered that the dramatic magnetic hardening of $Sm(Co,Fe,Cu)_5$ alloys in a narrow range of aging temperatures is associated with an increase in the Curie temperature and not accompanied by a the heat-treatment of $Sm(Co,Fe,Cu,Zr)_z$ magnets detectable phase

transformation. The atomic reordering suggested by the theory, due to the change in preferred atomic site occupancies, may be responsible for the dramatic increase in coercivity.

(c) Understood betterthe bulk magnetic hardening behavior with and without phase separation in $Sm(Co,Cu)_{5-7.3}$. Development of the coercivity in the magnets with the cellular structure may be quantitatively explained considering only the evolution of their 1:5 matrix phase. It is suggested that domain wall pinning in the 2:17 magnets takes place within triple junctions of the 1:5 cell boundaries, rather than at the 2:17 / 1:5 interface.

(d) Studied the structure evolution in 2:17 Sm-Co magnets with High-Resolution TEM, Mössbauer Spectroscopy and Extended X-ray Absorption Fine Structure (EXAFS). A beetter understanding of the structural mechanism in bulk magnetic hardening may lead to a breakthrough in the development of improved or novel hard magnetic materials.

(e) Theoretically studied the magnetic anisotropy in $SmCo_5$ and derivative structures.

- Identified the microscopic origins of the high magnetic anisotropy energy (MAE) as (i) a high MAE of the Co subsystem coming from a peak in the density of states at the Fermi level and (ii) high MAE of the Sm f-shells due to the interplay between the spin-orbital interaction and the crystal field.
- Explained the positive effect of Zr on the MAE of Sm_2Co_{17} in terms of the relative sizes of Zr, Co_2 and Sm atoms and related that to the crystal field magnitude of Sm.
- Found that Fe doping affects MAE primarily via the Fermi level shift. The calculations showing an increase of the MAE at small Fe concentrations and a rapid decrease for concentrations of Fe larger than 10 - 15% are consistent with existing data on $Y(Co,Fe)_5$.
- Evaluated the effects of the hydrostatic compression/expansion and c/a ratio on MAE. The effects are found to be too small to be of practical interest.
- Found a non-monotonic dependence of the saturation magnetization of $SmFe_xCo_{5-x}$ on the Fe concentration. The effect can be explained using an extended Stoner theory.
- Found that magnetism suppression by Cu depends on the preferential occupation: suppression of total M by one Cu per cell is 0.5 μ_B stronger when Cu occurs in the $SmCo_2$ plane.
- Found that exchange coupling for the Co-Co interaction is always long-range.

6. The most promising directions of a future search for advanced permanent magnets

Modification of existing phases / microstructures

- The interstitially modified $Sm_2Fe_{17}N_x$ compound has excellent combination of the intrinsic magnetic properties ($4\pi M_S$ = 15.4 kG, H_A = 140 kOe, T_C = 476 oC). However, because of its poor structural stability at the elevated temperatures this compound has only very limited application in bonded magnets. Development of an appropriate consolidation technique may open the way for its widespread application as a fully dense high-performance permanent magnet.
- Tuning microstructure / microchemistry in 2:17 magnets may improve their performance at the elevated temperature and, possibly, extend the operating temperature range of these magnets beyond 500 °C.

Nanocomposite / composite materials.

Though the highest obtained $(BH)_m$ of the nanocomposite magnets (55 MGOe) is still somewhat smaller than that of the best sintered magnets (59 MGOe), the theoretical $(BH)_m$ for anisotropic nanocomposites is 120 MGOe. In the novel magnetostatically coupled composite magnets, the requirements for a grain size are not as strict as in the exchange-coupled materials. Magnetostatically coupled and magnetostatically-assisted exchange-coupled hard-soft magnets is a new unexplored area.

Search for new compounds with high saturation magnetization and anisotropy field.

So far only binary and some ternary compounds have been investigated. There is still a good chance that out of many combinations (quaternary and higher) a new phase can be found with better performance.

Publications:

1. "Crystallographic texture study in melt-spun Pr-Fe-B 2:14:1 based nanocomposite magnet" Z. Q.Jin, H.L.Wang, G. C. Hadjipanayis. Microscopy & Microanalysis, n. 8, suppl 2, (2002) 1378.

2. "Relation of Coercivity of Sm(Co,Cu, Fe, Zr) 2:17 magnets to microstructure and microchemistry" Y.Zhang, W.Tang, C. E.Nelson, K. M.Krishnan, G. C. Hadjipanayis. Proc. of 15th Int. Congress on Electron Microscopy (2002) v. 1, p. 301.

3. "Microstructure, magnetic properties and magnetic hardening in 2:17 Sm-Co magnets" W.Tang, Y.Zhang, G. C.Hadjipanayis. Zeitschrift für Metallkunde, 93, (2002) 1002.

4. "Microstructure refinement and significant improvements of magnetic properties in Pr2Fe14B/alpha-Fe nanocomposites" Z.Q. Jin, H.Okumura, Y.Zhan, H.L.Wang, J.S.Munoz, G.C.Hadjipanayis. J. Magn. Magn. Mater. 248 (2002) 216.

5. "High Coercivity in Boron Substituted Sm-Co Melt-Spun Magnets" S.S.Makridis, G.Litsardakis, I.Panagiotopoulos, D.Niarchos, Y.Zhang, G.C.Hadjipanayis. IEEE Trans. Magn. 35 (2002) 2922.

6. "The Relationship between the Composition and the Abnormal Temperature Dependence of Coercivity in Sm(Co,Fe,Cu,Zr)z" W.Tang, Y.Zhang, G.C.Hadjipanayis. IEEE Trans. Magn. 35 (2002) 2940.

7. "Magnetic Hardening Studies in Sintered Nd-Fe-B based Magnets", Y.Zhang, A.M.Gabay, E.Belozerov and G.C.Hadjipanayis, Proc. 17th Int. Workshop on Rare Earth Magnets and their Applications (2002) 967.

8. "Effect of Zr on the Microstructure, magnetic domain structure, microchemistry and magnetic properties in $Sm(Co_{bal}Cu_{0.088}Fe_{0.01}Zr_x)_{8.5}$ Magnets", Y.Zhang, W.Tang and G.C.Hadjipanayis, Proc. 17th Int. Workshop on Rare Earth Magnets and their Applications (2002) 975.

9. "Influence of Co Substitution on Crystallographic Texture and Magnetic Properties of $Pr_2Fe_{14}B$/Fe Nanocomposites", Z.Q.Jin, Y.Zhang, H.Okumura, H.L.Wang, A.Klaessig and G.C.Hadjipanayis, Proc. 17th Int. Workshop on Rare Earth Magnets and their Applications (2002) 932.

10. "Effect of Particle size on the Coercivity of Rare Earth Magnets Prepared by Ball Milling", Q.Zeng, Y.S.Wang, E.V.Belozerov and G.C.Hadjipanayis, Proc. 17th Int. Workshop on Rare Earth Magnets and their Applications (2002) 983.

11. "Composite Sm-Co-Fe Magnets Prepared by Mechanical Milling", Q.Zeng, Y.Zhang and G.C.Hadjipanayis, Proc. 17th Int. Workshop on Rare Earth Magnets and their Applications (2002) 961.

12. "Cobalt Substituted $Nd_{10}Fe_{82}C_2B_6$ Melt-Spun Ribbons", D.Sultana, M.Daniil, Y.Zhang and G.C.Hadjipanayis, Proc. 17th Int. Workshop on Rare Earth Magnets and their Applications (2002) 630.

13. "Effect of Composition and Processing on Microstructure and Magnetic Properties of $Sm(Co_{bal}Fe_vCu_yZr_x)z$ Magnets", W.Tang, Y.Zhang, A.M.Gabay, H.Kronmuller and G.C.Hadjipanayis, Proc. 17th Int. Workshop on Rare Earth Magnets and their Applications (2002) 685.

14. "Pr-Fe-B Based Nanocomposites with High Energy Product", Z.Q.Jin, Y.Zhang, H.Okumura, H.L.Wang, A.Klaessig and G.C.Hadjipanayis, Proc. 17th Int. Workshop on Rare Earth Magnets and their Applications (2002) 760.

15. "Magnetic and Structural Characterization of B-rich $Nb_3Tb_1Cr_1Fe_{77}B_{18}$ Nanocomposites", H.L.Wang, Y.Zhang, Z.Q.Jin and G.C.Hadjipanayis, Proc. 17th Int. Workshop on Rare Earth Magnets and their Applications (2002) 900.

16. "Nanocomposite Melt-Spun Sm-Co-Fe-Zr-B-[Cu/Ni] 1:7.5 Type Magnets with high Coercivity", S.S.Markridis,G.Litsardakis, E.Pavlidou, K.Chrisafis, K.G.Efthmiadis, Y.Zhang and Hadjipanayis, Proc. 17th Int. Workshop on Rare Earth Magnets and their Applications (2002) 947.

17. "Application of Amorphous Iron in $SmCo_5$ Nanocomposites", S. Chu and S. A. Majetich, Proc. 17th Int. Workshop on Rare Earth Magnets and their Applications (2002) 905.

18. "Topology dependence of domain wall depinning in magnetic hard-soft composites", S. T. Chui, Z. F. Lin, L. B. Hu, J. Appl. Phys. 93 (2003) 6192.

19. "Magnetic and Structural Properties of $Sm_2(Co_{1-x}Fe_x)_{17}$ Based Powders and Spin Cast Ribbons", C. Chen, S. Kodat, M.H. Walmer, S. Sheng, M.A. Willard, V.G. Harris, Proc. 17th Int. Workshop on Rare Earth Magnets and their Applications (2002) 844.

20. "Magnetic and Structural Properties of Sm(Co, Cu, Hf)$_7$ Metastable Sintered Magnets", W. Gong, C.H. Chen, M. H. Walmer, Proc. 17th Int. Workshop on Rare Earth Magnets and their Applications (2002) 860.

21. "Applications of Improved Permanent Magnet Materials", D. Halsey, Proc. 17th Int. Workshop on Rare Earth Magnets and their Applications (2002) 1027.

22. "Nanostructured Melt-Spun Sm(Co-Fe-Zr-B)$_{7.5}$ Alloys for High Temperature Magnets", S.S.Markridis, G.Litsardakis,K.G.Efthimiadis, G.Papathanasiou, I.Panagiotopoulos, D.Niarchos and G.C.Hadjipananyis, IEEE Trans. Magn. 39 (2003) 2869.

23. "The improved magnetic properties in phosphorous substituted Pr-Fe-B nanocomposites" Z.Q. Jin, Y. Zhang, H.L. Wang, A. Klaessig, M.J. Bonder and G. C. Hadjipanayis, J. Appl. Phys. 93 (2003) 6492.

24. "Fabrication of Sm-Co/Co(Fe) composite magnets by electroless Co and Co-Fe alloy plating technique" Q. Zeng, Y. Zhang, M.J. Bonder, and G. C. Hadjipanayis, J. Appl. Phys. 93 (2003) 6498.

25. "The influence of Co substitution on the crystallization behavior and magnetic properties of melt-spun (Pr, Tb)$_2$(Fe, Nb, Zr)$_{14}$B/α-Fe nanocomposites" H.L. Wang, Y.Zhang, Z.Q. Jin, and G. C. Hadjipanayis, J. Appl. Phys. 93 (2003) 7978.

26. "Magnetic properties and microstructure of fine Fe-Pt nanoparticles prepared by chemical Reduction" Q. Zeng, Y. Zhang H. L. Wang V. Papaefthymiou and G.C. Hadjipananyis, J. Magn. Magn. Mater. 272-276, Suppl. 1 (2004) e1223.

27. "Structural and Magnetic Properties of Rhombohedral $Sm_2(Co,Fe,Cr)_{17}B_x$ and $Sm_2(Co,Fe,Mn)_{17}B_x$ compounds", S.S.Markridis, G.Litsardakis, K.G.Efthimiadis, G.Papathanasiou, I.Panagiotopoulos, D.Niarchos and G.C.Hadjipananyis, IEEE Trans. Magn. 39 (2003) 2872.

28. "Bulk $SmCo_5$/α-Fe composites by plasma pressure compaction", Q. Zeng, Y. Zhang, , M. J. Bonder, G. C. Hadjipanayis, R. Radhakrishnan, IEEE Trans. Magn. 39 (2003) 2974.

29. "Effects of Co substitution on the magnetic and microstructural properties of melt-spun $Pr_7Tb_1Fe_{87-x}Co_xNb_{0.5}Zr_{0.5}B_4$ nanocomposites", H.L. Wang, Y. Zhang, Z.Q. Jin, G.C. Hadjipanayis, IEEE Trans. Magn. 39 (2003) 2941.

30. "Calculation of magnetic anisotropy energy in YCo_5," P. Larson, I.I. Mazin, J. Mag. Mag. Mat. 264 (2003) 7.

31. "Magnetic properties of YCo_5 and $SmCo_5$", P. Larson, I.I. Mazin, J. Appl. Phys, 93 (2003) 6888.

32. "Calculation of magnetic anisotropy energy in $SmCo_5$", P. Larson, I.I. Mazin, D.A. Papaconstan-topoulos, Phys. Rev. B 67 (2003) 214405.

33. "Ferromagnetism and spin-orbital compensation in Sm intermetallics", H. J. Gotsis and I. I. Mazin, Phys. Rev. B 68, 224427.

34. "Effect of impurities on magnetic properties of $Y(Co_{5-x}Cu_x)$ and $Y_2Co_{7-x}Ni_x$". P. Larson, I.I. Mazin, J. Magn. Magn. Mater. 269 (2004) 176.

35. "Effects of doping on the magnetic anisotropy energy in $SmCo_{5-x}Fe_x$ and $YCo_{5-x}Fe_x$", P. Larson, I.I. Mazin, D.A. Papaconstantopoulos, Phys. Rev. B 69 (2004) 134408.

36. "Effect of lattice relaxation on magnetic anisotropy: Zr-doped Sm_2Co_{17}", P. Larson, I.I. Mazin, Phys. Rev. B 69 (2004) 012404.

37. "Synthesis and magnetic behavior of $(SmCo_5)_{1-x}Fe_x$ nanocomposite magnets", S. Chu, S.A. Majetich, M. Huang, R.T. Fingers, J. Appl. Phys. 93 (2003) 8146.

38. "The Effects of Grain Size and Morphology on the Coercivity of $Sm_2(Co_{1-x}Fe_x)_{17}$ Based Powders and Spin Cast Ribbons", C. Chen, S. Kodat, M.H. Walmer, S. Cheng, M.A. Willard, V. G. Harris, J. Appl. Phys. 93 (2003) 7966.

39. "Hot-pressed and Hot-Deformed Nanocomposite $(Nd,Pr,Dy)_2Fe_{14}B/\alpha$-Fe based magnets", D. Lee, J.S. Hilton, S. Liu, Y. Zhang, G.C. Hadjipanayis, and C.H. Chen, IEEE Trans. Magn. 39 (2003) 2947.

40. "Magnetic Properties of $SmCo_7$/Co and $Sm(Co,Fe)_7$/ α-Fe Nanocomposite Magnets Prepared by Magnetic Annealing", B.Z. Cui, M.-Q. Huang, S. Liu, IEEE Trans. Magn. 39 (2003) 2866.

41. "Magnetization reversal in antiferromagnetically coupled ternary layers" Y. J. Wang, S. T. Chui, J. Appl. Phys. 94 (2003) 525.

42. "A simple method to prepare uniform Co nanoparticles", Y.-W. Zhao, X.X. Zhang, R.K. Zheng, J.Q. Xiao, IEEE Trans. Magn. 39 (2003) 2764.

43. "Explosion Compacted FeCo Particles Coated with Ferrites: A Possible Route to Achieve Artificial Soft Ferrites", Y.-W. Zhao, T. Zhang, J.Q. Xiao, J. Appl. Phys. 93 (2003) 8014.

44. "Die-upset hybrid Pr-Fe-B nanocomposite magnets", A.M. Gabay, Y. Zhang, G.C. Hadjipanayis, Appl. Phys. Lett. 85 (2004) 446.

45. "Recent Studies in bulk 2:17 and Nanocomposite R-Co Magnets", G.C. Hadjipanayis and A.M. Gabay, in Proc. China Magnet Symposium, Xi'an, China (2004) 65-76.

46. "Overview of the high-temperature 2:17 magnets", G.C. Hadjipanayis and A.M. Gabay, in Proc. 18th International Workshop on High Performance Magnets and their Applications, Annecy, France (2004) 590.

47. " Nanocomposite Rare Earth Magnets", D. Lee, Hilton, C.H. Chen, M.Q. Huang, and S. Liu, in Proc. 18th International Workshop on High Performance Magnets and their Applications, Annecy, France (2004) 667.

48. "Microchemistry and microstructure of SmCo 2:17 permanent magnets with Ni, Pr, and Ti substitutions", Y. Zhang and G. C. Hadjipanayis, IEEE Trans. Magn. 40 (2004) 2925.

49. "Magnetic Domain Structure in SmCo 2:17 Permanent Magnets", Y. Zhang, W. Tang, and G. C. Hadjipanayis, C. Chen D. Goll, H. Kronmuller, IEEE Trans. Magn. 39 (2003) 2905.

50. " Microstructure, microchemistry, and coercivity in Sm-Co-Cu and Pr-Co-Cu 1:5 alloys", Y. Zhang, A. Gabay, Y. S. Wang and G. C. Hadjipanayis, J. Magn. Magn. Mater. 262-267, Suppl. 1 (2004) e1899.

51. "Fully dense Sm-Co-Fe-Cu and Sm-Co-Fe-Ga nanocomposite magnets by hot compaction", Q. Zeng, A. M. Gabay, Y. Zhang, and G. C. Hadjipanayis, IEEE Trans. Magn. 40 (2004) 2916.

52. "Effect of post deposition annealing on the hysteresis loops of sputtered NdFeB films", T. Speliotis, D. Niarchos, V. Skumryev, Y. Zhang, and G. C. Hadjipanayis, J. Magn. Magn. Mater. 262-267 (2004) 877.

53. "Fully dense bulk nanocomposites of $(Sm_{1-x}Gd_x)2(Co_{1-y}Fe^{y})_{17+}$(Co, Fe) with high coercivity and high Curie temperature", C. H. Chen, D. Lee, S. Liu, M. H. Walmer, Y. Zhang, and G. C. Hadjipanayis, IEEE Trans. Magn. 40 (2004) 2937.

54. "Bulk isotropic and anisotropic nanocomposite rare-earth magnets", D. Lee, J. S. Hilton, C. H. Chen, M. Q. Huang, Y. Zhang, G. C. Hadjipanayis, and S. Liu, IEEE Trans. Magn. 40 (2004) 2904.

55. "Exchange-coupled soft magnetic FeNi-SiO_2 nanocomposite", Y. Zhao, C. Ni, D. Kruczynski, X. Zhang and J.Q. Xiao, J. Phys. Chem. B 108 (2004) 3691.

56. "Magnetic states and structural transformations in $Sm(Co,Cu)_5$ and $Sm(Co,Fe,Cu)_5$ permanent magnets," A. M. Gabay, P. Larson, I. I. Mazin, G. C. Hadjipanayis, J. Phys. D, 38 (2005) 1337.

57. "Microstructure Characterization of Ball Milled Sm(CoCuFeZr) 2:17 Powders", Y. Zhang, Q. Zeng and G. C. Hadjipanayis, J. Appl. Phys. (in press).

58. "Cast composite Co-Fe / Sm-Pr-Co-Fe-Cu-Ti permanent magnets," A. M. Gabay, Y. Zhang, G. C. Hadjipanayis, J. Appl. Phys. (in press).

59. "Hot-pressed and die-upset Pr-Co magnets produced from mechanically activated alloys," A. M. Gabay, Y. Zhang, G.C. Hadjipanayis, J. Magn. Magn. Mater. (in press).

60. "Microstructure of R-Fe-B die-upset magnets (R = Pr, Nd) with high and low R content produced from mechanically milled powders," Y. Zhang, A. M. Gabay, G. C. Hadjipanayis, IEEE Trans. Magn. (in press).

61. "The effect of neutron irradiation on Sm_2Co_{17} -Based High Temperature Magnets and Nd-Fe-B Magnets," C.H. Chen, J. Talnagi, J. Liu, P. Vora, A. Higgins, S. Liu, IEEE Trans. Magn. (in press).

62. "Thermal Stability of Nanocomposite of $Sm_2(Co,Fe)_{17}$ Hard Phase and Co/Fe Soft Phase," C.H. Chen, Don Lee, Y. Zhang, and G. Hadjipanayis, S. Liu, to be submitted to IEEE Trans. Magn.

63. "Magnetostatically coupled composite magnets based on Nd-Fe-B," A. M. Gabay, Y. Zhang, M. Marinescu, G.C. Hadjipanayis, to be submitted to J. Appl. Phys.

64. "Magnetic core loss of ultrahigh strength nanocrystalline FeCo alloys," X. M. Cheng, X. K. Zhang, D. Z. Zhang, S. H. Lee, A. Duckham, T. P. Weihs, R. C. Cammarata, John Q. Xiao, C. L. Chien, J. Appl. Phys. 93 (2003) 7121.

65. "Magnetic properties of gadolinium and terbium nanoparticles produced via multilayer precursors," Z.C. Yan, Y.H. Huang, Y. Zhang, H. Okumura, J.Q. Xiao, S. Stoyanov, V. Skumryev, G. C. Hadjipanayis, Phys. Rev. B 67 (2003) 054403.

66. "Theoretical and Experimental Analysis of Magnetic Inductive Heating in Ferrite Materials," X.K Zhang, Y.F. Li, E.D. Wetzel, John Q Xiao, J. Appl. Phys. 93 (2003) 7124.

67. "Ferromagnetic Resonance in Granular Soft Magnetic Films," M. M. Corte-Real, J. Du, K. M. Unruh, J.Q. Xiao, IEEE Trans. Magn. 39 (2003) 3091.

68. "Low-Temperature Synthesis of Hexagonal (Wurtzite) ZnS Nanocrystals," Y. Zhao, Y. Zhang, H. Zhu, G.C. Hadjipanayis, J.Q. Xiao, J. Am. Chem. Soc., 126 (2004) 6874.

69. "Submicron Laminated Fe/SiO_2 Soft Magnetic Composites-an Effective Route to Achieve Materials for High Frequency Applications," Y. Zhao, X. Zhang, J.Q. Xiao, Adv. Materials 17 (2005) 915.

70. "Textured Co nanowire arrays with controlled magnetization direction," H.N. Hu, H.Y. Chen, S.Y. Yu, J.L. Chen, G.H. Wu, F.B. Meng, J.P. Qu, Y.X. Li, H. Zhu, J.Q. Xiao," J. Magn. Magn. Mater. (in press).

71. "Complex permittivity and permeability of magnetic granular composites at microwave frequencies," P. Chen, R. Wu, T. Zhao, Y. Fang, J.Q. Xiao, J. Appl. Phys. (submitted).

72. "Synthesis and Magnetic Properties of Magnetically Soft $FeCo-SiO_2$ Nanocomposite Particles," Y. Zhao, Y. Zhang, J.Q. Xiao, to be submitted to J. Am. Chem.

ELSEVIER

Journal of Magnetism and Magnetic Materials 248 (2002) 216–222

journal of magnetism and magnetic materials

www.elsevier.com/locate/jmmm

Microstructure refinement and significant improvements of magnetic properties in $Pr_2Fe_{14}B/\alpha$-Fe nanocomposites

Z.Q. Jin*, H. Okumura, Y. Zhang, H.L. Wang, J.S. Muñoz, G.C. Hadjipanayis

Department of Physics and Astronomy, University of Delaware, Newark, DE 19716, USA

Received 10 December 2001; received in revised form 13 March 2002

Abstract

Exchange coupled $(Pr,Tb)_2(Fe,Nb,Zr)_{14}B/\alpha$-Fe nanocomposites have been produced by melt spinning. A trend for perpendicular and planar *c*-axis orientation of the 2:14:1 phase was observed in the free surface of ribbons spun at speeds below 10 m/s and at optimal speeds, respectively. Higher wheel speeds led to the formation of an amorphous phase that transformed to 2:14:1 phase around 680°C. Optimum magnetic properties were found in samples spun at 14–17 m/s and annealed at 700°C for 20 min. The loop squareness was also found to depend mainly on the microstructure that is very sensitive to the sample composition. A few percentage of Nb and Zr suppressed the grain growth, resulting in a drastic improvement of magnetic properties, with approximate 50% enhancement in the intrinsic coercivity and an increase in maximum energy product from 5.6 kOe and 14.7 MGOe for the (Nb,Zr)-free sample to 8.2 kOe and 20.3 MGOe for the (Nb,Zr)-substituted samples, respectively. The significant improvement in magnetic properties originated from a much finer and homogeneous nanocomposite microstructure with an average grain size of 20 nm, leading to a high remanence of 0.73 M_s. Henkel plots indicate the enhancement of exchange coupling between hard and soft magnetic phases.

PACS: 75.50.Tt; 75.50.Ww 81.05.Ys; 81.40.Ef

Keywords: Nanocomposite magnet; Melt-spinning; Microstructure; Magnetic properties

1. Introduction

Recently, nanocomposite magnetic materials consisting of a fine mixture of magnetically hard and soft phases have been extensively studied for permanent magnet development due to their enhanced remanence and potentially high-energy products even in materials with a relatively low content of the expensive rare-earth elements [1–4]. However, the maximum energy product of nanocomposite magnets obtained experimentally up to now was significantly lower than that predicted by theory [4–7]. The intrinsic coercivities reported were usually below 6.5 kOe due to the presence of soft magnetic phase with volume percentage around 30 vol% [6–8]. Micromagnetic calculations by Schrefl et al. [9] showed that the magnetic properties were strongly dependent on microstructural parameters, such as grain size, grain boundaries, phase distribution, and the volume fraction

*Corresponding author. Tel.: +1-302-831-3515; fax: +1-302-831-1637.

E-mail address: zqjin@udel.edu (Z.Q. Jin).

0304-8853/02/$ - see front matter
PII: S0304-8853(02)00282-2

ratio between the soft and hard magnetic phases. The most critical parameter for a high coercivity is the grain size of soft magnetic phase that should be sufficiently small (5–10 nm). Experimentally, the desired nanocrystalline structure was generally obtained either by rapid quenching [2,6,10,11] or by mechanical alloying [12]. However, these fabrication methods made it technically difficult to control the nanostructures, especially the grain size and the grain boundary. Previous studies showed that Tb addition increase significantly the coercivity of $Pr_2Fe_{14}B$ due to the higher anisotropy field of $Tb_2Fe_{14}B$ and to a refinement in microstructure [6]. Other studies also revealed that small substitutions of Fe with refractory elements (Cr, Ti, Nb, Zr) could suppress the grain growth of α-Fe, thus refining the microstructure to a smaller grain size [10,11]. In this paper, the microstructure and magnetic properties of $(Pr,Tb)_2(Fe,Nb,Zr)_{14}$/α-Fe nanocomposite ribbons have been investigated. Significant improvements of magnetic properties have been observed by the small additions of Nb and Zr which led to $(BH)_m >$ 20 MGOe.

2. Experimental

Alloys with nominal compositions of $Pr_7Tb_1Fe_{88-x-y}Nb_xZr_yB_4$ $(x = 0-2; y = 0-1)$ (atomic percentage) were prepared by arc-melting the constituent elements in an argon atmosphere. The arc-melted ingots were cut into small pieces (2–3 mm) and then melt-spun in argon atmosphere from a quartz tube with an orifice diameter of about 0.5 mm. Substrate velocities from 5 to 40 m/s were used and optimized for each composition. The chamber pressure was adjusted from 0.5 to 1.2 atm. The obtained ribbons had a width of about 3 mm, a length ranging from a few millimeters to a few hundred millimeters. The density measured is around 7.6 g/cm^3. For annealing experiments, selected as-spun ribbons were sealed in quartz tube under a 2×10^{-5} Torr vacuum and then annealed at temperatures between 650°C and 850°C to develop a fine nanocrystalline microstructure with optimum coercivity. The crystallization behavior of the as-spun ribbons was determined using a du Pont Instruments differential scanning calorimeter (DSC) at a heating rate of 10°C/min. Hysteresis loops along the ribbon length and normal to the ribbon plane were measured using an Oxford vibrating sample magnetometer with an applied field up to 50 kOe. Structural and microstructural studies were carried out using a Philips X-ray diffractometer (XRD) and a JEOL JEM-2000FX transmission electron microscope (TEM), respectively.

3. Results and discussion

Fig. 1 presents the typical XRD spectra of the wheel-contacted surface and free surface of $Pr_7Tb_1Fe_{87}Nb_{0.5}Zr_{0.5}B_4$ ribbons spun at different speeds. An isotropic XRD pattern of 2:14:1 phase is observed for the wheel-contacted surface upon spinning at low speeds. However, for the free surface, the most prominent peaks for ribbons spun at 5 m/s are the (0 0 4), (0 0 6) and (0 0 8) reflections of tetragonal $Pr_2Fe_{14}B$ phase, which indicates a trend for a *c*-axis texture of 2:14:1 phase perpendicular to the ribbon plane. In $Pr_2Fe_{14}B$, the *c*-axis is the easy axis of magnetization and therefore, there may be a perpendicular

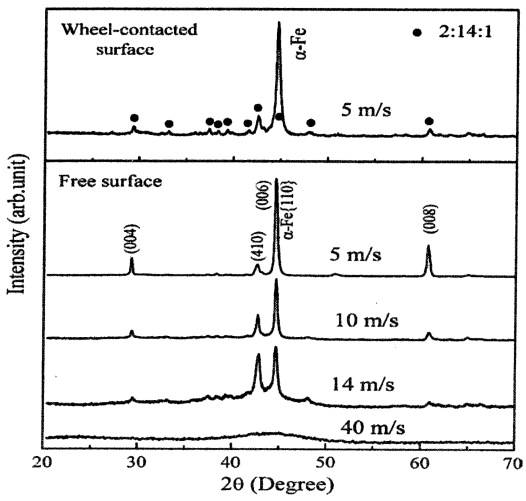

Fig. 1. X-ray diffraction patterns of as-spun $Pr_7Tb_1Fe_{87}Nb_{0.5}Zr_{0.5}B_4$ ribbons.

magnetic anisotropy suggested for the free surface of ribbons. This texture only exists in a thin layer of free surface (as it will be shown later). Due to the large grain size of hard and soft phases in the ribbons spun at such a low speed, the sample presents a soft magnetic behavior with a very low coercivity of around 0.2 kOe. A strong α-Fe (1 1 0) peak overlaps with the $(0\,0\,6)_{2:14:1}$ peak, indicating that the α-Fe grains are crystallogrophically textured to a (1 1 0) direction and coexist with the *c*-axis texture of the 2:14:1 phase. At the higher wheel speed of 14 m/s, the perpendicular *c*-axis texture disappears, and the planar (4 1 0) reflection becomes pronounced, indicating mostly an in-plane distribution of the easy *c*-axis. Meanwhile, an α-Fe/$Pr_2Fe_{14}B$-type nanocomposite microstructure is developed directly from the melt during the melt-spinning process. Fig. 2 shows the cross-section of the samples spun at 14 m/s. A very thin layer in the free surface of the ribbon was observed together with a large portion of fine grain existing in the middle zone and some columnar crystals nearby the wheel-contact surface. The perpendicular and in-plane crystallographic textures in the free surface may be correlated to both the directional solidification because of a thermal gradient and to the seeding effect of the (1 1 0) crystal texture of α-Fe phase, which have been verified in nanocomposite $Nd_2Fe_{14}B$/α-Fe ribbons and anisotropic $Nd_2Fe_{14}B$ films [13,14]. A fully amorphous state can be observed in ribbons spun with wheel speeds above 40 m/s, which show a very low coercivity due to the lack of atomic long-range order in the amorphous alloys.

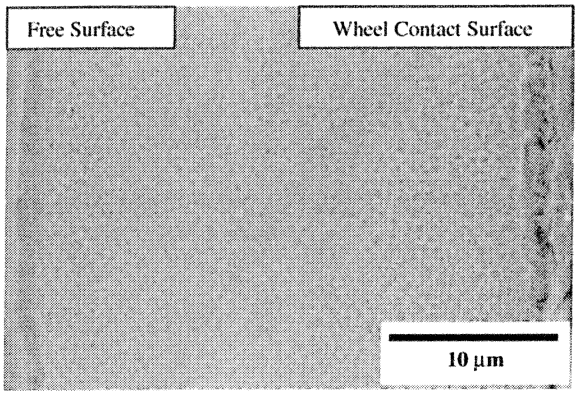

Fig. 2. Cross-sectional microstructure of ribbon spun at 14 m/s.

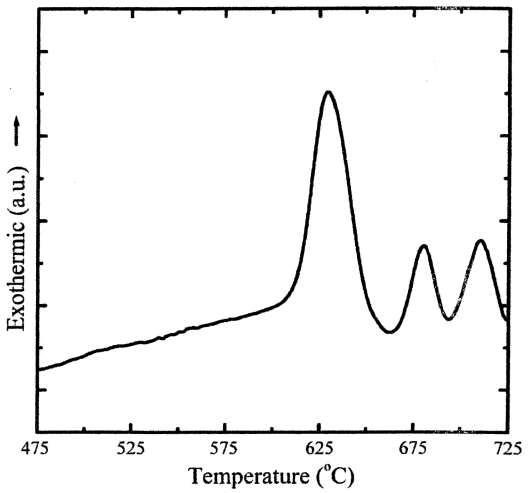

Fig. 3. DSC curve of $Pr_7Tb_1Fe_{87}Nb_{0.5}Zr_{0.5}B_4$ ribbons spun at 40 m/s.

The DSC curve performed at a scanning rate of 10°C/min is shown in Fig. 3 for the amorphous samples. XRD investigations performed on samples annealed at the peak temperatures show that the first exothermic peak corresponds to the crystallization from amorphous phase to the metastable $TbCu_7$-type structure. The second peak (680°C) correlates to the transformation from $TbCu_7$-type phase to 2:14:1 phase. The last one is attributed to the precipitation of $(Pr,Tb)_{1+\delta}(Fe,Nb,Zr)_4B_4$ phase, similar to the results reported in the $(Pr,Tb)_2(Fe,Nb)_{14}B$/α-Fe nanocomposites [15].

Fig. 4 summarizes the magnetic properties as a function of the wheel speed for the $Pr_7Tb_1Fe_{87}Nb_{0.5}Zr_{0.5}B_4$ samples annealed at 700°C for 20 min. Optimum magnetic properties are found in samples spun between 14 and 17 m/s. High wheel speeds lead to the decrease of magnetic properties due to the occurrence of coarse grains during subsequent annealing. XRD studies also revealed that the annealed ribbons spun at low speed (14 m/s) contain a larger volume fraction of 2:14:1 nanocrystallites than those spun at higher speeds (> 20 m/s). This should be related to the initial phase structure of as-spun samples and can be understood in terms of the different formation

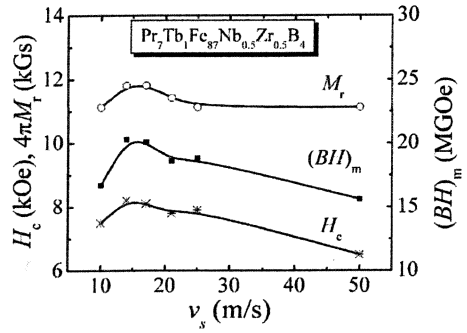

Fig. 4. Magnetic properties as a function of wheel speed v_s.

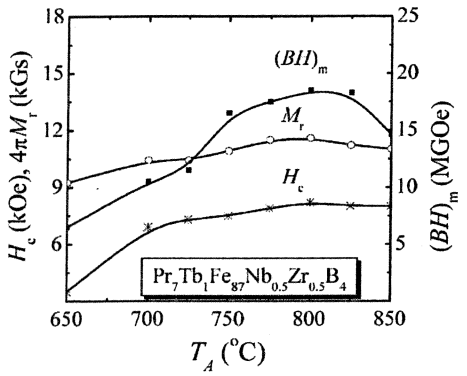

Fig. 5. Magnetic properties as a function of annealing temperature T_A for ribbons spun at 14 m/s.

mechanism of 2:14:1 phase involved in these samples. For the former, the 2:14:1 phase precipitates directly from the pre-existing 2:14:1 nanocrystallites upon heat treatment, leading to a fine microstructure. In this case, hard magnetic nanocrystallites have a higher nucleation rate but a lower growth rate with increasing cooling rate. Whereas in the later case, the number of nucleation sites for 2:14:1 decreases with the cooling rate, and the grains tend to grow much in the samples.

The dependence of magnetic properties on annealing temperature is shown in Fig. 5 for the $Pr_7Tb_1Fe_{87}Nb_{0.5}Zr_{0.5}B_4$ ribbons spun at 14 m/s and annealed for 1 min. It can be seen that the magnetic properties, including the coercivity H_c, remanence M_r and maximum energy product $(BH)_{max}$, increase initially with annealing temperature, showing peak values around 800°C, and then decrease with further increase of annealing temperature due to grain growth. Further studies as shown in Fig. 6 revealed that optimal magnetic properties could be obtained upon annealing for 20 min at 700°C, which is slightly above the transformation temperature of 680°C. XRD patterns revealed that the crystallized alloys consist of a nanocrystalline microstructure with grain size around 20–40 nm as calculated by Scherrer formula.

The magnetic properties also depend sensitively on the composition of the material. Table 1 summarizes the magnetic properties of $Pr_7Tb_1Fe_{88-x-y}Nb_xZr_yB_4$ ribbons ($x = 0-2$; $y = 0-1$). It can be seen that the coercivity and the reduced remanence (M_r/M_s) significantly increase with all the substitutions. Although the Nb substitution leads to a slight decrease of energy product, the addition of Zr improves it significantly. Substitutions of 0.5 at% Zr and 0.5 at% Nb for Fe lead to an approximate 50% improvement in the coercive field and the maximum energy product. The enhanced M_r/M_s ratio (~ 0.73) indicates the existence of stronger intergranular exchange interactions between the 2:14:1 hard phase and the soft α-Fe grains. Optimal magnetic properties of $H_c = 8.2$ kOe, $M_r = 11.7$ kGs and $(BH)_m = 20.3$ MGOe have been obtained in the Zr and Nb substituted sample as compared to 5.6 kOe, 10.7 kGs and 14.7 MGOe in the $Pr_7Tb_1Fe_{88}B_4$ sample. The magnetic properties of these samples are found to decrease with further increasing the amount of non-magnetic Zr and Nb elements due to the dilution of the overall magnetization.

Fig. 7 shows the typical hysteresis loops of selected $(Pr,Tb)_8(Fe,Nb,Zr)_{88}B_4$ samples. A demagnetization curve characteristic of single hard magnetic phase has been observed in all the samples even though the samples consist of two different magnetic phases. The ratio of remanence to saturation magnetization is higher than 0.5, indicating an exchange-coupling phenomenon peculiar to nanocomposite magnets. However, a "slanted" demagnetization curve is observed in $Pr_7Tb_1Fe_{87}Nb_1B_4$ samples, resulting in the degradation of energy product in spite of its high

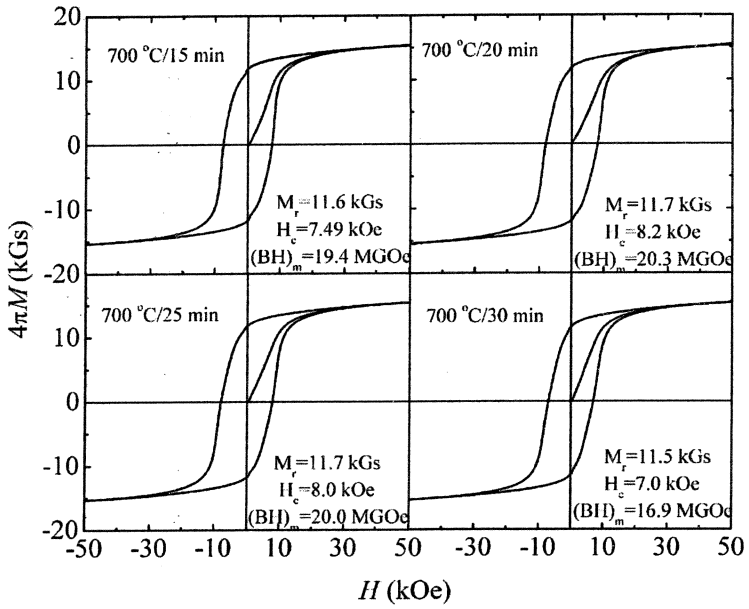

Fig. 6. Hysteresis loops of annealed $Pr_7Tb_1Fe_{87}Nb_{0.5}Zr_{0.5}B_4$ ribbons spun at 14 m/s.

Table 1
$4\pi M_r$, M_r/M_s, H_c and $(BH)_m$ of $Pr_7Tb_1Fe_{88-x-y}Nb_xZr_yB_4$ ($x = 0-2$; $y = 0-1$) ribbons after optimal thermal treatment

Compositions	$4\pi M_r$ (kGs)	M_r/M_s	H_c (kOe)	$(BH)_m$ (MGOe)
$Pr_7Tb_1Fe_{88}B_4$	10.7	0.63	5.6	14.7
$Pr_7Tb_1Fe_{87}Nb_1B_4$	10.4	0.65	7.3	14.5
$Pr_7Tb_1Fe_{86}Nb_2B_4$	10.1	0.65	7.7	14.2
$Pr_7Tb_1Fe_{87}Nb_{0.5}Zr_{0.5}B_4$	11.7	0.73	8.2	20.3
$Pr_7Tb_1Fe_{86.5}Nb_{0.5}Zr_1B_4$	11.4	0.69	7.4	17.7
$Pr_7Tb_1Fe_{86.5}Nb_1Zr_{0.5}B_4$	11.2	0.70	7.5	17.5
$Pr_7Tb_1Fe_{86.5}Nb_1Zr_1B_4$	10.8	0.70	6.6	16.7

coercivity. Fig. 7 also shows an enhanced hysteresis squareness of the samples containing small amount of both Nb and Zr. The introduction of Zr leads to a more square demagnetization curve. It is also noteworthy that the initial susceptibility decreases with the substitutions, which is consistent with the higher coercivity of substituted samples.

Fig. 8 shows the TEM micrographs of the samples investigated. Selected area electron diffraction confirms the existence of 2:14:1 and α-Fe nanocrystallites with an average grain size of 35 nm in $Pr_7Tb_1Fe_{88}B_4$ samples. Some irregular grain shape and large grain clusters have been observed for both the hard and soft magnetic phases in $Pr_7Tb_1Fe_{87}Nb_1B_4$ samples, where the cluster size exhibits a broader distribution from 25 to 80 nm. In the case of the irregular structure, there exist sharp edges which lead to an inhomogeneous magnetization distribution [16]. Whereas the magnetization remains parallel to the easy axis in the center of the grains, it deviates from the local easy axis at the vicinity of the grain boundaries, resulting in a broader distribution of magnetization. Schrefl et al. [9] has also noted that M_r and H_c change with grain size variations. As a consequence, the "slanted" demagnetization curve observed in Fig. 7 can be attributed to an assembly

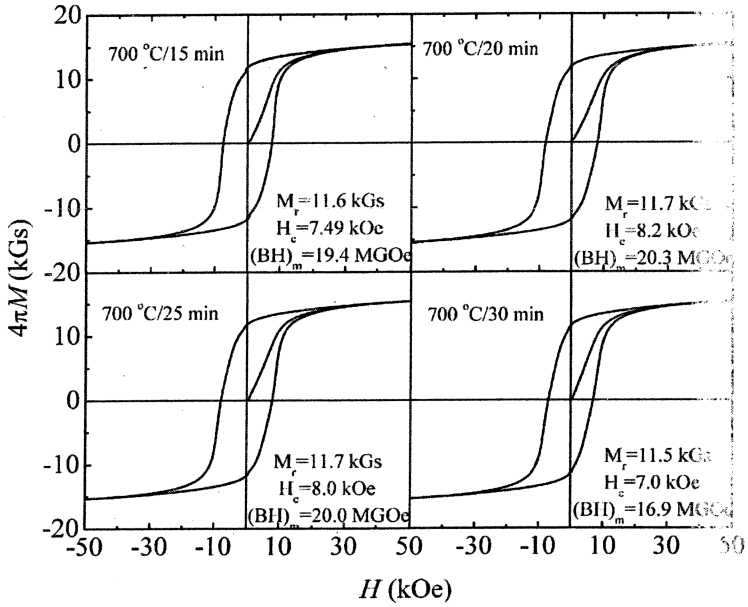

Fig. 6. Hysteresis loops of annealed $Pr_7Tb_1Fe_{87}Nb_{0.5}Zr_{0.5}B_4$ ribbons spun at 14 m/s.

Table 1
$4\pi M_r$, M_r/M_s, H_c and $(BH)_m$ of $Pr_7Tb_1Fe_{88-x-y}Nb_xZr_yB_4$ ($x = 0-2$; $y = 0-1$) ribbons after optimal thermal treatment

Compositions	$4\pi M_r$ (kGs)	M_r/M_s	H_c (kOe)	$(BH)_m$ (MGOe)
$Pr_7Tb_1Fe_{88}B_4$	10.7	0.63	5.6	14.7
$Pr_7Tb_1Fe_{87}Nb_1B_4$	10.4	0.65	7.3	14.5
$Pr_7Tb_1Fe_{86}Nb_2B_4$	10.1	0.65	7.7	14.2
$Pr_7Tb_1Fe_{87}Nb_{0.5}Zr_{0.5}B_4$	11.7	0.73	8.2	20.3
$Pr_7Tb_1Fe_{86.5}Nb_{0.5}Zr_1B_4$	11.4	0.69	7.4	17.7
$Pr_7Tb_1Fe_{86.5}Nb_1Zr_{0.5}B_4$	11.2	0.70	7.5	17.5
$Pr_7Tb_1Fe_{86.5}Nb_1Zr_1B_4$	10.8	0.70	6.6	16.7

coercivity. Fig. 7 also shows an enhanced hysteresis squareness of the samples containing small amount of both Nb and Zr. The introduction of Zr leads to a more square demagnetization curve. It is also noteworthy that the initial susceptibility decreases with the substitutions, which is consistent with the higher coercivity of substituted samples.

Fig. 8 shows the TEM micrographs of the samples investigated. Selected area electron diffraction confirms the existence of 2:14:1 and α-Fe nanocrystallites with an average grain size of 35 nm in $Pr_7Tb_1Fe_{88}B_4$ samples. Some irregular grain shape and large grain clusters have been observed for both the hard and soft magnetic phases in $Pr_7Tb_1Fe_{87}Nb_1B_4$ samples, where the cluster size exhibits a broader distribution from 25 to 80 nm. In the case of the irregular structure, there exist sharp edges which lead to an inhomogeneous magnetization distribution [16]. Whereas the magnetization remains parallel to the easy axis in the center of the grains, it deviates from the local easy axis at the vicinity of the grain boundaries, resulting in a broader distribution of magnetization. Schrefl et al. [9] has also noted that M_r and H_c change with grain size variations. As a consequence, the "slanted" demagnetization curve observed in Fig. 7 can be attributed to an assembly

of irregular grains with differing coercivity and magnetization ratio (M_r/M_s). It was predicted [16] that a large stray field originating from the edges of irregular grains might reduce the coercivity. However, it is noteworthy that a high coercivity of 7.3 kOe can still be obtained in $Pr_7Tb_1Fe_{87}Nb_1B_4$.

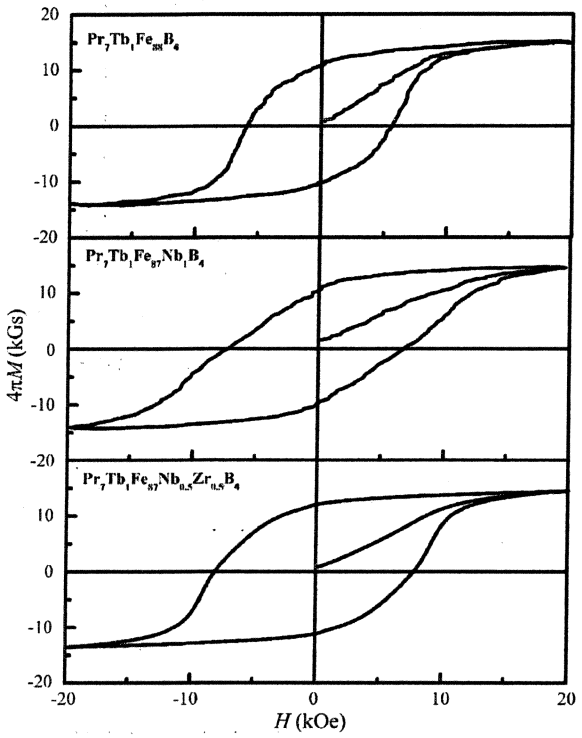

Fig. 7. Typical hysteresis loops of $(Pr,Tb)_8(Fe,Nb,Zr)_{88}B_4$ samples.

It appears that the Nb addition allows large grains to exist in nanocomposites without loosing H_c. Previous studies have shown that Nb preferably segregates at grain boundaries to form Nb-rich intergranular phase instead of entering the $Pr_2Fe_{14}B$ matrix [17]. This intergranular phase separates adjacent grains and thus decouples the exchange interaction, leading to a decrease in M_r/M_s and to an increase of H_c from 5.6 kOe for $Pr_7Tb_1Fe_{88}B_4$ to 7.3 kOe for $Pr_7Tb_1Fe_{87}Nb_1B_4$.

To obtain higher remanence and preserve a high coercivity in nanocomposite magnets, a small mean grain size is necessary due to the limited range of exchange interaction. The Zr additions appear to be very successful in suppressing the grain growth during crystallization (Fig. 8). A much finer and uniform microstructure has been found in $Pr_7Tb_1Fe_{87}Nb_{0.5}Zr_{0.5}B_4$ sample with an average grain size around 20 nm. The most remarkable characteristic of this sample is the formation of grains with smooth spherical-like shape. Moreover, the α-Fe grains are found to be distributed separately within the matrix as isolated particles. The overall uniform and narrow distribution of such a fine grain size with spherical-like shape contributes to the significant enhancement of exchange coupling between 2:14:1 and α-Fe, leading to a more rectangular hysteresis loop. The exchange coupling in nanocomposites magnetic materials can be investigated with the Henkel plot using $\delta M-H$ curves [10,18,19]. The δM is denoted as $m_d(H)-(1-2m_r(H))$ where $m_r(H)$ is the reduced initial remanence and $m_d(H)$ the reduced magnetization remanence. A positive

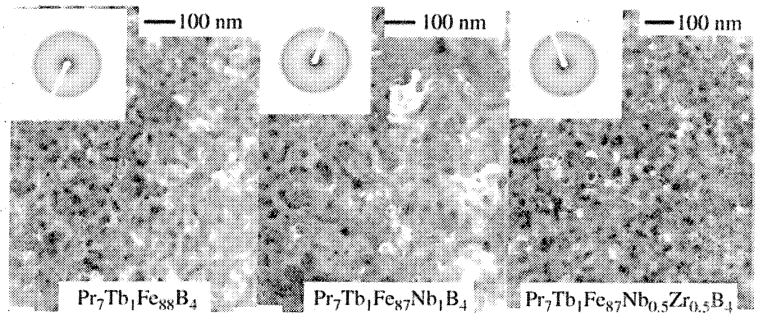

Fig. 8. TEM micrographs of optimally annealed $(Pr,Tb)_8(Fe,Nb,Zr)_{88}B_4$.

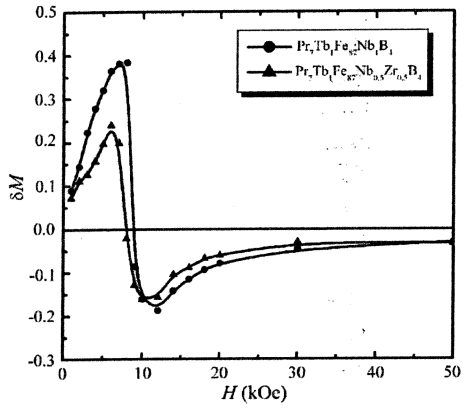

Fig. 9. δM as a function of applied field for annealed $(Pr,Tb)_8(Fe,Nb,Zr)_{88}B_4$ samples.

δM has been observed in all the samples indicating the existence of exchange coupling between the hard and soft phases [19,20]. Fig. 9 gives the typical results for Nb-added and (Nb,Zr)-added samples. A higher δM peak for (Nb,Zr)-added samples has been observed suggesting a stronger exchange coupling. This explains why small amounts of Nb and Zr substitutions contribute to the much higher improvement in coercivity and energy product among the samples investigated.

4. Conclusions

In conclusion, the magnetic properties of $(Pr,Tb)_2(Fe,Nb,Zr)_{14}B/\alpha$-Fe nanocomposites have been significantly improved by the addition of small amounts of Nb and Zr. A strong texture was developed in the as-quenched samples. The "slanted" loop squareness in the Nb-added sample originates from the irregular grain shape and broader grain size distribution, which can be significantly improved with a slight substitution of Zr. An approximate 50% enhancement in the coercivity and maximum energy product has been observed in $Pr_7Tb_1Fe_{87}Nb_{0.5}Zr_{0.5}B_4$, which is attributed to the drastic enhancement of exchange coupling due to the significant refinement of microstructure and the homogeneous distribution of α-Fe grains.

Acknowledgements

This work was supported by DARPA-Meta-Materials Program and Santoku America Inc.

References

[1] R. Skomski, J.M.D. Coey, Phys. Rev. B 48 (1993) 15812.
[2] L. Withanawasam, A.S. Murphy, G.C. Hadjipanayis, R.F. Krause, J. Appl. Phys. 76 (1994) 7065.
[3] Y.Q. Wu, D.H. Ping, K. Hono, M. Hamano, A. Inoue, J. Appl. Phys. 87 (2000) 8658.
[4] Z.M. Chen, H. Okumura, G.C. Hadjipanayis, Q. Chen, J. Appl. Phys. 89 (2001) 2299.
[5] V. Neu, L. Schultz, J. Appl. Phys. 90 (2001) 3340.
[6] Z.Q. Jin, H. Okumura, G.C. Hadjipanayis, IEEE Trans. Magn. 37 (2001) 2564.
[7] W. Zhang, A. Inoue, J. Appl. Phys. 89 (2001) 3509.
[8] J.H. Yin, B.G. Shen, D.H. Wang, X.B. Yin, M. Wang, Y.W. Du, J. Alloys Compounds 316 (2001) 296.
[9] T. Schrefl, J. Fidler, H. Kronmüller, Phys. Rev. B 49 (1994) 6100.
[10] Z.M. Chen, H. Okumura, G.C. Hadjipanayis, Q. Chen, J. Alloys Compounds 327 (2001) 201.
[11] Z.M. Chen, Y. Zhang, Y.Q. Ding, G.C. Hadjipanayis, Q. Chen, B.M. Ma, J. Appl. Phys. 85 (2001) 5908.
[12] P.G. McCormick, W.F. Miao, P.A.I. Smith, J. Ding, R. Street, J. Appl. Phys. 83 (1998) 6256.
[13] X.Y. Zhang, Y. Guan, L. Yang, J.W. Zhang, Appl. Phys. Lett. 79 (2001) 2426.
[14] T. Shima, A. Kamegawa, K. Hono, H. Fujimori, Appl. Phys. Lett. 78 (2001) 2049.
[15] Z.Q. Jin, H. Okumura, H.L. Wang, J.S. Muñoz, V. Papaefthymiou, G.C. Hadjipanayis, J. Magn. Magn. Mater. 242–245 (2002) 1307.
[16] R. Fischer, T. Schrefl, H. Kronmuller, J. Fidler, J. Magn. Magn. Mater. 153 (1996) 35.
[17] Z.M. Chen, Y. Zhang, Y.Q. Ding, G.C. Hadjipanayis, Q. Chen, B.M. Mao, J. Magn. Magn. Mater. 195 (1999) 420.
[18] Q. Chen, B.M. Ma, B. Lu, M.Q. Huang, D.E. Laughlin, J. Appl. Phys. 85 (1999) 5917.
[19] J. García-Otero, M. Porto, J. Rivas, J. Appl. Phys. 87 (2000) 7376.
[20] P.E. Kelly, K.O. Grady, P.I. Mayo, R.W. Chantrell, IEEE Trans. Magn. 25 (1989) 3881.

Synthesis and magnetic behavior of $SmCo_{5(1-x)}Fe_x$ nanocomposite magnets

Shaoyan Chu[a] and Sara A. Majetich
Carnegie Mellon University, 5000 Forbes Avenue, Pittsburgh, Pennsylvania 15213-3890

Meiqing Huang
UES Inc., 4401 Dayton-Xenia Road, Dayton, Ohio 45432

Richard T. Fingers
AFRL, Wright-Patterson AFB, Dayton, Ohio 45433

(Presented on 14 November 2002)

$SmCo_{5(1-x)}Fe_x$ ($x=0.2$, 0.4, 0.6, and 0.7) nanocomposites were synthesized by ball milling a mixture of $SmCo_5$ and nanosize iron powders. Composites were made using different kinds of soft ferromagnetic phase nanoparticles, either α-Fe crystallized from amorphous iron generated by sonochemical decomposition of $Fe(CO)_5$, or acicular metallic iron particles with an average length of 200 nm and average diameter of 18 nm. After milling the powder mixtures were compacted by hot isostatic pressing at 3000 psi for ~5 min at a temperature of 530–570 °C. The compacted solids were magnetically characterized between 5 and 300 K. Hysteresis loop measurements and recoil measurements for the $(SmCo_5)_{0.8}$/acicular-$Fe_{0.2}$ composite show stronger magnetic coupling when compared with the properties of $(SmCo_5)_{0.8}$/amorphous-$Fe_{0.2}$, am-Fe coated $SmCo_5$, and pure $SmCo_5$ powders alone. © *2003 American Institute of Physics.* [DOI: 10.1063/1.1544511]

I. INTRODUCTION

Exchange-spring magnetic materials[1] have the potential to substantially increase the energy product and the reversible component of the magnetization in permanent magnets, and there have been many efforts to prepare them.[2–6] For an ideal exchange-spring magnet, the soft ferromagnetic phase should be within an exchange length L_{ex} of the hard ferromagnetic phase,[7] so understanding how to make nanocomposites of these materials is crucial. Coating ball-milled $SmCo_5$ powder with amorphous Fe (am-Fe),[8] was shown to increase the reversible magnetization, indicating some degree of magnetic coupling in the composite powders. Here we examined the magnetic behavior of powders compacted by hot isostatic pressing (HIP), both mixtures of $SmCo_5$/am-Fe and $SmCo_5$/acicular α-iron nanoparticles.

II. EXPERIMENT

Commercial acicular metallic iron (aci-Fe) particles used in this work were prepared from hydrogen reduction of Fe_2O_3 at high temperature. Nanograined, structurally disordered Fe was synthesized sonochemically.[9–13] Details of this synthesis are found in Ref. 8. To produce the am-Fe, a reaction vessel was filled with pure liquid $Fe(CO)_5$ under an argon atmosphere. It was then exposed for a few hours to ultrasound at 20 kHz with a power density of ~100 W/cm^3, generated by a sonic dismembrator. The solid particles were magnetically separated from the remains of liquid phase, $Fe(CO)_5$ and then washed by pentane more than ten times, all under an inert atmosphere. After drying under mechanical pump vacuum, the fine powder was mixed with commercially available $SmCo_5$ powder (Alfa Aesar, −30 Mesh) and sealed in a Pyrex ampoule containing ZrO_2 balls under Ar. The typical grain size of the milled $SmCo_5$ powder was 25–100 nm, and the typical particle size was ~1 μm after ball milling in a rolling mill for roughly one week.

Seamless stainless steel 304 tubing (0.3750 in. diameter, 0.010 in. wall thickness) was used to seal the powder mixtures for HIP compaction. The tubing was evacuated to a base pressure below 10^{-5} Torr and then sealed under argon. Because of the oxidation sensitive $SmCo_5$ phase, the powder was always kept under argon using a glove box or a glove bag. A magnetic field up to 9 T was applied to align the magnetic particles prior to compaction. The maximum temperature and pressure attained during HIP consolidation were 550±30 °C and 3000 psi. The heat treatment time of ~5 min was kept as short as possible to minimize grain growth.

Magnetic properties were measured in the temperature range of 5–300 K and at fields up to 50 kOe, using a superconducting quantum interference device magnetometer. The compacted samples were either in bulk chunks, or were ground and magnetically oriented. To magnetically orient powder samples, the powders were ground to <38 μm, mixed with epoxy, and allowed to harden in a 20 kOe field. The samples used in the magnetic measurements had a width to thickness ratio of at least 15:1, so that the demagnetization corrections were negligible. For the recoil measurements, a saturating a reverse field was applied and reduced to zero, and then the magnetization was recorded.

[a]Electronic mail: sm70@andrew.cmu.edu

0021-8979/2003/93(10)/8146/3/$20.00

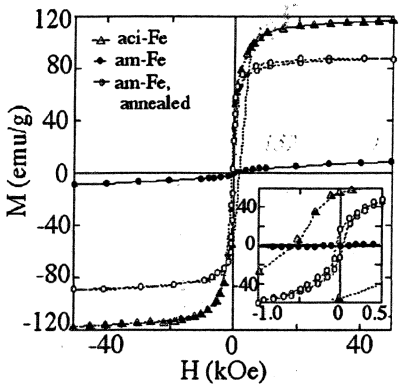

FIG. 1. Field dependence of the magnetization at 293 K for powder samples of acicular Fe, and for amorphous Fe before and after annealed at 320 °C for 1 h.

III. RESULTS AND DISCUSSION

A. Magnetic properties of the constitutent materials, Fe and $SmCo_5$

The magnetization curves of the different types of Fe nanoparticles are shown in Fig. 1. The saturation magnetization, M_s, and the coercivity, H_c, of commercial aci-Fe nanoparticles used here were ~114 emu/g and ~500 Oe, respectively. The reduced moment of the aci-Fe relative to that of bulk α-Fe is attributed to surface oxidation and the presence of impurities. The saturation magnetization, M_s, of am-Fe nanoparticles can vary from a few emu/g to ~120 emu/g depending on the size, crystallinity, and contaminants.[9–13] As made, the am-Fe was superparamagnetic at room temperature. However, after annealing at 320 °C for 1 h to improve the crystallinity, the sample has an M_s of ~88 emu/g and a H_c less than 50 Oe.

The magnetic properties of the ball-milled $SmCo_5$ powder alone are included in Fig. 2. At 293 K, M_s was ~76 emu/g, and the coercivity, H_c, was ~11.5 kOe. We have previously obtained higher coercivity in pure ball-milled $SmCo_5$;[14] however, the 11.5 kOe value refers to a sample treated with the same processing conditions as those of the composite materials.

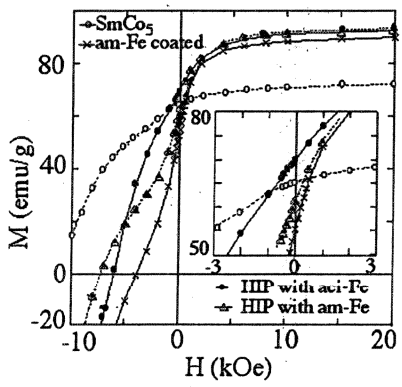

FIG. 2. Hysteresis loops for $(SmCo_5)_{0.8}/am\text{-}Fe_{0.2}$ and $(SmCo_5)_{0.8}/aci\text{-}Fe_{0.2}$ mixed powders after a HIP heat treatment. For comparison, data for annealed, uncompacted am-Fe coated $SmCo_5$, and pure ball-milled $SmCo_5$ alone are also shown.

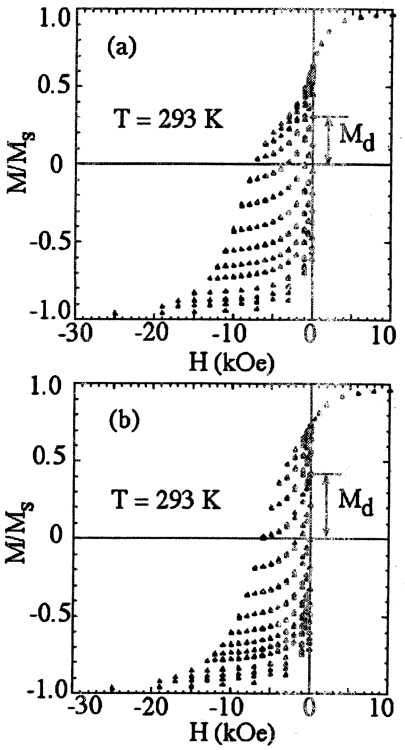

FIG. 3. Recoil measurements for the HIP compacted samples of $(SmCo_5)_{0.8}/aci\text{-}Fe_{0.2}$ (a) and $(SmCo_5)_{0.8}/am\text{-}Fe_{0.2}$ (b). After saturating a reverse field was applied and then reduced to zero.

B. Magnetic properties of the $SmCo_5$/Fe compacted nanocomposites

Figure 2 also shows hysteresis loops for the $(SmCo_5)_{0.8}/am\text{-}Fe_{0.2}$ and $(SmCo_5)_{0.8}/aci\text{-}Fe_{0.2}$ magnetically oriented powder samples after HIP heat treatment. The heat treatment enhanced M_s, but unfortunately also reduced the coercivity, in comparison with the original ball-milled $SmCo_5$. A significant increase in M_r and nearly single-phase magnetic behavior are seen for the $(SmCo_5)_{0.8}/aci\text{-}Fe_{0.2}$ sample, implying stronger magnetic coupling between the soft and hard phases. The $(SmCo_5)_{0.8}/am\text{-}Fe_{0.2}$ sample has a larger coercivity, but it shows two-phase behavior and has a reduced remanence. Similar qualities were also noted in am-Fe-coated $SmCo_5$ powders.[8] In the acicular Fe particles, the diameter is on the order of the exchange length, and it is fairly uniform. While the 4–5 nm grain size of the amorphous Fe is also uniform, the am-Fe coating on the ball-milled $SmCo_5$, or am-Fe cluster contains many layers of grains and varies in thickness. As a result, when a local dimension of the α-Fe phase exceeds the exchange length L_{ex} (~15 nm)[7] of the $SmCo_5$ phase, the exchange coupling between these two phases will be no longer effective. Similarly, the ball milled $SmCo_5$ has small grains but not a small average particle size, so much of the hard phase is beyond an exchange length of the soft Fe phase. Some anisotropy was observed in the magnetically aligned, compacted samples, and a more detailed study of this effect will be the subject of a future publication.

Recoil measurements for the compacted samples $SmCo_5$/Fe were carried out to quantify the degree of mag-

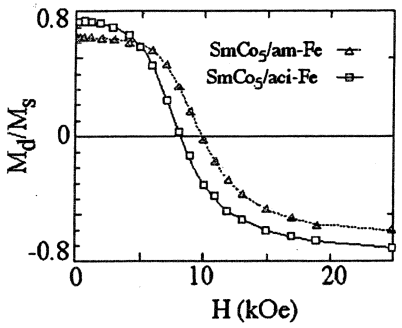

FIG. 4. Field dependence of reversible magnetization M_d/M_s of compacted samples of $(SmCo_5)_{0.8}$/aci-$Fe_{0.2}$ and $(SmCo_5)_{0.8}$/am-$Fe_{0.2}$.

netic coupling. Figures 3(a) and 3(b) present recoil results for the sample used in Fig. 2. In each of the recoil loops the data indicates that the reversible magnetization, M_d, is a reasonable fraction of M_s, as shown in Fig. 4. At lower fields (<5 kOe), the value of M_d in $(SmCo_5)_{0.8}$/aci-$Fe_{0.2}$, is clearly larger than that in $(SmCo_5)_{0.8}$/am-$Fe_{0.2}$. This also indicates that there is stronger magnetic coupling between the acicular Fe and the $SmCo_5$ phases. Experiments are underway to determine the relative importance of pinning and nucleation to the coercivity.

Single-phase magnetic behavior seen from the hysteresis loops and recoil curves of compacted $(SmCo_5)_{0.8}$/aci-$Fe_{0.2}$ by no means implies a single phase in the microstructure. Figure 5 shows that this sample has two-phase magnetic behavior at low temperature, suggesting that the HIP heat treatment did not product a new chemical phase in this system. Under the same HIP conditions, the saturation magnetization M_s increases monotonically with increasing soft phase content, within the experimental window of $SmCo_{5(1-x)}Fe_x$ ($x=0.2$, 0.4, 0.6, and 0.7). At the same time, H_c decreases with increasing soft phase content. The ball milling time and the HIP conditions may need to be adjusted to optimize the properties.

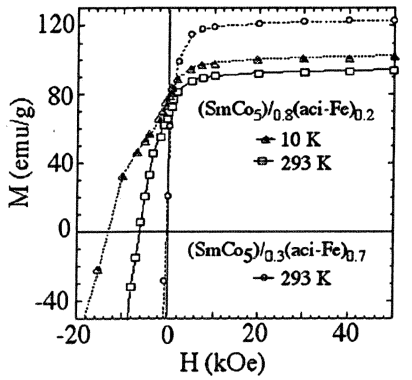

FIG. 5. Hysteresis loops for $(SmCo_5)_{0.8}$/aci-$Fe_{0.2}$ at 10 and 293 K as well as $(SmCo_5)_{0.3}$/aci-$Fe_{0.7}$ at 293 K mixed powders after a HIP heat treatment.

IV. SUMMARY

We have described the compaction of $SmCo_{5(1-x)}Fe_x$ made from ball-milled $SmCo_5$ and different types of Fe nanoparticles. Hysteresis loop and recoil measurements for the $(SmCo_5)_{0.8}$/aci-$Fe_{0.2}$ composites show improved magnetic coupling compared with composites of $(SmCo_5)_{0.8}$/am-$Fe_{0.2}$, am-Fe coated $SmCo_5$, and pure $SmCo_5$.

ACKNOWLEDGMENTS

This work was supported by DARPA/AFoSR under Grant No. F33615-01-2-2166, NSF Grant No. DMR-9900550, and Propulsion Directorate Summer Faculty Research Program (C2006-18) under the administrator of Ball Aerospace & Technologies Corp.

[1] E. F. Kneller and R. Hawing, IEEE Trans. Magn. **27**, 3588 (1991).
[2] R. Coehoorn, D. B. De Mooij, and C. De Waard, J. Magn. Magn. Mater. **80**, 101 (1989).
[3] J. Ding, P. G. McCormick, and R. Street, J. Magn. Magn. Mater. **124**, 1 (1993).
[4] G. C. Hadjipanayis, J. Magn. Magn. Mater. **200**, 373 (1999).
[5] J. Zhang, S.-Y. Zhang, H.-W. Zhang, and B.-G. Shen, J. Appl. Phys. **89**, 5601 (2001).
[6] M. Ito, K. Majima, T. Umemoto, S. Katsuyama, and H. Nagai, J. Alloys Compd. **329**, 272 (2001).
[7] E. E. Fullerton, J. S. Jiang, and S. D. Bader, J. Magn. Magn. Mater. **200**, 392 (1999).
[8] S. Chu and S. A. Majetich, 17th International Workshop on Rare-Earth Magnets and Their Applications, 18–22 August 2002, Newark, Delaware.
[9] K. S. Suslick, S. B. Choe, A. A. Cicholas, and M. W. Grinstaff, Nature (London) **353**, 414 (1991).
[10] R. Bellissent *et al.*, Phys. Scr., T **T57**, 79 (1995).
[11] R. Bellissent, G. Galli, M. W. Grinstaff, P. Migliardo, and K. S. Suslick, Phys. Rev. B **48**, 15797 (1993).
[12] K. V. P. M. Shafi, A. Gedanken, R. B. Goldfarb, and I. Felner, J. Appl. Phys. **81**, 6901 (1997).
[13] G. J. Long *et al.*, Phys. Rev. B **57**, 10716 (1998).
[14] S. A. Majetich, K. M. Chowdary, and E. M. Kirkpatrick, IEEE Trans. Magn. **34**, 985 (1998).

Fabrication of Sm–Co/Co (Fe) composites by electroless Co and Co–Fe plating

Q. Zeng,[a] Y. Zhang, M. J. Bonder, and G. C. Hadjipanayis
Department of Physics and Astronomy, University of Delaware, Newark, Delaware 19716

(Presented on 12 November 2002)

Sm–Co/Co and Sm–Co/Fe–Co nanocomposites have been fabricated by electroless plating of Sm–Co powders with Co and Co–Fe, respectively. The influence of electroless plating conditions on the magnetic properties and structure of the coatings were studied. The saturation magnetization (M_s) and morphology of the deposited material were found to be dependent on the concentration of hypophosphite, the temperature of the solution, and plating time. By plating at an elevated temperature and decreasing the $NaH_2PO_2 \cdot H_2O$ concentration of the bath, the phosphorus content decreases, and it is possible to form Co particles with a M_s of up to 142 emu/g as compared to 160 emu/g for bulk Co. For 50 μm $Sm(Co,Cu,Fe,Zr)_{7.5}$ particles, coating with Co has had little effect on the coercivity, maintaining a value of 7 kOe, while there is a substantial increase in the value of M_s that varies with Co plating time. However, $SmCo_5$ particles with a size of a few microns, plating with the bcc Co–Fe alloy increases M_s significantly, at the expense of the coercivity which decreases drastically. © *2003 American Institute of Physics.* [DOI: 10.1063/1.1558246]

I. INTRODUCTION

Nanocomposite magnets are based on interfacial exchange coupling between magnetically hard and soft materials.[1] In principle, the hard phase supplies the high magnetic anisotropy to resist magnetization reversal, while the soft phase provides the high magnetization necessary for remanence which results in a high energy product magnet. These magnets have been fabricated mainly by rapid-quenching and subsequent annealing or mechanical alloying.[2–5] However, these techniques yield nanocomposites with randomly dispersed and randomly oriented hard grains. Their maximum energy product $(BH)_{max}$, although improved over single phase isotropic hard magnets, is still significantly lower than that of oriented single-phase magnets. The current challenge is to come up with a synthesis route that imparts improved crystallographical alignment of the high anisotropy phase. The fabrication of magnetically soft nanoparticles on the surface of hard particles is a key step in producing bulk high energy product composite magnets.[6]

It is well known that electroless plating is used to produce uniformly thick, hard, and adhesive coatings on a wide variety of substrate materials. In this article we present a simple and economical way of fabricating Co and Co–Fe nanoparticles deposited on the surface of anisotropic Sm–Co hard powders by electroless plating from an alkaline solution containing hypophosphite which is used as a reducing agent.

II. EXPERIMENT

Two kinds of pulverized powder alloys having a nominal composition of $Sm(FeCoCuZr)_{7.5}$ and $SmCo_5$ with average particle sizes of 50 and 1.5 μm, respectively, were used as the precursors for plating. Initially Co and Co–Fe were electrolessly plated onto chemically polished Cu substrates activated by Pd^{2+} to optimize the bath composition. Sm–Co powders were degreased in acetone solution at room temperature and activated in a solution of 0.5 M sodium hypophosphite at 90 °C before plating. The Sm–Co powders were then introduced to the plating baths as shown in Table I.

TABLE I. Composition of plating bath and plating conditions.

	Co–P		Co–Fe–P	
Purpose	Compound	Conc ($moll^{-1}$)	Compound	Conc ($moll^{-1}$)
Cobalt/Iron source	$CoSO_4 \cdot 7H_2O$	0.05–0.8	$CoSO_4$ /$FeSO_4$	0.09/0.07
Reducing agent	$NaH_2PO_2 \cdot H_2O$	0.3–1.5	$NaH_2PO_2 \cdot H_2O$	0.3–0.6
Complexing agent	$Na_3C_6H_5O_7 \cdot 2H_2O$	0.5	$Na_3C_6H_5O_7 \cdot 2H_2O$	0.1–0.5
Buffer	$(NH_4)_2SO_4$	0.1	$(NH_4)_2SO_4$	0.05–0.3
*p*H	8–12			
Temperature	30–90 °C			
Time	0–2 h			

[a]Author to whom correspondence should be addressed; electronic mail: qizeng@udel.edu

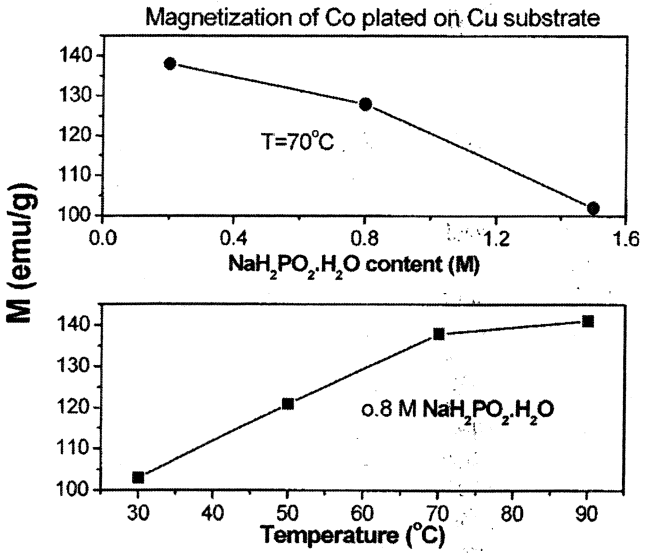

FIG. 1. Effect of plating temperature and reducing agent composition on the magnetization of Co deposits.

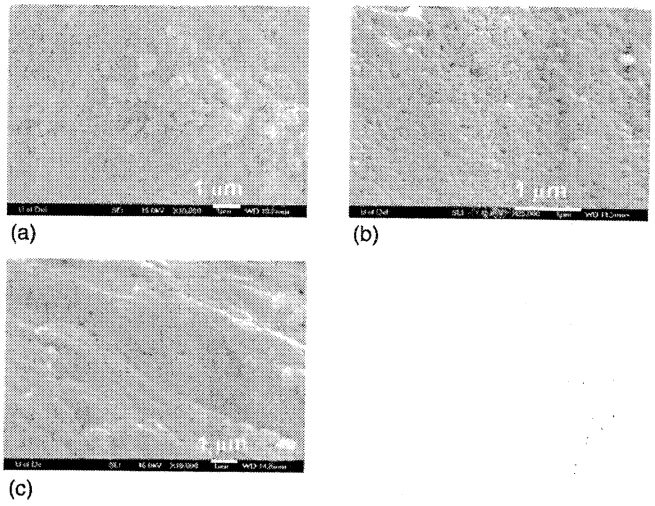

FIG. 3. Evolution of Co deposit microstructure during electroless plating of Co on $Sm(Co,Cu,Fe,Zr)_{7.5}$ powders: (a) 5 min; (b) 1 h; (c) 2 h.

After plating, the encapsulated Sm–Co powders were rinsed with de-ionized water and acetone solution, and dryed in a glove box filled with argon.

The composition and surface morphology of the deposited materials were analyzed by scanning electron microscopy with energy dispersive x-ray spectroscopy (EDS). The crystal structure was determined by x-ray diffraction with a Cu $K\alpha$ radiation. Magnetic measurements were made using a vibrating sample magnetometer.

III. RESULTS AND DISCUSSION

The effect of temperature and composition of reducing agent on the saturation magnetization of the deposits was studied on Cu substrates plated with Co particles. The results of Fig. 1 show that a higher temperature and lower concentration of the reduction solution ($NaH_2PO_2 \cdot H_2O$) increase the saturation magnetization of Co particles due to the decrease in phosphorus content. EDS studies show that the phosphorus content is 3–6 at. % for Co plating, while in the case of Fe–Co plating, it is 1–2.5 at. %. The highest value of M_s obtained so far for Co-plating is 142 emu/g. Annealing at temperatures in the range of 350–500 °C further increased the saturation magnetization. Similar increase of M_s was earlier observed during annealing of Co–Ni–P,[7,8] which was accompanied by appearance of the Co_2P and Ni_2P. Although we did not observe clear Co_2P peak in our x-ray diffraction (XRD) data, one can suppose that this phase does form together with pure Co. Since Co_2P is only weakly ferromagnetic, one can also suppose that Co+Co_2P mixture has higher saturation magnetization than the supersaturated Co(P) solid solution. On the other hand, the observed increase of M_s can be a result of perfection of Co crystal structure by the annealing.

X-ray diffraction patterns of the powders plated for 2 h are shown in Fig. 2 along with the spectrum of the original $SmCo_5$ particles. As can be seen, the strong peaks of hexagonal Co and bcc Co–Fe solid solution appear, while the peaks of $SmCo_5$ peaks decrease sharply. This indicates the formation of very thick Co and Co–Fe deposits on the $SmCo_5$ powder surface. According to PDF database and EDS analysis, the Co–Fe layer has composition close to

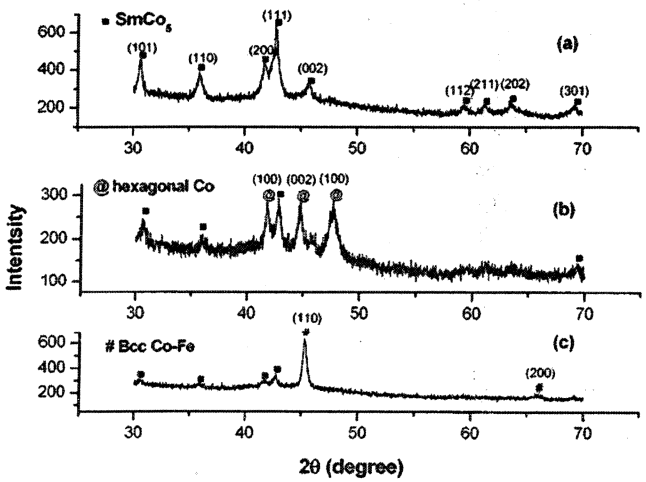

FIG. 2. X-ray diffraction patterns of (a) $SmCo_5$ powders; (b) with Co plating for 2 h; and (c) with Fe–Co plating for 2 h.

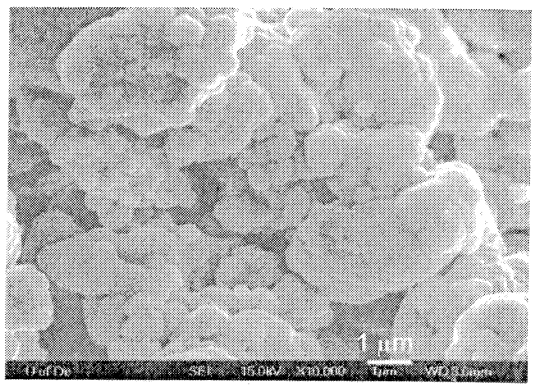

FIG. 4. Microstructure of Co–Fe alloy deposits on the surface of $SmCo_5$ powders.

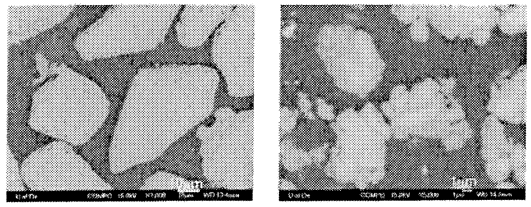

FIG. 5. Backscattered SEM structure of Fe–Co coated Sm–Co particles: (a) 50 μm; (b) 1.5 μm.

$Co_{70}Fe_{30}$. In fact, this phase may also have an ordered structure with higher saturation magnetization. This, however, could not be confirmed by XRD because the ordered Co–Fe has very low intensities of the superstructural peaks.

Figure 3 shows the evolution of the Co deposit microstructure at the different stages of plating. In the initial stage, the coating is not continuous, but the particles are very uniform with the size of 50–100 nm. However, extended plating time results in a much smoother surface [Fig. 3(c)]. In the case of Co–Fe deposits, continued plating results in particle agglomeration with a Co–Fe average particle size of more than 100 nm (Fig. 4). Typical cross-sectional structures showing the Co–Fe plating thickness are given in Fig. 5. Both of the images show a uniform Co–Fe layer regardless of initial Sm–Co particle size.

Figures 6 and 7 show the hysteresis loops of Co-encapsulated $Sm(CoFeZrCu)_{7.5}$ and Co-Fe-encapsulated $SmCo_5$ composites, respectively. As can be seen for the case of the Co plating, the saturation magnetization increases while the coercivity remains the same throughout the sample set. A smooth single switching field loop persists up to 1 h of plating as seen in Fig. 6(b), beyond which a shoulder appears in the hysteresis loop [Fig. 6(c)]. In the case of Co–Fe plating, the saturation magnetization increases more sharply than

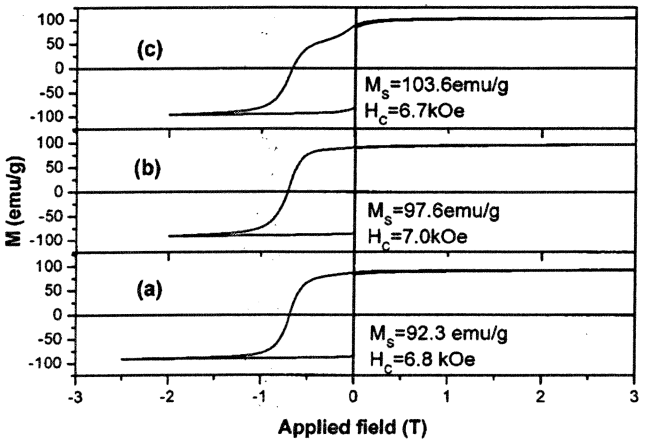

FIG. 6. Magnetic properties of Co coated $Sm(CoFeCuZr)_{7.5}$ powders (50 μm) (a) before plating; (b) after plating for 1 h; (c) after plating for 2 h.

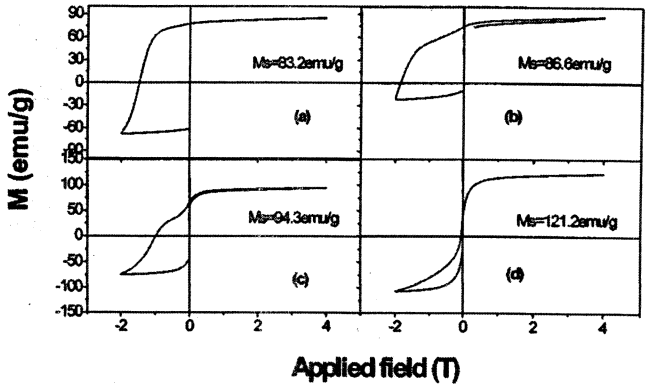

FIG. 7. Magnetic properties of Co–Fe coated $SmCo_5$ powders (1.5 μm) (a) before plating; (b) after plating for 5 min; (c) after plating for 15 min; (d) after plating for 2 h.

that of Co plating. This is easy to understand as Co–Fe has a higher magnetization than Co. However, the two materials are not exchange coupled even for the shortest times considered here. The coercivity and squareness are lost with increasing plating time. This may be in part due to the small size of the initial $SmCo_5$ particles. Different ways to improve the exchange coupling in Co (Fe) plated $SmCo_5$ particles including special compaction techniques are under way.

IV. CONCLUSION

In conclusion, we have successfully fabricated Co and Co–Fe coated anisotropic Sm–Co nanocomposites by electroless plating. As discussed in this article, this technique provides a route for increasing the energy product of Sm–Co permanent magnets with the addition of Co and Co–Fe to increase the M_s, while maintaining the high H_c. The M_s of the deposits is critically dependent on sample preparation and is a function of the phosphorus content, which in turn, is controlled by the deposition variables, primarily the solution composition, and plating temperature.

ACKNOWLEDGMENTS

Q.Z. wishes to thank Dr. Y. W. Zhao and Dr. A. M. Gaby for helpful discussion. This work was supported by the DARPA Meta-Materials program under Grant No. F 33615-01-2-2166.

[1] E. F. Kneller, R. Hawig, IEEE Trans. Magn. **27**, 3588 (1991).
[2] G. C. Hadjipanayis, J. Magn. Magn. Mater. **200**, 373 (1999).
[3] R. Coehoorn, D. B. de Mooij, and C. De Waard, J. Magn. Magn. Mater. **80**, 101 (1989).
[4] J. Ding, P. G. McCormick, and R. Street, J. Magn. Magn. Mater. **124**, L1 (1993).
[5] Q. Zeng *et al.* J. Mater. Eng. Perform. **8**, 305 (1999).
[6] S. V. Chu and S. A. Majetich, "Proceedings of the 17th International Workshop: Rare Earth Magnets and Their Application," edited by G. C. Hadjipanayis and M. J. Bonder, 2002, p. 905.
[7] K. M. Gorbunova, J. Phys. (France) **58**, 80 (1964).
[8] G. Rugo, European patent 0159600 (1985).

Topology dependence of domain wall depinning in magnetic hard–soft composites

Z. F. Lin
Bartol Research Institute, University of Delaware, Newark, Delaware 19716 and Physics Department, Fudan University, China

S. T. Chui and L. B. Hu
Bartol Research Institute, University of Delaware, Newark, Delaware 19716

(Received 6 September 2002; accepted 4 February 2003)

We study the depinning field H_d in magnetic hard–soft nanocomposite by finite-temperature Monte Carlo simulation for two different topologies of the composites: (1) a hard phase in a soft matrix and (2) a soft phase in a hard matrix. We find that the depinning field and maximum energy product is higher in the first case. The temperature and composition dependence of the switching field and maximum energy product is reported. © *2003 American Institute of Physics.*
[DOI: 10.1063/1.1563848]

I. INTRODUCTION

Bulk magnets of mixed hard and soft phases have been studied recently[1–7] because of the promise that the magnetization can be increased without substantial reduction in the coercive field, thereby increasing the energy product. Past theoretical interest focused on a coherent rotation mechanism at zero temperature.[4,5] Our recent Monte Carlo simulations at finite temperatures for multilayer systems and models of nanocomposite systems for the nucleation field H_n are consistent with zero-temperature analytic calculations.[7,8] The experimental coercive field in bulk systems is much smaller than this theoretical "nucleation" field.[2,3] In bulk experimental systems, nucleation centers such as surfaces and grain boundaries enable the initiation of the switching to bypasses the intrinsic nucleation mechanism. The *rate limiting* step may then be determined by the depinning of a domain wall. Recently, we studied a model of a soft matrix with a periodic array of aligned cubic hard magnetic inclusions.[8,9] We determined the intrinsic nucleation field H_n and the depinning field H_d at different temperatures with Monte Carlo simulations and find that H_d is approximately *5 times smaller* than H_n and has a different dependence on the amount of the soft materials. A significant temperature dependence was observed, consistent with our earlier work,[10] which focuses on the qualitative *trends* and physics of this type of problems. Two different topologies of the composite can, in principle, be made: (1) hard inclusions in a soft matrix and (2) soft inclusions in a hard matrix. In this paper, we report results of our studies on the second case and compare them with our previous results for the first case. We found that the switching field and maximum energy product is higher in the first case. We now describe our results in detail.

II. MODEL AND DETAILS

We have performed Monte Carlo simulations of a collection of Heisenberg spins under periodic boundary conditions. The interaction energy between the spins at the positions $\mathbf{R}$, $\mathbf{R}'$ is given by $U=0.5\Sigma_{i,j=x,y,z}\Sigma_{\mathrm{RR}'}V_{ij}(\mathbf{R}-\mathbf{R}')S_i(\mathbf{R})S_j(\mathbf{R}')-\Sigma_i S_i\cdot H-2K\Sigma_i S_{ix}^2$, where $V=V^d+V^e$ is the sum of the dipolar energy $V_{ij}^d(\mathbf{R})=g_{ab}\nabla_i\nabla_j(1/|\mathbf{R}_{ab}|)$ and the nearest-neighbor exchange energy $V^e=-J\delta(\mathbf{R}=\mathbf{R}'+a)\delta_{ij}$. Here a denotes the nearest-neighbor distance. $g_{ab}=M_aM_b/v$, where M_a is the magnetization of site a, and v is the unit cell volume. Experimentally, the effective parameters can exhibit temperature dependences. Part of this is electronic in origin and part of this is due to the thermal fluctuation of the spins. Starting with the above model with non-temperature-dependent parameters, one finds that as a result of thermal fluctuation the average magnetization and the effective anisotropy constant will change.[11] The change of the physical quantities due to thermal fluctuation is already included in our calculation. In our calculation, we shall assume constant parameters and ignore possible electronic contributions within the temperature range that we work in.

We have recently developed a Monte Carlo code and have investigated the micromagnetic behavior of various problems.[12] Our Monte Carlo calculation produces known results in micromagnetics in all situations that we have tested.[13–16] In particular, our simulation[7] agrees with analytic calculations for the nucleation field for multilayer structures by Skomski and Coey.[4] Thus we feel confident that the Monte Carlo technique produces reliable results for the coercive behavior of magnetic systems. Our calculation is carried out on classical three-dimensional spins (the "Heisenberg" model) on a simple cubic lattice in a box of size $L\times L\times 2L$ under periodic boundary conditions with the conventional Metropolis algorithm. Here we apply this technique to a model of a hard matrix with a periodic array of aligned soft inclusions. The pinning structure is modeled by setting the interaction constants to that of the hard phase (soft phase) for the spins in the matrix (inclusion). The inclusion is assumed to be cubes, as is described in our previous work. This is illustrated in Fig. 1 for one particular case of soft material thickness. We show different cross sections of our box. The soft magnetic material are inside the cubic inclusions for $X=7-10$ and $13-16$. Most of our calculations

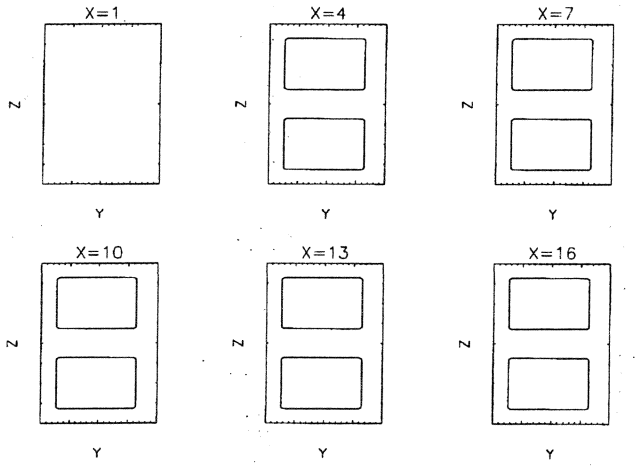

FIG. 1. The location of the hard phase as a function of z and y for $x=1$, 4, 7, 10, 13, and 16.

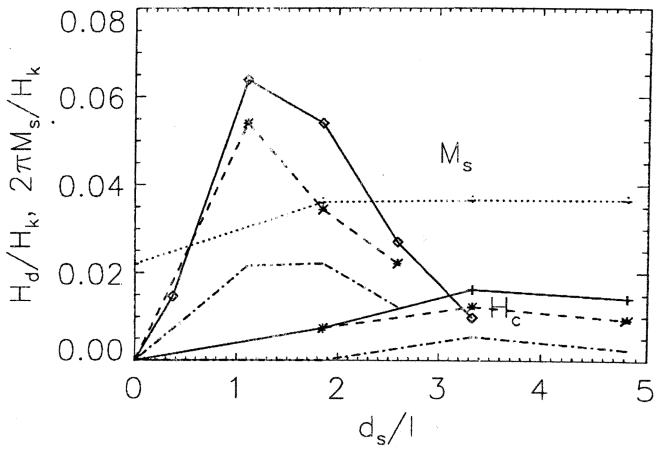

FIG. 2. The depinning field and low-temperature magnetization density $2\pi M$ (dotted line) as a function of the soft layer thickness d_s normalized by the magnetic length at three different temperatures: $T/V=0.58$ (solid line), $T/V=1.2$ (dashed line), and $T/V=2.3$ (dash-dotted line). The hard cube thickness is fixed at the magnetic length. The coercive field is normalized by the hard phase coherent switching field $H_k=2K_H$.

are performed for $L=20$. The parameters that we used are, for the soft layer, $J_s=2.2\times10^{-6}$ erg/cm, $K_s=54\times10^4$ erg/cc, and $M_s=1731$ emu/cc, and for the hard layer, $J_h=2.8\times10^{-6}$ erg/cm, $K_h=18\times10^7$ erg/cc, and $M_h=900$ emu/cc corresponding approximately to $SmCo_5$–Fe composites. The exchange between the hard and soft phases is taken to be the geometric mean of the hard phase and soft phase exchange, i.e., $J_{sh}=\sqrt{J_sJ_h}$. We have used a cubic block spin of linear dimension of 3.7 Å for both the hard and soft phases. In real experimental systems, the shape of the pinning grains may not be uniform. Nor will they be square in shape. Our goal here is not to exactly calculate the experimental switching field. Rather, our aim is to compare the relative merit of two different class of pinning structures. For this purpose, we feel that our idealized structure will be sufficient.

To determine the depinning field, we set the spins in the upper half ($z>0$) along the x direction and opposite to that of the lower half ($z<0$) at the beginning of the simulation. The system is then equilibrated in zero field. We perform simulations at increasing field strengths along the negative x direction until the switching occurs. From this, we can determine the coercive field as a function of the amount of the soft phase.

The length scale that governs the magnetic fluctuation is given by $l\approx2\sqrt{|J/M(H/2-K)|}$.[17] Near the onset of switching the magnetic field is of the order of the anisotropy of the hard magnet, $H_c\approx O(K_h)$, which is much bigger than the anisotropy constant of the soft magnet. Hence in both the hard and soft phases the length scale is of the order $l\approx2\sqrt{|2J/K_h|}\approx35.2$ Å. The pinning potential for the domain wall, V, is given by the difference of the domain wall energy between the hard and soft phases $\Delta(JK)^{0.5}$.

III. RESULTS AND CONCLUSION

The depinning field H_d normalized by the hard phase coherent switching field $H_k=2K_h$ as a function of the thickness d_s of the soft phase normalized by l is shown in Fig. 2 together with our previous results for case (1) for three temperatures $T/V=0.58$ (solid line), $T/V=1.2$ (dashed line), and $T/V=2.3$ (dash-dotted line). The lower three curves are for the present case, while the upper three curves are for case (1). Also shown is the magnetization. H_d exhibits a maximum as d_s is increased. But the position of the maximum now occurs for larger d_s. Most importantly, the switching field in the current case is much smaller.

The temperature range studied here is still much less than the Curie temperature. The corresponding magnetization exhibits a relatively small change in this temperature range just as in our previous work. (For the Heisenberg model $T_c\approx1.7$ J for a simple cubic lattice. The highest temperature we looked at here corresponds to a temperature of approximately 560 K.) On the other hand there is a substantial decrease of the depinning field (300%), even though the

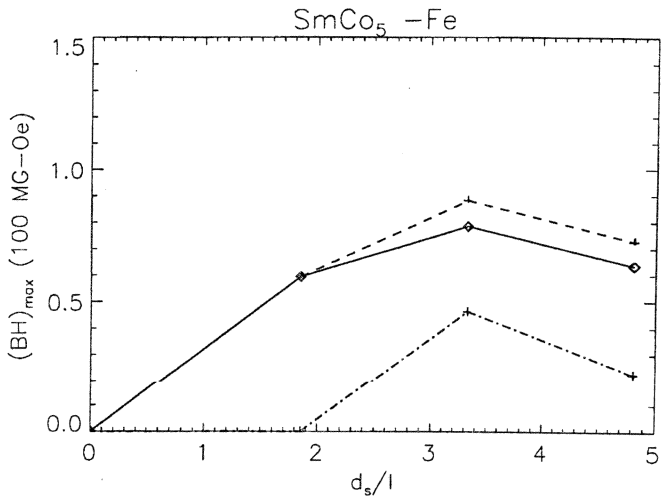

FIG. 3. The energy product for $SmCo_5$–Fe as a function of the soft layer thickness for temperatures $T/V=0.58$ (dashed line), $T/V=1.16$ (solid line), and $T/V=2.3$ (dash-dotted line).

temperature range of interest is still much less than the Curie temperature. This is because the energy scale that controls the pinning is the pinning potential, which is of the order of the difference of the domain wall energy between the soft and hard phases not the exchange alone.

The energy product is $P=(4\pi M-H)H$. Depending on the relationship between M and H, the maximum energy product can exhibit different behavior. M is approximately constant when $H<H_d$, the coercive field. If M is constant, the maximum of P occurs when $H=H_0=2\pi M_s$, where M_s is the saturation magnetization. Thus the maximum energy product is $P_2=4\pi M_s^2$ when $H_d>2\pi M_s$. M is no longer constant when $H>H_d$. If $H_0>H_d$, the maximum energy product is $P_1=(4\pi M-H_d)H_d$. If $H_0\ll H_c$, the energy product can be increased by increasing M even if H_c is decreased. In Fig. 3 we show the maximum energy product of the composite discussed here at three temperatures ($T/V=0.58$, dashed line; $T/V=1.16$, solid line; $T/V=2.31$, dash-dotted line). For case (1) some of the results come from P_1 and some for P_2. In the present case, all the results come from P_1 because the switching field is much smaller. Our result suggests that case (1) have a better chance of providing a magnet with a high-energy product.

This work is supported in part by DARPA Contract No. F33615-01-2166.

[1] E. F. Kneller and R. Hawig, IEEE Trans. Magn. **27**, 3588 (1991).
[2] P. G. McCormick, W. F. Miao, P. A. I. Smith, J. Ding, and R. Street, J. Appl. Phys. **83**, 6256 (1998).
[3] Zhongmin Chen, Yong Zhang, Maria Daniil, Hideyuki Okumura, G. C. Hadjipanayis, and Qun Chen, in *Proceedings of the 16th International Workshop on Rare-Earth Magnets and their Applications,* edited by H. Kaneko, M. Homma, and M. Okada (Japan Institute of Metals, Tokyo, 2000), Vol. 1, p. 449.
[4] R. Skomski and J. M. D. Coey, Phys. Rev. B **48**, 15812 (1993); R. Skomski, J. Appl. Phys. **76**, 7059 (1994).
[5] See, for example, R. Fisher, T. Schrefl, H. Kronmuller, and J. Fidler, J. Magn. Magn. Mater. **153**, 35 (1996) and references therein.
[6] R. F. Sabiryanov and S. S. Jaswal, Phys. Rev. B **58**, 12071 (1998); J. Magn. Magn. Mater. **177**, 989 (1998).
[7] Yuqiang Ma and S. T. Chui, J. Appl. Phys. **88**, 1583 (2000).
[8] S. T. Chui and Y. Yu, Phys. Rev. B **63**, 140419(R) (2001).
[9] S. T. Chui and Yong-li Ma, J. Appl. Phys. **91**, 9315 (2002).
[10] S. T. Chui, J. Phys.: Condens. Matter **11**, 2719 (1999).
[11] S. T. Chui, J. Magn. Magn. Mater. **187**, 63 (1998).
[12] S. T. Chui, J. Magn. Magn. Mater. **217**, 120 (2000).
[13] S. T. Chui, in *Micromagnetism*, Vol. 338 of NATO Advanced Study Institute, Series E, edited by George C. Hadjipanayis (Kluwer, Boston, 1996).
[14] S. T. Chui and V. Ryzhov, Phys. Rev. Lett. **78**, 2224 (1997); J. Magn. Magn. Mater. **177**, 1303 (1998).
[15] S. T. Chui, Appl. Phys. Lett. **68**, 3641 (1996).
[16] S. T. Chui and D. C. Tian, J. Appl. Phys. **78**, 3965 (1995); S. T. Chui, *ibid.* **79**, 4951 (1995); Phys. Rev. B **55**, 3688 (1997); J. Magn. Magn. Mater. **168**, 9 (1997).
[17] This length scale comes from consideration of the nucleus formation. See, for example, S. T. Chui, J. Magn. Magn. Mater. **168**, 9 (1997) —in particular, p. 13.

OVERVIEW OF THE HIGH-TEMPERATURE 2:17 MAGNETS

G. C. HADJIPANAYIS* AND A. M. GABAY
Department of Physics and Astronomy, University of Delaware, Newark, Delaware, 19716, U.S.A.
*Corresponding author e-mail: hadji@udel.edu

Abstract

Recent works on the bulk-hardened and nanocrystalline 2:17 magnets are reviewed. New experimental findings regarding the structure evolution, high-temperature magnetic behaviour and coercivity mechanism, as well as progress in improvement the room-temperature performance of the magnets are discussed.

Introduction

Known for three decades, the "2:17" magnets [1,2] (named for their major phase, Sm_2Co_{17}) are still materials of a great commercial importance, especially for high-temperature applications. Research efforts during the 90s [3-5] pushed the maximum operating temperature of the 2:17 magnets to above 400 °C. This became possible due to the unusual feature of certain 2:17 magnets - the positive temperature coefficient of their coercivity. Correspondingly, the earlier coercivity models had to be updated to explain these phenomena.

In general, the Sm-Co-Fe-Cu-Zr magnets (cast or sintered) require a solution heat treatment at 1150 - 1175 °C followed by an isothermal aging in the temperature range of 800 - 850 °C followed by slow cooling to 350 - 400 °C. The aging forms a sub-micron size microstructure consisting of the 2:17 cells (the Th_2Zn_{17}-type rhombohedral structure) surrounded by 1:5 layers (the $CaCu_5$ hexagonal structure) and intersected by the Zr-rich lamellas (whose structure is disputable). The slow cooling is accompanied by element exchange between the phases, notably by diffusion of Cu into the 1:5 cell boundaries. A noticeable coercivity appears only at this stage. This traditional model has been recently challenged by Goll *et al.* [6] suggesting that the $CaCu_5$-type structure of the cell boundaries forms only at the cooling stage.

The predominant magnetic hardening model for these magnets is that their coercivity is caused by a large gradient of domain wall energy at the cell boundaries which leads to domain wall pinning. There is no, however, agreement on the origin of this gradient. To illustrate this point, Figure 1 shows schematically three very different profiles of the anisotropy constant/domain wall energy suggested in some very recent publications.

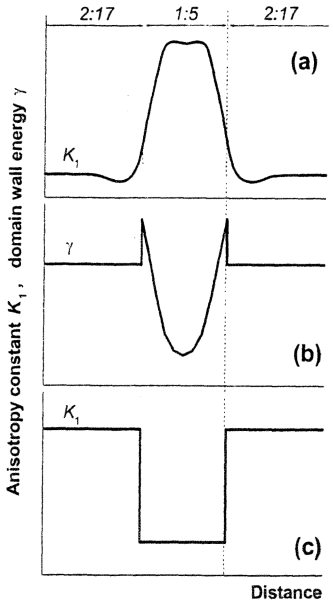

Figure 1 Profiles of the anisotropy constant K_1 or domain wall energy γ at the 1:5 cell-boundary phase as (a) estimated by Goll [7], Xiong *et al.* [8], (b) propsed by Yan et al. [9], and (c) assumed by Liu *et al.* [11], Rong *et al.* [12].

The K_1 profile shown in Figure1a and resulted from microchemistry studies allows two interpretations with respect to domain wall pinning. According to Goll [7], the 1:5 layers act as

repulsive pinning sites at room temperature and as attractive pinning sites at elevated temperatures. On the other hand, according to Xiong *et al.* [8], domain walls might be trapped at the Cu-rich layers of the 2:17 phase adjacent to the cell boundaries. Another model aroused from the microchemistry studies by Yan *at al.* [9]: in this model, domain wall motion is blocked by the Cu-poor outer layers of the 1:5 phase (Figure 1b). It should be noted that the "grain-boundary" $Sm(Co,Cu)_5$ phase itself displays exceptional hard magnetic properties [10]. Still the models with the uniform 1:5 phase acting as attractive pinning site (Figure 1c) are frequently used for qualitative [11] and quantitative [12] simulations. Earlier we suggested [13] that in the magnets with a monotonic temperature dependence of coercivity the hardening is not due to pinning, but is nucleation-controlled.

In this paper, we review the most recent (and mostly experimental) works on the bulk-hardened 2:17 magnets with a special attention paid to the studies performed at the University of Delaware Magnetics Laboratory. It is not surprising that most of the latest studies were focused on the structure evolution and coercivity mechanism. The magnetic performance was also addressed in the attempts to improve the high-temperature coercivity of the Sm-Co-Fe-Cu-Zr magnets or raise their maximum energy product by partial Pr substitution for Sm. The review on the 2:17 magnets would be incomplete without mentioning the alloys whose coercivity originates not from the above two-phase cellular structure, but from very fine single phase grains. These nanocrystalline magnets made from an amorphous precursor or by controlled rapid solidification are also suitable for high-temperature applications.

1 Magnetic properties of bulk-hardened and nanocrystalline 2/17 magnets

1.1 High-temperature magnets

A number of recent studies were aimed to explore further the anomalous temperature dependence of coercivity. It is well known that this phenomenon is very sensitive to the alloy composition, in particular to the Fe content. Our recent work has showed that it may also be sensitive to the temperature of isothermal aging. Figure 2 shows the temperature dependencies of coercivity for the 2:17 magnets with three different Fe concentrations processed either at 800 or 850 °C. In all the cases, the lower aging temperature favours the high-temperature coercivity (at the larger Fe contents it favours the room-temperature coercivity as well).

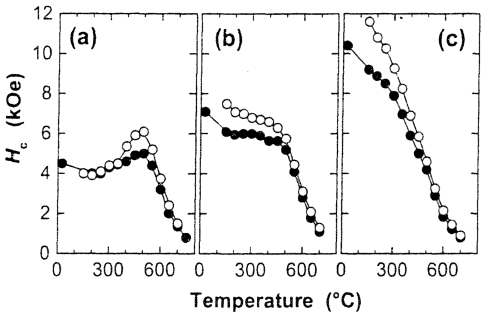

Figure 2 Coercivity *vs.* temperature for $Sm(Co_{0.9-x}Fe_xCu_{0.08}Zr_{0.02})_{7.5}$ magnets aged at 800 °C for 36 h (open circles) or at 850 °C for 12 h (closed circles): (a) $x = 0.1$, (b) $x = 0.15$, (c) $x = 0.2$.

We also observed magnetic hardening in the $Sm(Co_{0.86-y}Fe_{0.1}Ni_yZr_{0.04})_{8.5}$ alloys having Cu completely replaced by Ni. The cellular microstructure of the heat-treated Sm-Co-Fe-Ni-Zr magnets is very similar to that of the conventional Sm-Co-Fe-Cu-Zr ones (Figure 3). Nickel changes the Curie temperature, saturation magnetization and magnetocrystalline anisotropy of the 1:5 cell-boundary phase in a way similar to that of copper. It has, however, much greater low-temperature solubility in

the cell-interior 2:17 phase. We should not therefore expect significant Ni segregations at the cell boundaries after aging. The observed properties (Figure 4) - relatively low room temperature coercivity and its anomalous temperature dependence for certain Ni concentrations - suggest that the segregation of the non-magnetic Cu or Ni atoms at the cell boundaries is more important for the room-temperature coercivity and, apparently, less important for the coercivity at elevated temperatures.

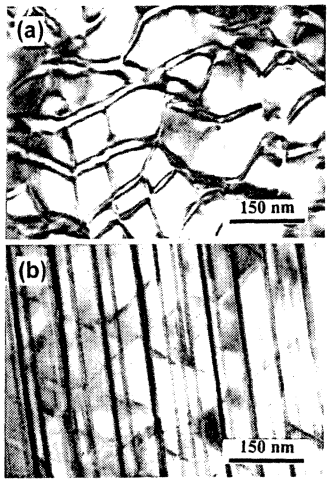

Figure 3 TEM images showing (a) cellular and (b) lamellar microstructures in heat-treated $Sm(Co_{0.68}Fe_{0.1}Ni_{0.18}Zr_{0.04})_{8.5}$.

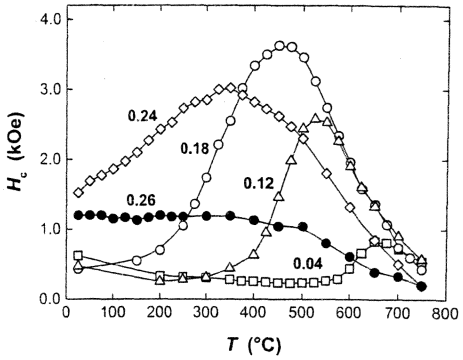

Figure 4 Coercivity *vs.* temperature for $Sm(Co_{0.86-x}Fe_{0.1}Ni_xZr_{0.04})_{8.5}$ magnet with different x.

Zhang *et al.* [14] also observed the anomalous temperature dependence of coercivity in bulk-hardened $PrCo_{6.7-x}Cu_xTi_{0.3}$ and reported its perfect correlation with the Curie temperature of the 1:5 phase. Thermomagnetic data suggest a significant effect of Ti on the properties of the cell-interior 2:17 phase. This is not the case for Zr (known to form a separate "lamellar" phase) and may explain the low room-temperature coercivity of the magnets with Ti. Unfortunately, because of the poor room-temperature properties neither bulk-hardened Pr-Co-Cu-Ti nor Sm-Co-Fe-Ni-Zr alloys can be considered for practical magnets.

Coercivity can also be developed in Sm_2Co_{17}-based alloys by inducing a nanocrystalline structure, either by annealing an amorphous precursor or directly by rapid solidification. Recently, Rhen *et al.* [15] reported preparing Sm-Co-Zr-Ti-B magnets by annealing a ball-milled amorphous precursor. The magnets showed coercivity of 5 kOe at 400 °C and their nanocrystalline structure of the disordered hexagonal 2:17 phase (also known as 1:7) appeared to be stable at this temperature. In our recent work [16], we attempted to induce texture by hot deformation of similarly prepared Sm-Co-Fe alloys. We found that the Cu and Ga additions significantly increase density achieved by hot pressing and improve deformability at elevated temperatures. However, the deformation did not induce the desired texture. The typical hysteresis loops and alloy microstructures are shown in Figures 5 and 6, respectively.

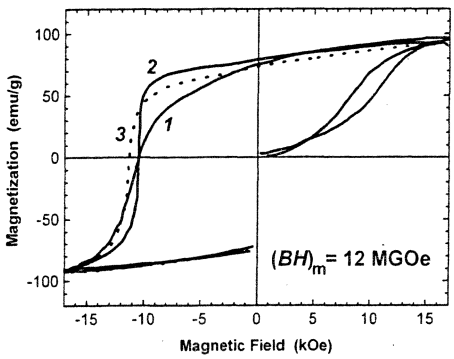

Figure 5 Hysteresis loops of nanocrystalline $Sm_{10.85}Co_{54.25}Fe_{21.6}Cu_{13.3}$: hot-pressed magnet (*1*), die-upset magnet parallel to pressure direction (*2*), die-upset magnet parallel to pressure direction (*3*).

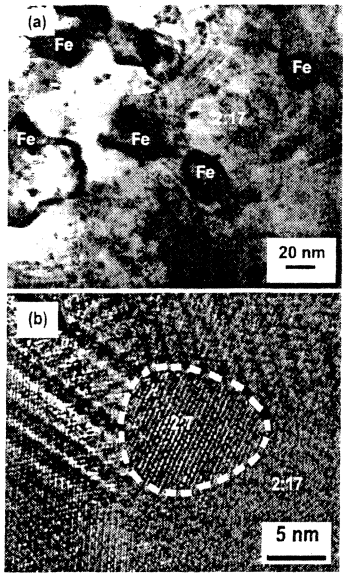

Figure 6 TEM (a) bright-field and (b) high-resolution images of hot-pressed $Sm_{11.9}Co_{59.5}Fe_{23.6}Cu_5$ magnet.

1.2 Magnets with high energy product

So far, the most effective way of increasing the energy product in the bulk-hardened Sm-Co-Fe-Cu-Zr magnets proved to be an increase of the Fe content. Magnets with 25 - 28 at.% Fe show a $(BH)_m$ of 33 - 34 MGOe with a coercivity H_c of 13 - 18 kOe [17-19]. Partial replacement of Sm by other light rare-earths with larger atomic magnetic moments, though potentially promising, appeared to be less successful. The energy product of 36 MGOe reportedly measured on a quasi-single crystal with 41% Sm replaced by Pr [20], has never been reproduced in sintered magnets [21]. For the latter, 30 MGOe with H_c of 15.5 kOe were the best reported properties achieved via combined Pr-Nd-Ce substitution for Sm [22].

Working with cast magnets we have succeeded in achieving very high values of $(BH)_m$ (at reasonably high H_c) by partial Pr substitution for Sm. The as-cast ingots were subjected to a solution treatment at 1100 - 1175 °C followed by water quenching. Isothermal aging was performed at 785 - 850 °C and followed by slow cooling to 350 °C at a rate of 0.7 °C/min. The magnetic properties were measured for magnetically oriented coarse powders magnetized by a dc field of 50 kOe with an appropriate correction for the self-demagnetizing field.

It is known from the earlier studies [21] that Pr substitution makes the 2:17 magnets more sensitive to the solution treatment temperature. Figure 7 shows the $(BH)_m$ of fully heat-treated magnets with different Pr substitutions plotted as a function of the solution treatment temperature. When Pr is added, the effect of this temperature becomes much stronger for the same aging conditions; the optimum solution temperature decreases with increasing Pr content. It is interesting, however, that even after solution treatment at a "wrong" temperature, relatively high $(BH)_m$ values can be achieved after a very prolonged aging (Figure 8). SEM reveals that both samples with relatively large Pr content shown in Figure 8 are not perfectly homogeneous after the solution treatment. Sample 1, which was processed at 1150 °C, contained fewer precipitates rich in Pr and Cu, while sample 2, which was held at 1125 °C, contained extended areas which are slightly enriched in Pr and Cu. Therefore, the longer aging time for sample 1 is required because of the longer average distance that the atoms of the more segregated elements (like Cu) must travel until they reach their position in the newly formed cellular structure.

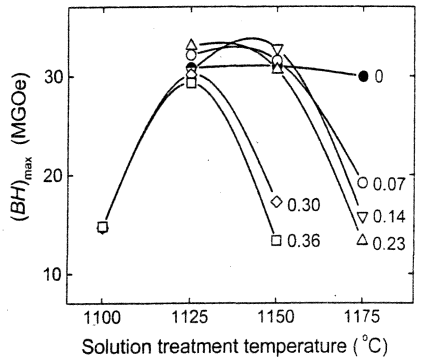

Figure 7 Effect of solution treatment temperature on the maximum energy product of $(Sm_{1-w}Pr_w)_{11}(Co_{0.72}Fe_{0.28})_{82}Cu_{5.5}Zr_{1.5}$ alloy after aging at 800 °C for 24 h and slow cooling.

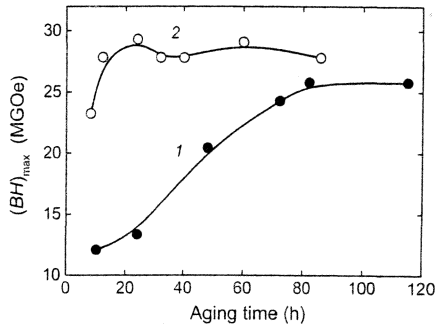

Figure 8 Maximum energy product *vs.* aging time for $(Sm_{0.64}Pr_{0.36})_{11}(Co_{0.72}Fe_{0.28})_{82}Cu_{5.5}Zr_{1.5}$ alloy solution-treated at 1150 °C (*1*) and 1125 °C (*2*).

We have found that in Pr-substituted alloys Zr tends to form phases with Co. Figure 9 shows SEM microstructures of as-solution-treated alloys with 2 at.% Zr and Pr substitution for Sm. The bright rare-earth-rich areas were found to be greatly enriched with Pr and Cu. It can be seen that these areas are not uniform; compositions determined by EDS varied from $(Sm,Pr,Zr)_2(Co,Fe,Cu)_7$ to binary PrCu. The dark, distinctly shaped precipitates were identified as $Zr_6(Co,Fe)_{23}$ and $Zr(Co,Fe)_2$. The formation and growth of the Zr-rich phases seem to be promoted by the (Pr,Cu)-rich phases. To avoid formation of the undesirable Zr-rich phases, the Zr content was limited to 1.5 at.%.

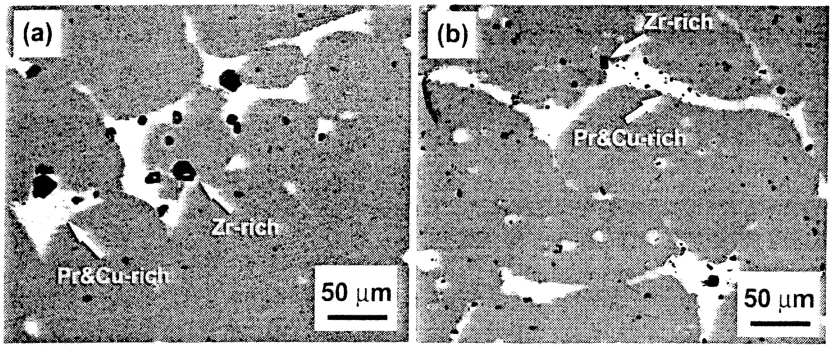

Figure 9 Backscattered SEM images of (a) $(Sm_{0.8}Pr_{0.2})_{11.5}(Co_{0.7}Fe_{0.3})_{80.5}Cu_6Zr_2$ and (b) $(Sm_{0.6}Pr_{0.4})_{11}(Co_{0.7}Fe_{0.3})_{82}Cu_5Zr_2$ alloys after solution treatment at 1150 °C.

Generally somewhat different heat treatments are needed to achieve the largest H_c and $(BH)_m$. Figure 10 summarizes the properties of the Pr-substituted magnets heat treated for the largest $(BH)_m$. Replacing 23 at.% Sm by Pr allowed us to increase $(BH)_m$ from 30 to 33 MGOe (up to 34 MGOe in selected samples) preserving the intrinsic coercivity of 17-19 kOe. TEM images of cellular structure in the magnets with zero, optimum and excessive Pr substitutions (Figure 11) reveal no significant differences. We must assume, therefore, that in the optimized magnets, the observed effect of Pr is merely associated with the change of phase properties. Even without a clear understanding of the coercivity mechanism, one can connect the rise of $(BH)_m$ and the corresponding decline of H_c with the beneficial effect of Pr on the saturation magnetizations of both the 2:17 and 1:5 phases and its detrimental effect on the magnetocrystalline anisotropies of these phases.

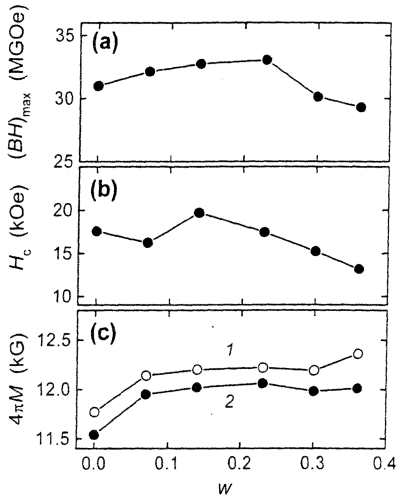

Figure 10 Effect of Pr substitution for Sm in $(Sm_{1-w}Pr_w)_{11}(Co_{0.72}Fe_{0.28})_{82}Cu_{5.5}Zr_{1.5}$ on (a) maximum energy product, (b) intrinsic coercivity and (c) magnetization at 15 kOe (*1*) and at the remanence (*2*).

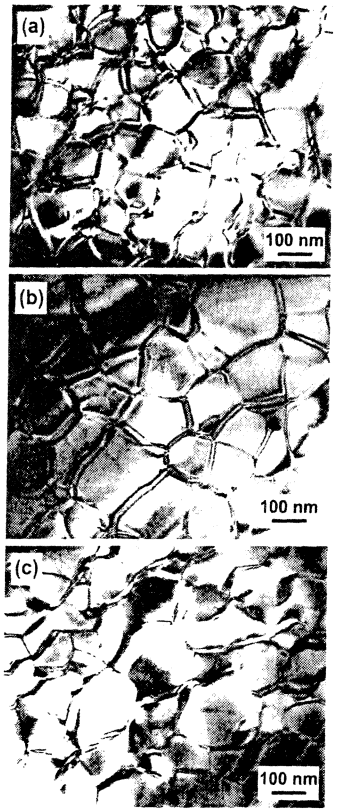

Figure 11 TEM images of optimally heat-treated $(Sm_{1-w}Pr_w)_{11}(Co_{0.72}Fe_{0.28})_{82}Cu_{5.5}Zr_{1.5}$ alloys with (a) $w = 0$, (b) $w = 0.23$, (c) $w = 0.36$.

2 Coercivity studies

2.1 High-temperature measurements

The high-temperature peak of coercivity can be observed in many R-Co-Cu based systems having the typical microstructure of 2:17 cells surrounded by 1:5 cell boundaries [3,4,13,14,23]. It is now more or less accepted that this phenomenon is caused by a loss of ferromagnetic ordering in the 1:5 phase, which makes the 2:17 cells magnetically insulated with their coercivity controlled by a magnetization rotation [3] or by nucleation of revered magnetic domains [13,14,24]. Recently we have studied the evolution of remanence behaviour for the $Sm(Co_{0.74}Fe_{0.1}Cu_{0.12}Zr_{0.04})_7$ magnet with the anomalous temperature behaviour of coercivity (see Figure 12a). The remanence behaviour was analyzed via the so-called δM plot:

$$\delta M(H) = M_r(H) - [1-2M_d(H)], \qquad (1)$$

where $M_r(H)$ and $M_d(H)$ are the remanent magnetizations after magnetizing with $+H$ field and demagnetizing with $-H$ field, respectively. In particulate media studies, the non-zero δM values are associated with positive or negative interactions between the particles. When studying continuous

granular ferromagnets, $\delta M > 0$ is usually thought to indicate the predominant exchange interaction between the grains, while $\delta M < 0$ - the predominant magnetostatic (dipole) interaction. Figure 12b shows that heating the sample above the certain critical temperature results in the transition from $\delta M > 0$ to $\delta M < 0$. One can suggest that the critical temperature is the Curie temperature of the 1:5 phase; $\delta M > 0$ represents a continuous ferromagnet with exchange coupled 2:17 and 1:5 phases, while $\delta M < 0$ represents insulated 2:17 cells interacting only magnetostatically. In many bulk-hardened 2:17 magnets, the 1:5 cell-boundary layers are only 4-5 nm thick, but recent calculations by Skomski *et al.* [25] confirm that a paramagnetic layer only a few interatomic distances thick can provide a nearly complete exchange decoupling. If our analysis is correct, at room temperature, the bulk-hardened 2:17 magnets are a type of anisotropic nanocomposites with both the constituent phases magnetically hard and all the easy magnetization directions parallel to each other. Due to the latter no remanence enhancement (which is typical for the isotropic exchange-coupled magnets) can be expected.

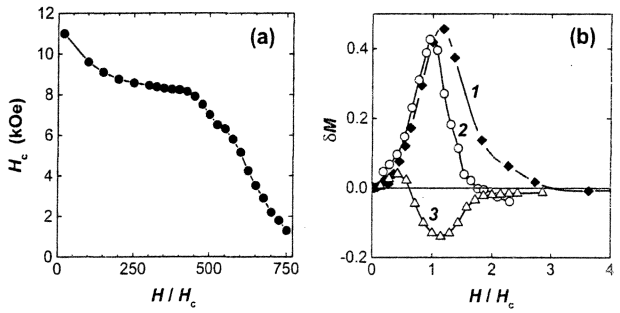

Figure 12 (a) Temperature dependence of coercivity and (b) δM plots at 25 (1), 250 (2) and 500 (3) °C for $Sm(Co_{0.74}Fe_{0.1}Cu_{0.12}Zr_{0.04})$- magnet.

Magnetic viscosity studies by Panagiotopoulos *et al.* [26] showed a drastic increase of the activation volume above the Curie temperature of the 1:5 phase. This was interpreted by the authors as an indication of a transition from a pinning-type hardening at low temperatures to a nucleation-type at high temperatures

2.2 Structure evolution during heat treatment

In the case of "precipitation-hardened" 2:17 magnets, the nearly similar compositions of the magnets and the cell-interior phase sometimes leads to the mistaken opinion that the precipitating phase is the cell-boundary phase. In fact, however, it is the rhombohedral cell-interior phase (2:17R) which precipitates from the off-stoichiometric 1:5 solid solution leaving the remaining matrix phase to form cell boundaries with the "more stoichiometric" 1:5 composition. Therefore, the entire microstructure evolution in the 2:17 magnets is driven by the hexagonal → rhombohedral ordering transformation.

In an attempt to examine the structure evolution in a typical 2:17 magnet by Mössbauer spectroscopy, we replaced part of the Fe in the cast $Sm_{10.75}(Co_{0.7}Fe_{0.3})_{82}Cu_{5.5}Zr_{1.75}$ magnet by the Fe^{57} isotope. Samples of the magnet were studied at three different stages of the heat treatment and the results are shown in Table 1. The Mössbauer data suggest that about half of the Fe atoms are still present in the hexagonal cell-boundary phase by the end of isothermal aging.

Since the solution-treated alloys possess the off-stoichiometric 1:5 structure, we can start from the pure $SmCo_5$ phase and name three factors needed to obtain the 2:17-type magnet. The first factor, of course, is the deviation from the 1:5 stoichiometry (*i.e.* Sm content less than 16.7 at.%). The second factor is the presence of Cu and the third one is the presence of Zr. The latter effectively suppresses the formation of the rhombohedral 2:17 phase in solution-treated samples and makes it possible to achieve a disordered hexagonal structure with significant deviations from the 1:5 stoichiometry [27].

The presence of Fe in the 2:17 magnets is favorable, but not necessary for the magnetic hardening. In order to better understand the structure evolution in the bulk-hardened 2:17 alloys, we studied the individual and combined effects of the above three factors. The off-stoichiometric $Sm_{15.5}Co_{84.5}$ alloy and a number of its derivatives with Zr substitution for Sm and Cu substitution for Co (*e.g.*, $Sm_{12}Zr_{3.5}Co_{84.5}$, $Sm_{15.5}Co_{72.5}Cu_{12}$ and $Sm_{12}Zr_{3.5}Co_{72.5}Cu_{12}$) were solution treated at 1050 - 1150 °C, aged at 850 °C and slowly cooled to 350 °C. During this heat treatment we monitored changes in the structure, thermomagnetic and hard magnetic properties of the samples. Before aging all the alloys had a single-phase hexagonal 1:5 structure and a single Curie temperature. Aging at 850 °C led to the formation of the second phase, 2:17R, and changed the properties of the original 1:5 phase. These changes are shown in Figure 13.

Table 1 Coercivity, Mössbauer parameters and estimated percentage of Fe atoms in the hexagonal and rhombohedral 2:17 phases for the $Sm_{10.75}(Co_{0.7}Fe_{0.3})_{82}Cu_{5.5}Zr_{1.75}$ alloy at different stages of heat treatment.

Alloy state	H_c (kOe)	Parameters	Atomic sites					Fe atoms in	
			6*c*1	6*c*2	9*d*	18*h*	18*f*	2:17H	2:17R
Solution-treated at 1175 °C	0.3	δ (mm/s)	0.1	0.14	-0.06	-0.07	-0.05	> 90%	-
		H_{eff} (kOe)	329	345	283	270	270		
		ΔE_q (mm/s)	0.08	0.04	-0.66	-0.75	0.23		
		ΔH (kG)	3	1	5	11	16		
		%	11	7	21	18	43		
Aged at 800 °C	0.7	δ (mm/s)	0.08	0.09	-0.07	-0.06	-0.05	50%	50%
		H_{eff} (kOe)	336	337	290	276	273		
		ΔE_q (mm/s)	0.04	0.06	-0.64	-0.07	0.26		
		ΔH (kG)	6	6	4	5	17		
		%	11	11	18	17	42		
Slowly cooled from 800 °C	24.8	δ (mm/s)	0.08	0.15	-0.05	-0.04	-0.04	25%	75%
		H_{eff} (kOe)	334	348	294	280	276		
		ΔE_q (mm/s)	0.08	0.02	-0.66	-0.68	0.26		
		ΔH (kG)	4	2	5	4	16		
		%	13	9	19	18	41		

In the binary $Sm_{15.5}Co_{84.5}$ alloy, the properties of the 1:5 phase rapidly approach those of the stoichiometric $SmCo_5$: phase separation occurs via a nucleation and growth of the incoherent 2:17R precipitates [28] and no cellular structure forms. In Zr(Cu)-substituted alloys, the phase separation occurs via coherent 2:17R precipitates [28]; the lattice parameters and Curie temperature change gradually and TEM reveals the cellular 2:17 / 1:5 microstructure. Unexpectedly, the T_C of the alloys substituted with both Zr and Cu was found to rise during isothermal aging (see $Sm_{12}Zr_{3.5}Co_{72.5}Cu_{12}$ in Figure 13). This must reflect more complex compositional changes than just an increase in the Sm content as approaching the 1:5 stoichiometry.

The cellular microstructure is not the only condition for developing the high coercivity. Only alloys containing a sufficient amount of Cu show magnetic hardening during the slow cooling (Figure 14). Alloys with different amount of Cu - $Sm_{12}Zr_{3.5}Co_{72.5}Cu_9$ and $Sm_{12}Zr_{3.5}Co_{72.5}Cu_{12}$ - show very different coercivities (5 and 12.5 kOe, respectively) after the slow cooling, despite very similar microstructure (Figure 15). As the $Sm_{12}Zr_{3.5}Co_{72.5}Cu_{12}$ alloy is slowly cooled, the T_C of the 1:5 phase present in the alloy decreases significantly. At the first sight, this is consistent with the model which connects the magnetic hardening with the redistribution of Cu between the 2:17 and 1:5 phases. More detailed analysis, however, reveals certain discrepancies. First, we observe no changes in the Curie temperature of the 2:17 phase. Those changes must occur as the phase looses Cu, but possibly they are simply too small to notice. Second, the increase of coercivity mostly occurs not when the T_C of the 1:5 phase decreases, but after it "stabilizes". In order to illustrate the latter point, Figure 16 shows the $M(H)$ and $M(T)$ curves of the $Sm_{12}Zr_{3.5}Co_{72.5}Cu_{12}$ alloy after partial and complete slow

cooling. One can see that a significant change in the alloy coercivity is *not* accompanied by any noticeable changes in the Curie temperatures. It is, therefore, possible that the high coercivity develops in the alloy as a result of a low-temperature aging *after* the cooling-induced compositional changes. These results suggest that a full understanding of magnetic hardening in 2:17 magnets requires more careful attention to the magnetic hardening behaviour of $Sm(Co,Cu)_5$ cell-boundary phase.

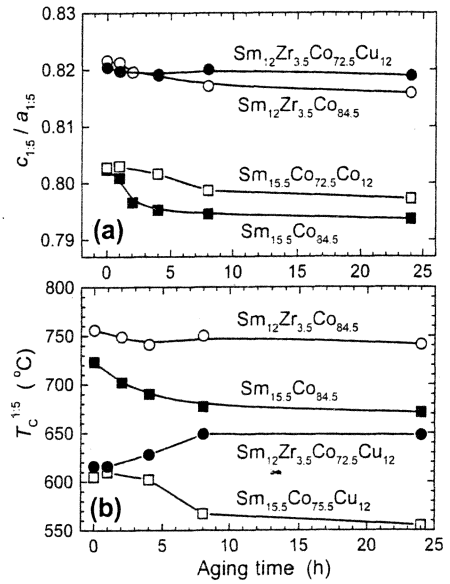

Figure 13 Effect of aging at 850 °C on (a) *c*/*a* ratio and (b) Curie temperature of the 1:5-type phase in the alloys whose compositions were derived from $Sm_{15.5}Co_{84.5}$ by Zr substitution for Sm and or Cu substitution for Co.

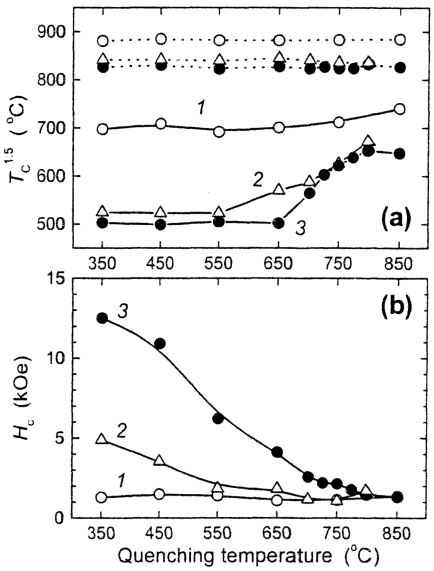

Figure 14 Values of (a) Curie temperature and (b) coercivity of $Sm_{12}Zr_{3.5}Co_{84.5}$ (*1*), $Sm_{12}Zr_{3.5}Co_{72.5}Cu_9$ (2) and $Sm_{12}Zr_{3.5}Co_{72.5}Cu_{12}$ (*3*) alloys quenched from different temperatures during the slow cooling after being aged at 850 °C for 24 h. T_Cs of the 2:17 phases are shown with dotted lines.

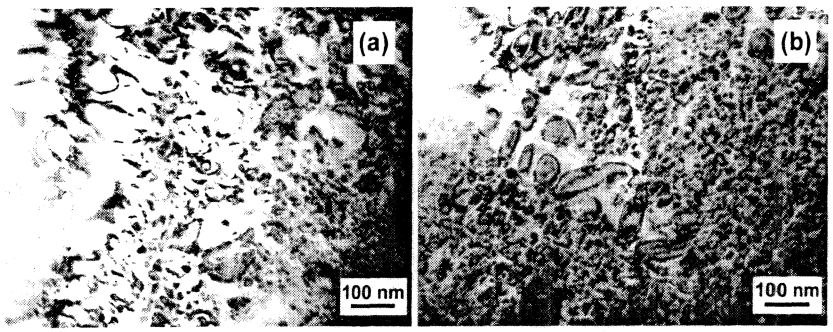

Figure 15 TEM images of the cellular 2:17/1:5 microstructure in fully heat-treated (a) $Sm_{12}Zr_{3.5}Co_{75.5}Cu_9$ and (b) $Sm_{12}Zr_{3.5}Co_{72.5}Cu_{12}$.

Unfortunately, it is not easy to estimate to which extent the $M(T)$ experiment itself modifies the microstructure and/or the microchemistry of the alloys, *i.e.* to which extent the data in Figure 16b

correspond to those in Figure 16a. A simple remeasurement of the room-temperature $M(H)$ curves is not a solution, because cooling in the $M(T)$ experiment is relatively slow. Nevertheless even after that cooling the samples *1* and *2* from Figure 16b still show a significant difference in the room-temperature coercivity.

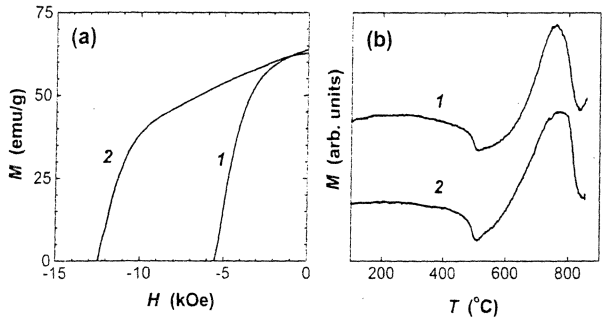

Figure 16 (a) Room-temperature demagnetization curves and (b) heating $M(T)$ curves at 1 kOe for $Sm_{12}Zr_{3.5}Co_{72.5}Cu_{12}$ samples aged at 850 °C for 24 h and slowly cooled to 550 (1) and 350 (2) °C.

It is very important that in our study, the 1:5 phase has been traced by its lattice and thermomagnetic characteristics throughout the whole heat treatment - from the solution state to the state with high coercivity. These results strongly suggest that the 1:5 phase does not appear during the slow cooling as suggested in [6,8].

In the work by Xiong *et al.* [8], the structure evolution in the $Sm(Co_{0.72}Fe_{0.2}Cu_{0.055}Zr_{0.025})_{7.5}$ magnet has been studied with a three-dimensional atom probe. The results also support the traditional view that the cell boundary phase has the 1:5 structure not *after*, but *before* the slow cooling. The study confirms our earlier finding [29] that the triple junctions of the 1:5 cell-boundary phase are almost twice richer in Cu than the narrow regions of this phase. In addition to diffusion of Cu into the cell-boundaries at the slow-cooling stage, the authors observed a diffusion of Zr and Sm respectively into and out of the lamellar phase. By the end of the slow cooling, the latter is nearly Sm-free $Zr(Co,Fe)_3$ with the Be_3Nb structure.

2.3 Coercivity mechanisms

While there seems to be a general agreement on the coercivity mechanism of the 2:17 magnets above the Curie temperature of the grain-boundary phase (nucleation), the room-temperature magnetization reversal remains disputable.

The repulsive pinning model (Figure 1a), in which $\gamma_{1:5} > \gamma_{2:17}$ (γ is the domain wall energy for the corresponding phase) is based on the studies of microchemistry of the heat-treated magnets [7,30]. It cannot, however, explain why the coercivity appears (or greatly increases) during the slow cooling, when the diffusion of Cu from 2:17 into 1:5 leads to an increase in $\gamma_{2:17}$ and decrease in $\gamma_{1:5}$. The suggestion that the 1:5 phase itself forms only at the slow-cooling stage [7], as we just showed, disagrees with a number of experimental results. In attempt to resolve this inconsistency, Xiong *et al.* [8] suggested that domain walls are attracted by the Cu-rich layers of the 2:17 phase (the K_1 minima in Figure 1a). In our opinion, however, the experimental results they presented do not show significant changes of the Cu content in those layers upon the slow cooling.

The simplest attractive pinning model (Figure 1c) with $\gamma_{1:5} < \gamma_{2:17}$ is consistent with the Cu diffusion, but not consistent with the latest microchemical studies [7,30]. The model proposed by Yan et al [9] (Figure 1b; repulsive pinning at the Cu-poor outer layers of the 1:5 phase) is based on the microchemical data which are highly different from those reported in [7,30] and have to be confirmed. Finally, our earlier model [13], which relates the room temperature coercivity to either

nucleation or attractive pinning (depending on the amount of Cu in the cell boundaries after a full heat treament), is also lacking solid microchemical evidences.

Recently there has been a trend [8,9,13,29] to pay more attention to the internal structure of the $Sm(Co,Cu)_5$ cell-boundary phase - the phase related to the whole history of the bulk-hardened magnets [10]. It is quite possible that this history will eventually make a full circle explaining the coercivity of the 2:17 magnet via the understanding of the coercivity of bulk $Sm(Co,Cu)_5$ magnets.

Acknowledgements

The authors would like to thank Drs. V. Papaefthymiou, W. Tang and Y. Zhang for their contributions. This work was supported by DARPA.

References

[1] Y. Tawara and H. Senno, *Jpn., J. Appl. Phys.* **12** (1973) 761.

[2] T. Ojima, S. Tomizawa, T. Yoneyama and T. Hori, *IEEE Trans. Magn.* **13** (1977) 1317.

[3] A. G. Popov, A. V. Korolev and N. N. Shchegoleva, *Phys. Met. Metall.*, **69** (1990) 100.

[4] J. F. Liu, T. Chui, D. Dimitrov and G. C. Hadjipanayis, *Appl. Phys. Lett.* **73**, 3007 (1998).

[5] C. H. Chen, M. S. Walmer, M. H. Walmer, S. Liu, E. Kuhl, G. Simon, *J. Appl. Phys.* **83** (1998) 6706.

[6] D. Goll, W. Sigle, G. C. Hadjipanayis and H. Kronmüller, *Mat. Res. Soc. Symp. Proc.* **674** (2001) U.2.4.

[7] D. Goll, *Z. Metallkd.* **93** (2002) 1009.

[8] X. Y. Xiong, T. Ohkubo, T. Koyama, K. Ohashi, Y. Tawara and K. Hono, *Acta Mater.* **52** (2004) 737.

[9] A. Yan, O. Gutfleisch, T. Gemming and K.-H. Müller, *Appl. Phys. Lett.* **83** (2003) 2208.

[10] E. A. Nesbitt, R. H. Willens, R. C. Sherwood, E. Buehler and J. H. Wernick, *Appl. Phys. Lett.* **12** (1968) 361.

[11] S. Liu, G. Doyle, E. Kuhl, C. Chen, M. S. Walmer and Y. Liu, *IEEE Trans. Magn.* **37** (2001) 2521.

[12] C. B. Rong, H. W. Zhang, J. Zhang, X. B. Du, S. Y. Zhang and B. G. Shen, *J. Appl. Phys.* **95** (2004) 1351.

[13] A. M. Gabay, W. Tang, Y. Zhang and G. C. Hadjipanayis, *Appl. Phys. Lett.* **78** (2001) 1595.

[14] J. Zhang, H.Liu, C. B. Rong, H. W. Zhang, S. Y. Zhang, B. G. Shen, Y. Q. Bai and B. H. Li, *Appl. Phys. Lett.* **83** (2003) 1172.

[15] F. M. F. Rhen, M Venkatesan, I. R. Harris and J. M. D. Coey, *J. Appl. Phys.* **93** (2003) 8683.

[16] Q. Zeng, A. M. Gabay, Y. Zhang and G. C. Hadjipanayis, *IEEE Trans. Magn.* (2004) in press.

[17] R. K. Mishra, G. Thomas, T. Yoneyama, A. Fukuno and T. Ojima, *J. Appl. Phys.* **52** (1981) 2517.

[18] S. Liu and A.E. Ray. *IEEE Trans. Magn.* **25** (1989) 3785.

[19] B. M. Ma, Y. L. Liang, J. Patel, D. Scott and C. O. Bounds, *IEEE Trans. Magn.* **32** (1996) 4377.

[20] G. V. Ivanova, A. G. Popov, L. M. Magat, V. G. Maykov, T. Z. Puzanova, Y. S. Shur and N.V. Nikolayeva. *Phys. Met. Metall.*, **59** (1985) 64.

[21] M. Q. Huang, Y. Zheng and W. E. Wallace, *J. Appl. Phys.* **75** (1994) 6280.

[22] S. Liu, A. E. Ray and H. F. Mildrum, *IEEE Trans. Magn.* **26** (1990) 1382.

[23] D. Goll, I. Kleinschroth, W. Sigle and H. Kronmüller, *Appl. Phys. Lett.* **76**, (2000) 1054.

[24] H. Kronmüller and D. Goll, *Physica B* **319** (2002) 122.

[25] R. Scomski, A. Kashyap, Y. Qiang and D. J. Sellmyer, *J. Appl. Phys.* **93** (2003) 6477.

[26] I. Panagiotopoulos, M. Gjoka and D. Niarchos, *J. Appl. Phys.* **92** (2002) 7693.

Fully Dense Bulk Nanocomposites of $(Sm_{1-x}Gd_x)_2(Co_{1-y}Fe_y)_{17}$+(Co, Fe) With High Coercivity and High Curie Temperature

Christina H. Chen, Don Lee, Sam Liu, Michael H. Walmer, Yong Zhang, and George C. Hadjipanayis

***Abstract*—Fully dense nanocomposites of $(Sm_{1-x}Gd_x)_2(Co_{1-y}Fe_y)_{2:17}$ phase + Co/Fe were obtained by hot pressing the amorphous powders at 740 °–760 °C. Amorphous powders were made by mechanical alloying. Up to 14 kOe of Coercivity was obtained for these Cu and Zr free nanocomposites. X-ray diffraction patterns confirm the status of amorphous powder and crystallized structure after annealing at 750–825 °C. Transmission electron microscopy image shows that the sizes of crystals were in the range of several nm to 100 nm. These fully dense nanocomposites have Curie temperatures higher than 900 °C and lower temperature coefficient of magnetization, which would make them ideal candidates for temperature compensated permanent magnets.**

***Index Terms*—Curie temperature, full density, nanocomposites magnets, Sm–Co rare earth magnets, temperature coefficient.**

I. Introduction

THE Sm_2Co_{17}-based magnets were an outgrowth of the investigation of $R_2(Co, Fe)_{17}$ alloys in 1972 [1]. A technique was developed in 1975–1977 [2]–[4] for manufacturing sintered 2:17 type magnets, which included adding Cu and Zr for purposes of magnetic precipitation hardening through a complicated heat treatment to achieve high coercivity.During the precipitation, a unique cellular and lamellar microstructure with 2:17 cells, 1:5 cell boundaries, and Zr rich lamellar were formed [5]–[7]. This technique has been used for the commercial production of 2:17 type magnets since then [8]–[11].

It is anticipated that different methods can be established to make $Sm_2(Co, Fe)_{17}$ magnets with $(BH)_{max}$ of 40 MGOe and acceptable Hci, while eliminating the addition of nonmagnetic elements, such as Cu and Zr [12]. High coercivity values for nanocomposite Sm_2Co_{17}/Co powder made by using mechanical alloying have been reported since 1996 [13], [14].

It is well known that the substitution of heavy rare earth metals for Sm results in temperature compensated (TC) magnets for special applications. TC magnets have smaller temperature coefficient of magnetization and lower magnetization compared to the normal Sm–Co 2:17 magnets, since the magnetic moment of heavy rare earth metal (such as Gd, Tb, Dy, Ho, and Er) couples antiparallel to the moment of transition metals (referring as the ferrimagnetic coupling). TC magnets with near "zero" temperature coefficient of Br have been producing since 1974, and it is our desire to develop better performance TC magnets with higher energy product for special applications.

The work reported here is one of our efforts to make 2:17 type magnets with high coercivity without additions of Cu, Zr, or other nonmagnetic elements.

Manuscript received October 16, 2003. This work was supported by DARPA-ONR under Contract N00014-03-01-0636 and DARPA-AFRL under Contract F33615-01-2-2166.

C. H. Chen, D. Lee, and S. Liu are with the University of Dayton, Dayton, OH 45469-0170 USA (e-mail: christina.chen@udri.udayton.edu).

M. H. Walmer is with Electron Energy Corporation, Landisville, PA 17538 USA (e-mail: mhw@electronenergy.com).

Y. Zhang and G. C. Hadjipanayis are with the Department of Physics and Astronomy, University of Delaware, Newark, DE 19716 USA (e-mail: yzhang@physics.udel.edu).

Digital Object Identifier 10.1109/TMAG.2004.830398

II. Experimental Method

$SmCo_5$, $GdCo_5$, $SmCo_{13}$, and $Sm(Co_{.5}Fe_{.5})_{13}$ alloys were mixed in certain ratios and milled with SPEX 8000 mixer/mill. $(Sm_{1-x}Gd_x)$ $(Co_{1-y}Fe_y)_z$ amorphous powders were formed after milling for 8–16 h. Some powders were annealed at 775–825 °C, and some were hot pressed at 740–760 °C for 1–2 min. Hot pressed magnets weighed 10–12 g for each. Some hot pressed samples were then hot deformed at 950 to 1000°C with 60% deformation in order to achieve crystal orientation. KJS Hysteresigraph was used for magnetic characterization at temperatures $\leq$300 °C, and the Lakeshore Vibrating Sample Magnetometer (VSM) was used for determining temperature coefficients of magnetization 4 πM and Curie temperatures at temperature up to 930 °C.

X-ray diffraction (XRD) was used to analyze the powders as milled and as annealed. Transmission electron microscopy (TEM) was used to observe microstructures of hot pressed sample.

III. Results and Discussions

Fully dense nanocomposite magnets with density of 8.35–8.70 g/cm^3 were obtained by hot pressing at 740–760 °C for 1–2 min. Coercivity Hci up to 14 kOe was obtained. This marks the first time that the fully dense Sm–Co/Fe nanocomposite with high coercivity is reported. Fig. 1 shows the curves of magnetization (4 πM) versus magnetic field (H) for as-milled powder and as-hot-pressed nanocomposite of $SmCo_{9.4}$. The coercivity Hci was 2.6 kOe for the as-milled powder, and 13.9 kOe for hot pressed nanocomposite. Fig. 2 displays the XRD patterns for the powders as milled and as

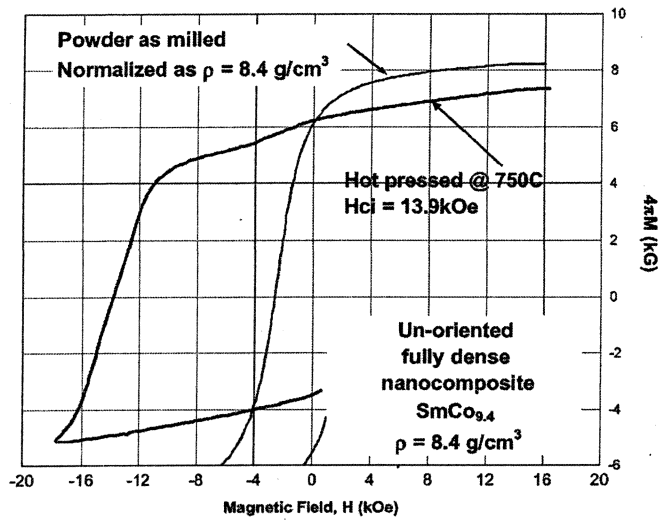

Fig. 1. Magnetization 4 πM versus magnetic field H.

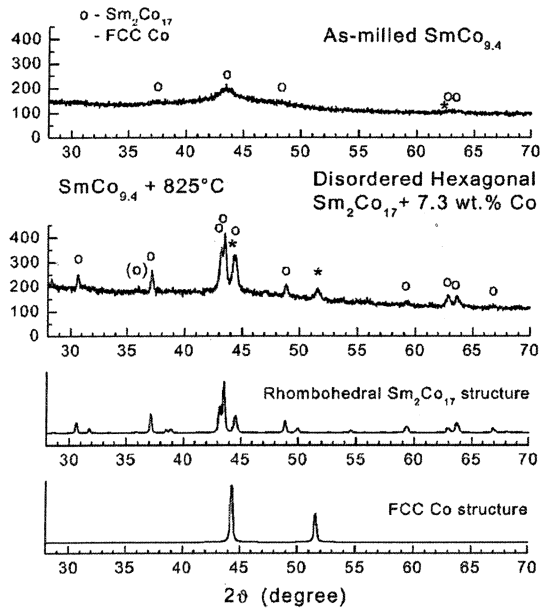

Fig. 2. XDR patterns of $SmCo_{9.4}$ powders: (Top) Mostly amorphous for as-milled. (Middle) Crystalline 2:17 + Co for annealed. (Bottom) Reference patterns of rhombohedral Sm_2Co_{17} and FCC Co.

annealed. The XRD patterns for Co FCC phase and Sm–Co 2:17 phase are also shown in Fig. 2 as references. The XRD patterns indicated that the as-milled powder was mostly in amorphous condition, and the annealed powder had the 2:17 phase and a Co phase. Fig. 3 is the TEM image for the hot pressed specimen, which shows that the sizes of crystals were in the range of several nm to about 100 nm.

Fig. 4 shows the curves of 4 πM versus H for the hot pressed nanocomposites of $Sm_{.84}Gd_{.16}Co_{8.95}$ and $Sm_{.17}Gd_{.83}Co_{8.95}$. The two curves shown in the figure had Hci = 10.25 and 6.2 kOe, respectively.Since these magnets were isotropic or unoriented, the values of saturation 4 πM are relatively low, with 7.5 and 6.9 kG, respectively.

As Fig. 5 shows, these nanocomposite magnets have two distinct T_c points, with $T_{c1} \cong 900\,^{\circ}C$ and $T_{c2} > 930\,^{\circ}C$. Due to the temperature limitation of the VSM, the T_{c2} can be only

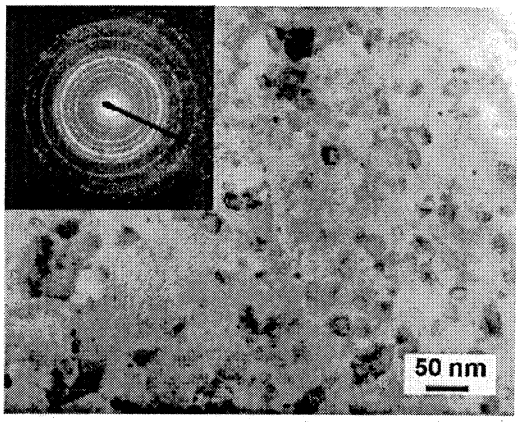

Fig. 3. TEM microstructure for the annealed powder.

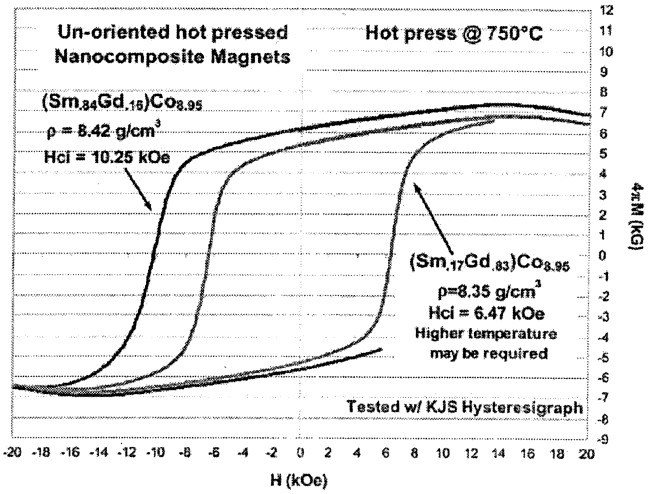

Fig. 4. 4 πM versus field H for the hot pressed nanocomposites.

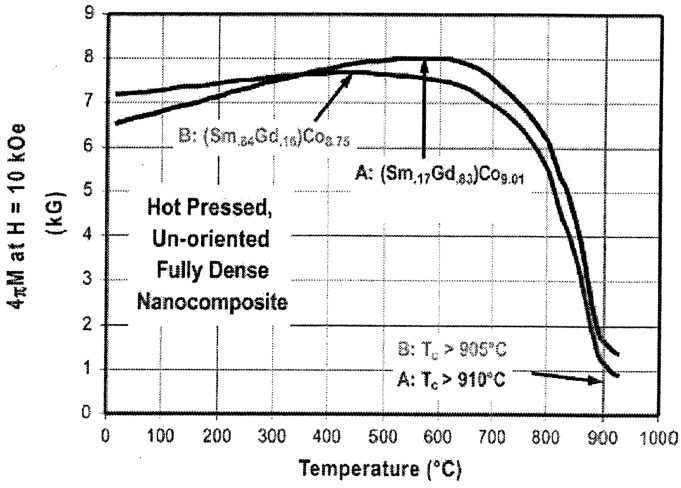

Fig. 5. Curie temperature measurement: $T_c > 900\,^{\circ}C$.

determined to be higher than 930 °C, since the 4 πM values are about 1 kG at 930 °C. Two T_c points show the presence of two distinct phases of 2:17 and cobalt.

These nanocomposite magnets also have lower temperature coefficient, α, of 4 πM, compared to that of the conventional 2:17 sintered magnets. Fig. 6 shows the comparison of the fully dense (Sm, Gd)-Co nanocomposite and the conventional

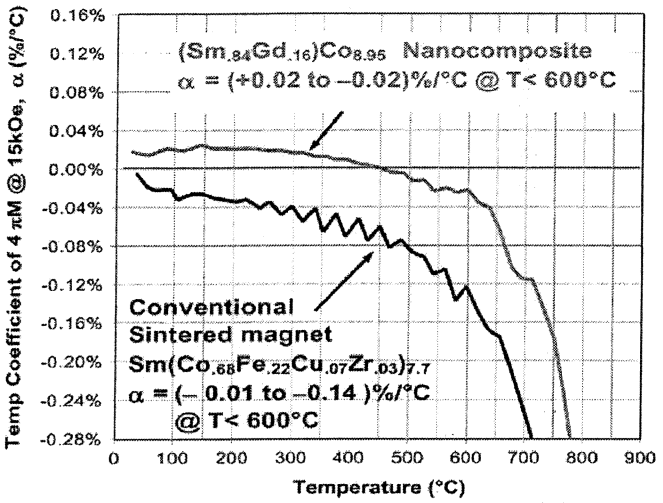

Fig. 6. Temperature coefficients of the 4 πM for the fully dense nanocomposite and conventional 2:17 magnet.

TABLE I
MAGNETIC PROPERTIES OF SOME NANOCOMPOSITE MAGNETS

	$4\pi M_{@15kOe}$ (kG)	Br (kG)	$_MH_I$ (kOe)	$(BH)_{max}$ (MGOe)
$(Sm_{.17}Gd_{.83})Co_{9.0}$	6.8	5.40	6.6	6.0
$(Sm_{.86}Gd_{.14})Co_{8.8}$	7.4	6.20	10.3	8.4
$Sm(Co_{.88}Fe_{.12})_{8.6}$	8.3	6.81	10.4	10.1
$Sm(Co_{.85}Fe_{.15})_{9.0}$	9.1	7.48	8.6	12.3
$Sm(Co_{.75}Fe_{.25})_{9.0}$	9.2	7.36	7.5	11.1
$SmCo_{9.4}$	8.7	7.70	13.8	9.1
$SmCo_{9.9}$ (O%>1.2%)	9.4	7.00	6.5	7.0

Sm–Co magnets. The high T_c and low temperature coefficient make these nanocomposites good candidates for high temperature applications.

Table I shows magnetic properties for some nanocomposite magnets of $(Sm_{1-x}\ Gd_x)_2(Co_{1-y}Fe_y)_z$. The range of x is 0 to 0.88, and the range of y is 0 to 0.25. The soft phase of Co/Fe should be 1% for z = 8.6, 5% for z = 9.0, and 12.8% for z = 9.9.

It was anticipated to form anisotropic nanocomposites with mechanical deformation, as previous paper reported for the nanocomposite magnets of Nd–Fe–B/Fe, Co [15]. However, our preliminary results for three samples with 60% deformation did not show any advantage of this technique. After 60% deformation, the coercivity was decreased due to grain growth, and the magnetization of the magnet was actually unchanged. It seems that the 2:17 hexagonal and/or rhombohedral crystals would not form texture as 2:14:1 tetragonal crystals would do when mechanical deformation occurs.

IV. CONCLUSION AND FURTHER WORK

In conclusion, fully dense nanocomposite magnets of $(Sm_{1-x}Gd_x)_2$ $(Co_{1-y}Fe_y)_{17}$+Co/Fe can be obtained by hot pressing the amorphous powder. These Cu and Zr free, fully dense nanocomposites have reasonable high coercivity with Hci = 6–14 kOe. These magnets also have Curie temperature higher than 900 °C, and small temperature coefficient of magnetization, which would make them ideal candidates for temperature compensated permanent magnets.

The further effort would include controlling oxygen content of amorphous powder, producing amorphous powder in large scale, and making anisotropic nanocomposite magnets with high energy.

ACKNOWLEDGMENT

The authors are grateful to Dr. V.M. Browning of DARPA and Dr. R.T. Fingers and Mr. E.M. Gregory of AFRL for their support.

REFERENCES

[1] A. E. Ray and K. J. Strnat, "Easy directions of magnetization in ternary," *IEEE Trans. Magn.*, vol. MAG-8, p. 516, 1972.
[2] A. J. Perry and A. Menth, "Permanent magnets based on Sm(Co, Cu, Fe)z," *IEEE Trans. Magn.*, vol. MAG-11, p. 1423, 1975.
[3] Y. Tawara and K. Strnat, "Rare earth cobalt permanent magnets near the 2:17 composition," *IEEE Trans. Magn.*, vol. MAG-12, p. 954, 1976.
[4] T. Ojima, S. Tomizawa, T. Yoneyama, and T. Hori, "Magnetic properties of a new type of rare earth magnets Sm2(Co,Cu,Fe,M)17," *IEEE Trans. Magn.*, vol. MAG-13, p. 1317, 1977.
[5] J. Fidler, P. Skalicky, and F. Rothwarf, "High resolution electron microscope study of Sm(Co,Fe,Cu,Zr) magnets," *IEEE Trans. Magn.*, vol. MAG-19, p. 2041, 1983.
[6] A. E. Ray, W. Soffa, J. Blachere, and B. Zhang, "Cellular microstructure development in Sm(Co,Fe,Cu,Zr)8.35 alloys," *IEEE Trans. Magn.*, vol. MAG-23, p. 2711, 1987.
[7] G. C. Hadjipanayis, W. Tang, Y. Zhang, S. T. Chui, J. F. Liu, C. Chen, and H. Kronmueller, "High temperature 2:17 magnets: relationship of magnetic properties to microstructure and processing," *IEEE Trans. Magn.*, vol. 36, p. 3382, Sept. 2000.
[8] A. E. Ray, "A revised model for the metallurgical behavior of 2:17 type permanent magnet alloys," *J. Appl. Phys.*, vol. 67, no. 9, p. 4972, 1990.
[9] B. M. Ma, Y. L. Liang, J. Patel, D. Scott, and C. O. Bounds, "The effect of Fe content on the temperature dependent magnetic properties of Sm(Co,Fe,Cu,Zr)z and SmCo5 sintered magnets at 450°C," *IEEE Trans. Magn.*, vol. 32, p. 4377, 1996.
[10] C. H. Chen, M. S. Walmer, M. H. Walmer, S. Liu, G. E. Kuhl, and G. Simon, "Sm2(Co,Fe,Cu,Zr)17 magnets for use at temperature 400°C," *J. Appl. Phys.*, vol. 83, p. 6706, 1998.
[11] M. S. Walmer, C. H. Chen, M. H. Walmer, S. Liu, and G. E. Kuhl, "A new class of Sm2TM17 magnets with operating temperature up to 550°C," *IEEE Trans. Magn.*, vol. 36, p. 3376, Sept. 2000.
[12] C. Chen, S. Kodat, M. H. Walmer, S.-F. Cheng, M. A. Willard, and V. G. Harris, "The effects of grain size and morphology on the coercivity of Sm2(Co1-xFex)17 based powders and spin cast ribbons," *J. Appl. Phys.*, vol. 93, no. 10, p. 7966, 2003.
[13] S. K. Chen, J. L. Tsai, and T. S. Chin, "Nanocomposite Sm2Co17/Co permanent magnets by mechanical alloying," *J. Appl. Phys.*, vol. 79, p. 5964, 1996.
[14] B. Z. Cui, M. Q. Huang, and S. Liu, "Magnetic properties of (Nd,Pr,Dy)2Fe14B/a-Fe nanocomposite magnets crystallized in a magnetic field," *IEEE Trans. Magn.*, vol. 39, p. 2866, Sept. 2003.
[15] D. Lee, J. S. Hilton, S. Liu, Y. Zhang, G. C. Hadjipanayis, and C. H. Chen, "Hot pressed and hot deformed nanocomposite (Nd,Pr,Dy)2Fe14B/a-Fe based magnets," *IEEE Trans. Magn.*, vol. 39, p. 2947, Sept. 2003.

Bulk Isotropic and Anisotropic Nanocomposite Rare-Earth Magnets

D. Lee, J. S. Hilton, C. H. Chen, M. Q. Huang, Y. Zhang, G. C. Hadjipanayis, and S. Liu

***Abstract*—Bulk, isotropic and anisotropic nanocomposite magnets of $(Nd,Pr,Dy)_xFe_{100-x-y-z-u-v}Co_yAl_zGa_uB_v$ with $x = 8$–11.6, $y = 6$–6.3, $z = 0$–0.2, $u = 0$–0.2, and $v = 5.6$–10.0 were prepared and their magnetic properties as functions of rare-earth content, hot press temperature, and hot-deformation amount were investigated. For isotropic nanocomposite magnets, the best $(BH)_{max}$ of 16.2 MGOe was obtained when hot pressing $Nd_{9.3}Pr_{0.5}Dy_{0.2}Fe_{77.7}Co_{6.3}Al_{0.2}Ga_{0.2}B_{5.6}$ at 660 °C. The magnetic performance of anisotropic nanocomposite magnets is strongly dependent on the rare-earth content and the hot deformation amount. The best $(BH)_{max}$ of 42 MGOe was achieved in a hot-deformed $Nd_{10.8}Pr_{0.6}Dy_{0.2}Fe_{76.1}Co_{6.3}Al_{0.2}Ga_{0.2}B_{5.6}$ magnet with 70% height reduction.**

***Index Terms*—Anisotropic, full density, hot deformation, hot press, nanocomposite magnets, rare-earth magnets.**

I. Introduction

THE $Nd_2Fe_{14}B$–α-Fe and $N_2Fe_{14}B$–Fe_3B nanocomposite magnet materials have been extensively studied since they were first reported by the Philips group the in late 1980s [1]–[6]. This new type of permanent magnet materials combines the high magnetocrystalline anisotropy of a magnetically hard phase, such as $Nd_2Fe_{14}B$, and the high saturation magnetization of a magnetically soft phase, such as α-Fe or Fe_3B, and possesses a potential for a very high energy product as predicted by many researchers [2]–[4].

In practice, however, technical difficulties were encountered in making bulk nanocomposite magnets with full density and anisotropic nanocomposite magnets. These difficulties remained for more than a decade until in early 2003 a rapid hot press and hot deformation were reported being used for successfully preparing bulk, anisotropic nanocomposite magnets [9]. This paper reports recent advances in making isotropic and anisotropic nanocomposite magnets.

Manuscript received October 16, 2003. This work was supported in part by the Defense Advanced Research Projects Agency-Air Force Research Laboratory (DARPA-AFRL) under Contract F33615-01-2-2166 and the U.S. Defense Advanced Research Projects Agency-Officeof Naval Research (DARPA-ONR) under Contract N00014-03-01-0636.

D. Lee, J. S. Hilton, C. H. Chen, and S. Liu are with the University of Dayton, Dayton, OH 45469 USA (e-mail: Don.Lee@udri.udayton.edu; hiltonjs@udri.udayton.edu; Christina.Chen@udri.udayton.edu; lius@udri.udayton.edu).

M. Q. Huang is with UES, Incorporated, Dayton, OH 45432 USA (e-mail: Meiqing.Huang@wpafb.af.mil).

Y. Zhang and G. C. Hadjipanayis are with the Department of Physics and Astronomy, University of Delaware, Newark, DE 19716 USA (e-mail: yzhang@physics.udel.edu;).

Digital Object Identifier 10.1109/TMAG.2004.829246

II. Experiments

Bulk, nanocomposite rare-earth magnets having compositions of (Nd, Pr, Dy)$_x$Fe$_{100-x-y-z-u-v}$Co$_y$Al$_z$Ga$_u$B$_v$ with $x = 8$–11.6, $y = 6$–6.3, $z = 0$–0.2, $u = 0$–0.2, and $v = 5.6$–10.0 were prepared using induction melting, melt spinning, hot press, and hot deformation. These technologies have been used for producing commercial Nd–Fe–B magnets with Nd $\approx$ 13–14 at% for many years [7], [8]. After melt spinning with a wheel speed of 35 m/s, the overquenched ribbons were crushed into powder particles of < 425 μm and then hot pressed at 620 °C–740 °C under 172 MPa in vacuum. The hot press took only 2 min including heating and cooling to 100 °C, therefore, excessive grain growth could be avoided. In order to obtain anisotropic nanocomposite magnets, the hot-pressed magnet specimens were further hot deformed at ~900 °C under ~ 35 MPa. The hot-pressed isotropic and hot-deformed anisotropic magnet specimens are of diameters equal to or greater than 12 mm.

Closed-circuit magnetic characterizations were performed using a hysteresisgraph at room temperature. Transmission electron microscopy (TEM) was used to observe microstructures of the hot-deformed magnet specimens. X-ray diffraction (XRD) was used to analyze the crystallographic texture of the hot deformed anisotropic magnet specimens.

III. Results and Discussions

A. Isotropic Nanocomposite Magnets

Bulk, isotropic nanocomposite magnets with full density of ~ 7.6 g/cm^3 were readily obtained after the hot press. Fig. 1 shows variation of magnetic properties of the hot-pressed isotropic $(Nd_{0.93}Pr_{0.05}Dy_{0.02})_xFe_{87.7-x}Co_{6.3}Al_{0.2}Ga_{0.2}B_{5.6}$ magnets with $x = 8$, 9, 10, 10.5, 11, and11.6 as a function of the amount of α-Fe phase in the composite magnets. It can be seen from Fig. 1 that increases in the magnetically soft α-Fe amount led to a gradual increase in remanence; however, the intrinsic coercivity sharply dropped. These two conflicting factors lead to a peak of the maximum energy product at around 12.5 vol% α-Fe phase (or 10 at% rare earth content).

The hot-press temperature has a strong effect on the magnetic properties of the hot-pressed isotropic $Nd_5Pr_5Dy_1Fe_{73}Co_6B_{10}$ magnets. As shown in Fig. 2, the intrinsic coercivity is reduced with increases in the hot press temperature as a result of grain growth at higher temperatures. A peak $(BH)_{max}$ of 16 MGOe was obtained when hot pressed at 660 °C.

The best $(BH)_{max}$ of 16.2 MGOe was obtained in $Nd_{9.3}Pr_{0.5}Dy_{0.2}Fe_{77.7}Co_{6.3}Al_{0.2}Ga_{0.2}B_{5.6}$ as shown by curves A in Fig. 5. This value is slightly higher than that of the

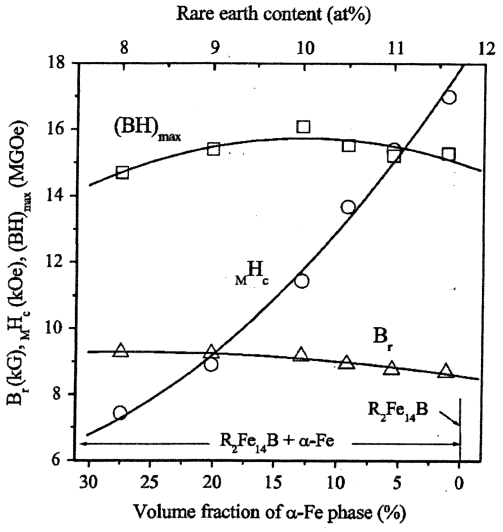

Fig. 1. Variation of magnetic properties as a function of the α-Fe phase amount in isotropic $(Nd_{0.93}Pr_{0.05}Dy_{0.02})_xFe_{87.7-x}Co_{6.3}Al_{0.2}Ga_{0.2}B_{5.6}$ magnets with x = 8–11.6.

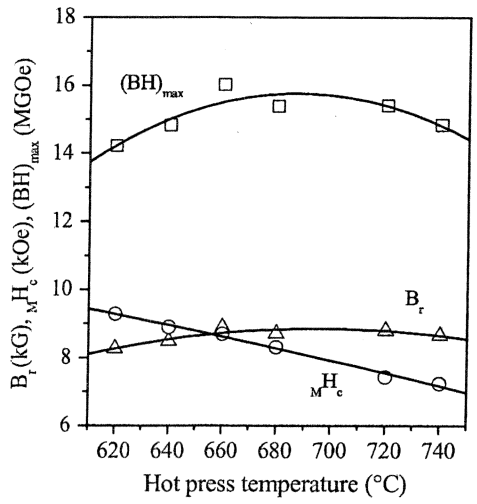

Fig. 2. Effect of hot-press temperature on magnetic properties of isotropic $Nd_5Pr_5Dy_1Fe_{73}Co_6B_{10}$ magnets.

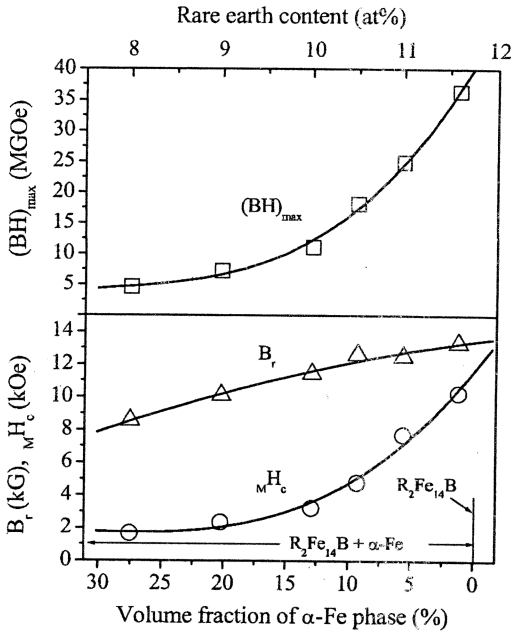

Fig. 3. Magnetic properties vs. the amount of α-Fe phase in anisotropic $(Nd_{0.93}Pr_{0.05}Dy_{0.02})_xFe_{87.7-x}Co_{6.3}Al_{0.2}Ga_{0.2}B_{5.6}$ magnets with x = 8–11.6.

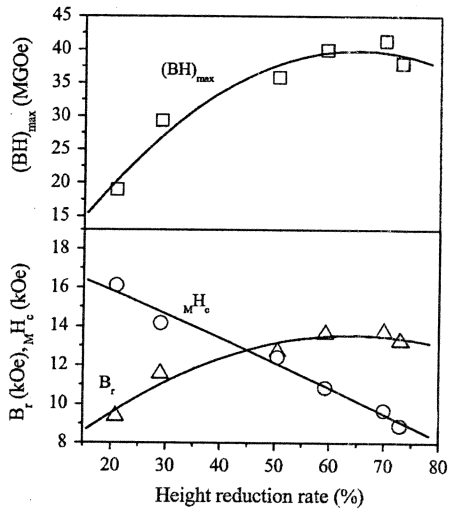

Fig. 4. Effect of height reduction rate during hot deformation on magnetic properties of anisotropic $Nd_{10.8}Pr_{0.6}Dy_{0.2}Fe_{76.1}Co_{6.3}Al_{0.2}Ga_{0.2}B_{5.6}$ magnets.

best commercial hot-pressed magnets. However, the rare earth content in the nanocomposite magnets is 26 at% lower than that in their commercial counterparts.

B. Anisotropic Nanocomposite Magnets

Further hot deformation of the isotropic nanocomposite magnets can create crystallographic texture and obtain anisotropic nanocomposite magnets. The magnetic properties, especially the maximum energy product, of anisotropic magnets are more sensitive to the rare earth content (or the amount of α-Fe phase) than isotropic magnets. Fig. 3 demonstrates the effect of the amount of the α-Fe phase on the magnetic properties of anisotropic $(Nd_{0.93}Pr_{0.05}Dy_{0.02})_xFe_{87.7-x}Co_{6.3}Al_{0.2}Ga_{0.2}B_{5.6}$ magnets with x = 8, 9, 10, 10.5, 11, and 11.6.

It can be observed from Fig. 3 that increasing the amount of the soft α-Fe phase in the magnets results in a sharp drop in the intrinsic coercivity, as in the case of isotropic magnets. However, different from that case, the remanence is also reduced with increasing the α-Fe amount. It should be noticed that this reduction in remanence is related to the fact that reducing the rare earth content makes it more difficult to create the desired crystallographic texture during hot deformation and, therefore, leads to lower remanence and poorer squareness of the demagnetization curve. These two negative factors result in a sharp drop of $(BH)_{max}$ with increasing the α-Fe amount as shown in Fig. 3.

The height reduction rate during hot deformation has strong effects on magnetic properties of anisotropic nanocomposite magnets. It can be seen from Fig. 4 that the remanence of $Nd_{10.8}Pr_{0.6}Dy_{0.2}Fe_{76.1}Co_{6.3}Al_{0.2}Ga_{0.2}B_{5.6}$ is significantly

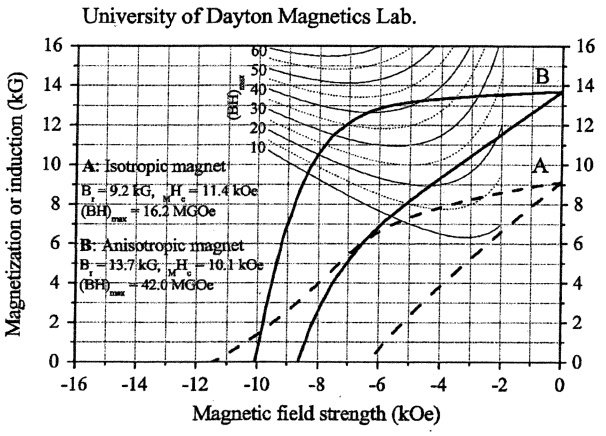

Fig. 5. Demagnetization curves of an isotropic $Nd_{9.3}Pr_{0.5}Dy_{0.2}Fe_{77.7}Co_{6.3}Al_{0.2}Ga_{0.2}B_{5.6}$ (A) and an anisotropic $Nd_{10.8}Pr_{0.6}Dy_{0.2}Fe_{76.1}Co_{6.3}Al_{0.2}Ga_{0.2}B_{5.6}$ (B).

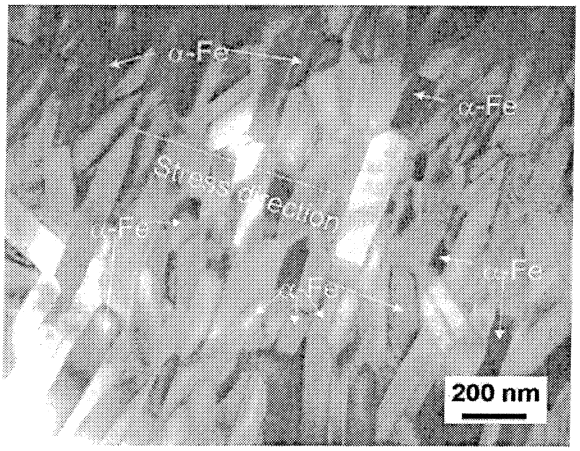

Fig. 6. TEM image of an anisotropic nanocomposite $Nd_{9.2}Pr_1Dy_{0.3}Fe_{77.5}Co_{6.1}Ga_{0.2}B_{5.7}$.

enhanced by increasing the height reduction rate, indicating that more hot deformation is favorable to nanograin alignment. As shown in Fig. 4, the maximum energy product is strongly dependent on the height reduction rate. The best $(BH)_{max}$ of 42 MGOe was achieved when hot deforming $Nd_{10.8}Pr_{0.6}Dy_{0.2}Fe_{76.1}Co_{6.3}Al_{0.2}Ga_{0.2}B_{5.6}$ with a height reduction rate of 70% as shown in Fig. 5 curve B.

The TEM study of the hot deformed anisotropic $Nd_{9.2}Pr_1Dy_{0.3}Fe_{77.5}Co_{6.1}Ga_{0.2}B_{5.7}$ revealed elongated and aligned nanograins, however, misalignment of some nanograins was observed as shown in Fig. 6.

XRD was performed on hot-deformed $Nd_{10.8}Pr_{0.6}Dy_{0.2}Fe_{76.1}Co_{6.3}Al_{0.2}Ga_{0.2}B_{5.6}$ for both a random powder and a bulk specimen on a plane perpendicular to the hot-deformation direction. As shown in Fig. 7(a), the XRD pattern on the random powder shows a typical $Nd_2Fe_{14}B$ structure with a small amount of α-Fe. On the other hand, the XRD pattern of the bulk specimen shows that reflections (00 ℓ), such as (004), (006), (008), and (105), are strengthened, indicating that the c-axes of the nanograins have been partially aligned along the

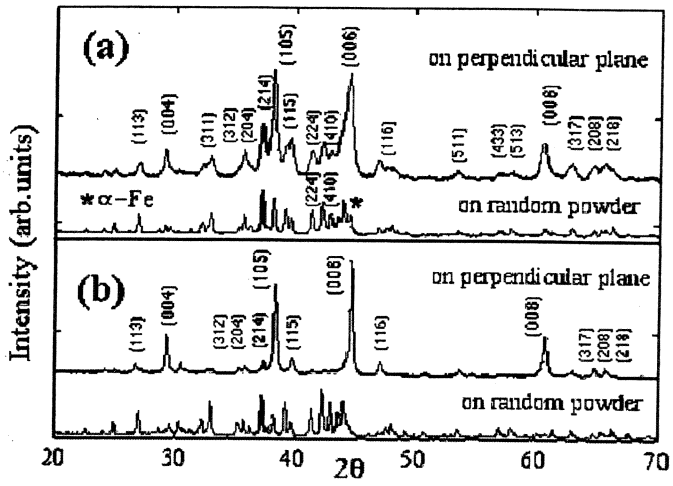

Fig. 7. XRD patterns of (a) a hot-deformed $Nd_{10.8}Pr_{0.6}Dy_{0.2}Fe_{76.1}Co_{6.3}Al_{0.2}Ga_{0.2}B_{5.6}$ nanocomposite magnet and (b) a sintered Nd–Fe–B magnet.

hot-deformation direction. In comparison to the XRD patterns of a commercial sintered anisotropic Nd–Fe–B specimen shown in Fig. 7(b), the misalignment of some nanograins in the specimen shown in Fig. 7(a) is obvious. Both the hot-pressed nanocomposite magnet presented in Fig. 7(a) and the commercial sintered Nd–Fe–B magnet presented in Fig. 7(b) have $(BH)_{max} \approx 40$ MGOe. Therefore, much higher $(BH)_{max}$ is anticipated for nanocomposite magnets with further improving their nanograin alignment.

ACKNOWLEDGMENT

The authors are grateful to Dr. V. M. Browning of DARPA, Dr. R. T. Fingers and E. M. Gregory of AFRL, and Dr. J. Christodoulou of ONR for their support.

REFERENCES

[1] R. Coehoorn, D. B. de Mooij, and C. de Waard, "Melt spun permanent magnets materials containing Fe_3B as the main phase," *J. Magn. Magn. Mater.*, vol. 80, pp. 101–104, 1989.

[2] E. F. Kneller and R. Hawig, "The exchange-spring magnet: A new material principle for permanent magnets," *IEEE Trans. Magn.*, vol. 27, pp. 3588–3600, 1991.

[3] A. Manaf, R. A. Buckley, and H. A. Davies, "New nanocrystalline high-remanence Nd-Fe-B alloys by rapid solidification," *J. Magn. Magn. Mater.*, vol. 128, pp. 302–306, 1993.

[4] R. Skomski, "Aligned two-phase magnets: Permanent magnetism of the future?," *J. Appl. Phys.*, vol. 76, pp. 7059–7064, 1994.

[5] Z. Wang, S. Zhou, M. Zhang, and Y. Qiao, "Effects of high pressure hot compaction on the formation, microstructure and magnetic properties of melt-spun α-Fe/$Re_2Fe_{14}B$-type nanocomposite magnets," in *Proc. 16th Int. Workshop REM*, vol. 2, 2000, pp. 687–693.

[6] Z. Chen, Y. Zhang, M. Daniil, H. Okumura, G. C. Hadjipanayis, and Q. Chen, "Review of rare earth nanocomposite magnets," in *Proc. 16th Int. Workshop REM*, vol. 1, 2000, pp. 449–464.

[7] R. W. Lee, "Hot-pressed neodymium-iron-boron magnets," *Appl. Phys. Lett.*, vol. 46, pp. 790–791, 1985.

[8] J. J. Croat, "Current status of rapidly solidified Nd-Fe-B permanent magnets," in *Proc. 11th Int. Workshop REM*, vol. I, S. G. Sankar, Ed., 1990, pp. 1–9.

[9] D. Lee, J. S. Hilton, S. Liu, Y. Zhang, G. C. Hadjipanayis, and C. H. Chen, "Hot-pressed and hot-deformed nanocomposite (Nd, Pr, Dy)$_2Fe_{14}B/\alpha$-Fe-based magnets," *IEEE Trans. Magn.*, vol. 39, pp. 2947–2949, 2003.

Available online at www.sciencedirect.com
SCIENCE DIRECT®
ELSEVIER
Journal of Magnetism and Magnetic Materials 295 (2005) 257–262
Journal of magnetism and magnetic materials
www.elsevier.com/locate/jmmm

Textured Co nanowire arrays with controlled magnetization direction

H.N. Hu[a,*], H.Y. Chen[a], S.Y. Yu[a], J.L. Chen[a], G.H. Wu[a], F.B. Meng[b], J.P. Qu[b], Y.X. Li[b], H. Zhu[c], John Q. Xiao[c]

[a]*Beijing National Laboratory for Condensed Matter Physics, State Key Laboratory for Magnetism, Institute of Physics, Chinese Academy of Sciences, Beijing 100080, China*
[b]*School of Material Sciences and Engineering, Hebei University of Technology, Tianjin 300130, People's Republic of China*
[c]*Department of Physics and Astronomy, University of Delaware, Newark, DE 19716, USA*

Received 11 November 2004; received in revised form 21 December 2004
Available online 5 February 2005

Abstract

Textured HCP Co nanowires with preferentially oriented (1 0 0) along the growth direction were fabricated by electrodeposition at high potential. Further increase of deposition potential results in the formation of twist wires with circumferential strain. These conclusions are unambiguously reached by combining TEM, XRD rocking curves and pole figures. The magnetic properties are determined by the combination of magnetocrystalline, shape, and stress anisotropies and magnetostatic interaction. Consequently, the magnetic easy axis can be tuned with structure and temperature, thus paving the road for magnetic nanowire array use in applications where self-biasing of magnetization is necessary.

PACS: 75.75; 81.07; 81.07.B

Keywords: Nanowire electrodeposition texture; Porous anodic aluminum oxide

1. Introduction

One-dimensional nanostructures are of great interest because of potential applications in areas such as high-density perpendicular magnetic recording media and nanosensors [1–3]. More recently, exciting developments in magnetic domain switching by spin-polarized currents seem to promise breakthroughs in magnetic memory technology [4,5]. A spin-polarized current of a high current density can be easily achieved in one-dimensional structure. Precise structural control of these one-dimensional structures allows us to understand the mechanism of current-driven spin

*Corresponding author. Tel.: +86 1 082 649 247; fax: +86 1 082 649 485.
E-mail address: hnhu@aphy.iphy.ac.cn (H.N. Hu).

0304-8853/$ - see front matter © 2005 Elsevier B.V. All rights reserved.
doi:10.1016/j.jmmm.2005.01.010

dynamics. The synthesis and precise control of such a magnetic nanostructure on a large scale is a challenging issue in materials science. One strategy is to electrodeposit magnetic nanowires into nanochannels of porous anodic aluminum oxide (AAO) templates, which have been utilized by many groups to prepare magnetic metals including Ni, Co, and Fe [1–3,6–13]. In the case of Co nanowires, almost all electrodeposited Co nanowires are polycrystalline. In this letter we report the preparation of (1 0 0) oriented Co nanowires with hexagon close packed (HCP) structure in a controllable fashion. The structure has been verified with conventional X-ray diffraction (XRD), scanning electron microscopy (SEM) and transmission electron microscopy (TEM). Detailed X-ray rocking curve and pole figure measurements reveal the formation of twisted HCP structure by controlling the fabrication parameters. The circumferential tension in twisted HCP structures significantly influences the magnetic anisotropy and can be used to control the magnetization direction in Co nanowire array.

2. Experiment procedure

Porous anodic aluminum oxide (AAO) template was prepared by a two-step anodizing process on aluminum foils [14,15]. Al foil with purity of 99.999% was anodized in 0.3 M under a constant voltage of 40 V at 12 °C. After anodization, the remaining aluminium substrate and its barrier layer at the bottom of the AAO template were removed to obtain the through holes AAO template with pore length of 40 μm and uniform diameters of 60 nm. A Cu layer was sputter deposited on one side of the AAO template to serve as the working electrode in a two-electrode electrochemical cell. An aqueous bath (pH ~ 3.0) containing 0.2 M Co^{2+} and H_3BO_3 (30 g/l) was used to prepare Co nanowire at room temperature with constant potential of −2 V or higher. Co-1 and Co-2 samples were deposited from the same electrolyte with potential of −1.95 and −2.15 V, respectively. SEM and TEM were used to characterize the morphology and the structure of the nanowires. The X-ray rocking curve and pole figure measurements were carried out in a Philips X'Pert MPD instrument using the Cu Kα radiation. The magnetic measurements were performed using a superconducting quantum interference device (SQUID) magnetometer.

3. Results and discussion

Fig. 1 shows the SEM and TEM results on the Co nanowire arrays and an isolated nanowire. The length of Co nanowires is about 40 μm, consistent with AAO template thickness. The wires show uniform diameter of about 60 nm, resulting in a high aspect ratio of about 700. Selected-area electron diffraction (SAED) pattern has been performed on different Co nanowires and different positions on individual wires. All

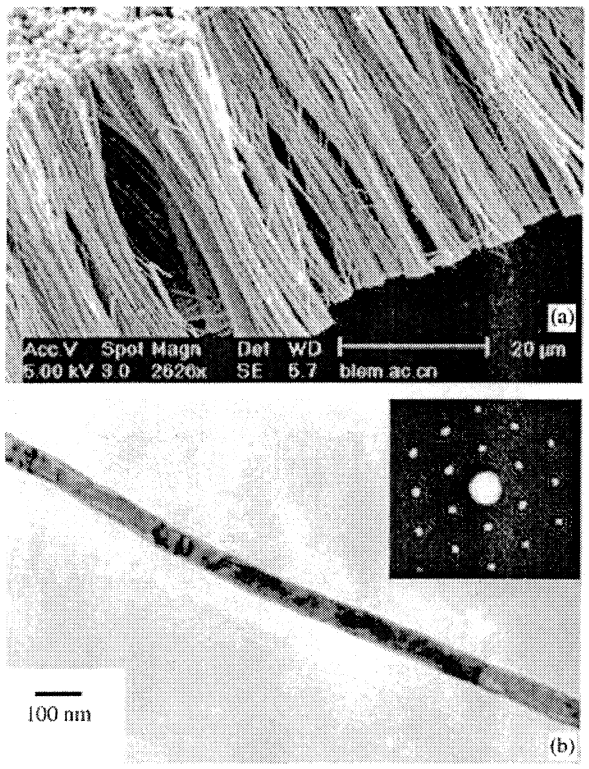

Fig. 1. (a) SEM images of cross-section view of Co nanowire arrays after removing the AAO template; (b) typical bright field TEM image of a single-crystal Co nanowire and electron diffraction from the same sample (inset) showing the HCP structure with *c*-axis aligned perpendicular to the wire.

obtained diffraction patterns show hexagonal symmetry (inset in Fig. 1b), indicating that wires are single crystal HCP structure with c-axis perpendicular to the wire.

Fig. 2 shows XRD spectra of Co nanowire arrays embedded in templates. All samples show only a sharp (1 0 0) peak of HCP Co, indicating the preferential orientation of whole single-crystalline wires. The inset of Fig. 2 shows the results from X-ray rocking curve of (1 0 0) reflection. Most of samples, denoted as Co-1, show one sharp peak centered at the specular angle of 20.8° with narrow peak widths at half-maximum (FWHM) in the range of 2.38–5.51°. Assuming a Gaussian distribution, these results indicate that at least 75% of the wires have a preferential orientation within 1.2–2.8° of the [1 0 0] direction. Similar analyses for polycrystalline samples show a larger distribution angle up to 9° [8]. Samples electrodeposited at the potential of −2.15 V (denoted as Co-2) show very different rocking curves, indicated in the inset of Fig. 2. Although they have the same sharp (1 0 0) XRD peak as Co-1 samples, there is no peak at 20.8° in rocking curves. Interestingly, there are two twin-peaks with the same intensity at 15.7° and 26.1°, respectively (i.e., about ±5° mirror imaging the [1 0 0] characteristic angle of 20.8°).

Combining the results from SEM, TEM, XRD and X-ray rocking curves, we can conclude that each individual nanowire is single crystal and has [1 0 0] preferred orientation along the wires. The nanowires array has random c-axis distribution in the AAO template plane. The sharp (1 0 0) peak in XRD and the narrow FWHM of rocking curves of 2.38° indicates the excellent pore parallelity in AAO templates as well as a near-perfect texture in our nanowire arrays. This clearly indicates that optimum deposition condition can be achieved to fabricate well-textured nanowires array over a large area. It is important to emphasize that the unusual twin-peak in rocking curves of Co-2 samples cannot be explained by the parallelity deviation in pore structure, nor can it be explained with the deviation from the overall orientation. A poor parallelity only increases the FWHM of the rocking curves, and orientation deviation increases the FWHM and shifts the peak position.

To explain the double peaks in rocking curves for Co-2 samples, we performed pole figure measurement and (1 0 0) and (1 0 1) pole figures for Co-1 and Co-2 samples as shown in Fig. 3. The tilt angle (α) was varied from 0–85° in steps of 5°. The azimuth angle (β) was varied from 0–355° in steps of 5°. Fig. 3(a) shows a well-defined HCP (1 0 0) sharp peak at $\alpha = 0°$ for Co-1, further confirming the high degree of (1 0 0) alignment of

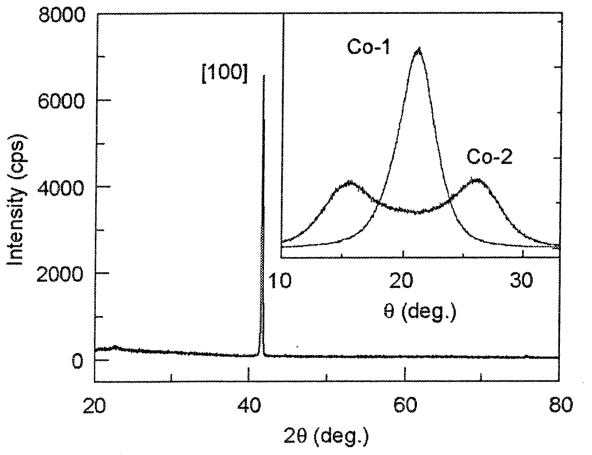

Fig. 2. X-ray diffraction (XRD) spectrum of Co nanowire arrays embedded in porous alumina template. Inset is the (1 0 0) rocking curve for two types of nanowire arrays.

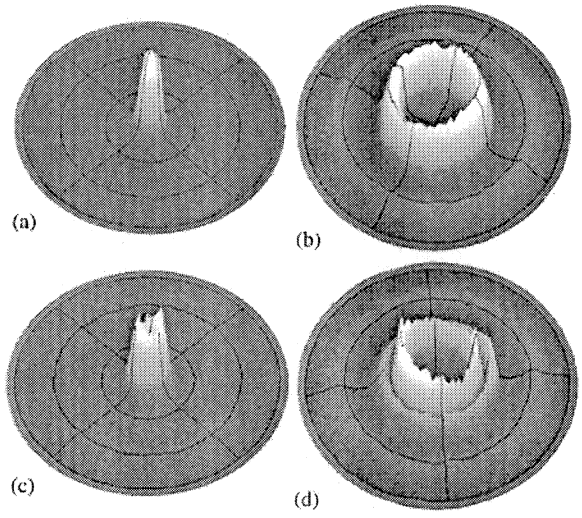

Fig. 3. Three-dimensional (1 0 0) (a) and (1 0 1) (b) pole figures of Co-1 samples and three-dimensional (1 0 0) (c) and (1 0 1) (d) pole figures of Co-2 samples, respectively.

nanowires along the wire direction in Co-1 samples. The HCP (1 0 1) peak in Fig. 3(b) shows the diffraction maximum as a crateriform ring located at $\alpha = 30°$, corresponding to the angle between the neighboring [1 0 0] and [1 0 1] planes. This means that the ⟨1 0 1⟩ axis of nanowires are randomly distributed in the array. Based on this observation, one may easily conclude that the *c*-axis of single-crystalline wires also distribute randomly in the array plane.

For Co-2 samples, the (1 0 0) peak has a volcano shape located at about $\alpha = 5°$ surrounding the center of the pole figure (Fig. 3c). Its (1 0 1) pole figure shows two crateriform rings located at about $\alpha = 25°$ and 35°, respectively. These shifted angles are consistent with twin-peak pattern observed in (1 0 0) rocking curve (inset of Fig. 2). If twin peak pattern in rocking curve suggests lattice structure shown in Fig. 4d, then the pole figure suggests that such distortion have circular symmetry. Here, we propose a model of twisted wire shown in Fig. 4 which will result in this cone structure, this model is also consistent with observed magnetic properties to be discussed later.

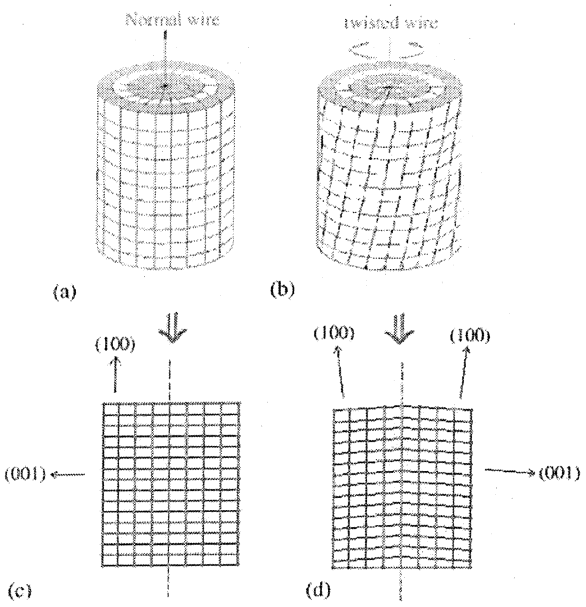

Fig. 4. The twisted nanowire model. The cross-section of both normal and twisted nanowires are shown below the three-dimensional diagram. (1 0 0) and (0 0 1) orientations are labeled in the figure. (See text for detailed explanation).

If the wire is twisted as it grows (Fig. 4b), the atoms on the second plane will not be directly above these on the first plane, but shifted along the twisted direction. Consequently, the distance between the first and second planes is reduced. The reduction is most on the outmost radius and zero along the center line since the twist creates the largest displacement at the outmost radius. It is clear the formation of this structure must be accompanied by dislocations or defects. The cross-sectional view of such a distortion is shown in Fig. 4d. The angle between wire axis and (1 0 0) orientation for the twisted wire, in our case, should be about 5°. This effect gives rise to the twin peaks shown in the inset of Fig. 2, and in the pole figure volcano-like (1 0 0) peak at $\alpha = \pm 5°$ in Fig. 3c. Similar analysis shows that double crateriform rings should be observed for (1 0 1) orientation located at $\alpha = 30 \pm 5°$. Experimental pole figure of (1 0 1) for twisted nanowire array is shown in Fig. 3d. This is the only structure that explains consistently the results shown in the rocking curves and pole figures. This model has never been proposed before, since no pole figure studies have been done in nanowire array.

Magnetic properties were measured by a SQUID magnetometer from 5 to 300 K. Fig. 5 shows the hysteresis loops of Co-1 (a, b), Co-2 (c, d), and Co-2 with template partially etched away (e, f) at 5 and 300 K, respectively. The

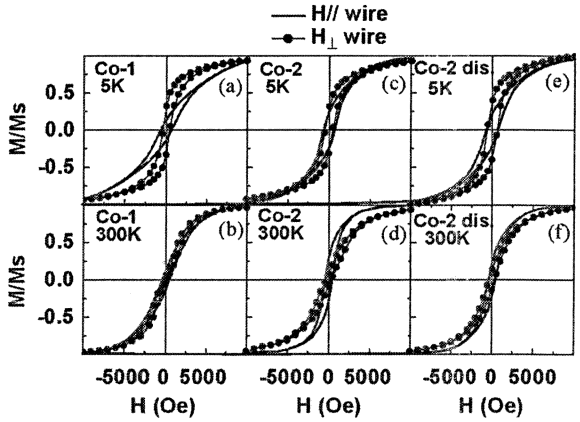

Fig. 5. Hysteresis loops of sample Co-1 (a, b), Co-2 (c, d) and Co-2 with template partially etched away (e, f). Field is applied perpendicular (- - -) or parallel (—) to the nanowires.

control of anisotropy by structure and temperature is clear: for untwisted Co-1 wire array, the easy axis is perpendicular to the wires at low temperature and gradually decreases with increasing temperatures, while twisted Co-2 wire array shows an easy axis along the wires at high temperatures and decreases with decreasing temperatures. The total anisotropy represents the competition among magnetocrystalline, shape, and stress anisotropies and dipolar interaction [7,9]. For HCP Co, the magnetocrystalline anisotropy creates an easy magnetization direction along the c-axis, which is reduced due to the random c-axis orientations in both Co-1 and Co-2 samples. The dipolar interaction, which is the same for both samples because of the same diameter and length, leads to an easy magnetization direction perpendicular to the nanowire array. If the stress effect in the Co-1 samples is neglected, then the sum of magnetocrystalline anisotropy and dipolar interaction is larger than the shape anisotropy. This results in an easy magnetization direction perpendicular to the nanowires. The magnetocrystalline anisotropy decreases faster than shape anisotropy and dipolar interaction with increasing temperature, leading to the temperature-dependent behaviors observed in sample Co-1. In sample Co-2 , in addition to crystalline and shape anisotropies and dipolar interaction, there is a stress anisotropy, $E_{me} = \frac{3}{2}\lambda\sigma \sin^2\theta$, where λ is the magnetostriction coefficient, σ the stress, and θ the angle between M_s and σ. In Co-2, the positive circumferential tensile stress σ and negative λ for Co along the c-axis gives rise to a negative stress anisotropy, implying that along the wire direction is an easy axis [16]. At low temperature, the stress and shape anisotropy balances the magnetocrystalline anisotropy and dipolar interaction, resulting in similar magnetic properties in two directions. For the same reason as in Co-1, at the room temperature, the magnetization prefers to be along the wire direction. It should be noted that the coercivity of Co-2 samples is always larger than that of Co-1 samples because of this additional stress anisotropy. To confirm the stress anisotropy in Co-2 sample, the Al_2O_3 template was partially removed to release portion of stress, and the magnetic properties at 5 and 300 K are shown in Fig. 4(e,f). As anticipate the hysteresis loops are between those non-stressed Co-1 nanowire arrays and stressed (twisted) Co-2 nanowire array (Co-2), clearly demonstrating that the stress anisotropy plays a crucial role here

4. Conclusions

Textured Co nanowire with preferred growth orientation of (100) has been fabricated by electrodeposition at high potential. Further increase of deposition potential results in the formation of twist wires. These conclusions are unambiguously reached by combining, TEM, XRD rocking curve and pole figure measurements. The magnetic properties are determined by the combination of magnetocrystalline, shape, and strain anisotropies and dipolar interaction. Consequently, the magnetic easy axis can be tuned with structure and temperature, thus paving the road for magnetic nanowire array use in applications where self-biasing of magnetization is necessary.

Acknowledgements

This work was supported by National Natural Science Foundation of China Grant no. 50371101. JQX would also like to acknowledge the support from Grant AFOSR F49620-03-1-0351 and American Chemical Society Petroleum 40057-AC5M.

References

[1] T.M. Whitney, J.S. Jiang, P.C. Searson, C.L. Chien, Science 261 (1993) 1316.
[2] D. Almawlawi, N. Coombs, M. Moskovits, J. Appl. Phys. 70 (1991) 4421.
[3] T. Thurn-Albrecht, J. Schotter, G.A. Kastle, N. Emley, T. Shibauchi, L. Krusin-Elbaum, K. Guarini, C.T. Black, M.T. Tuominen, T.P. Russell, Science 290 (2000) 2126.
[4] M. Klaui, C.A.F. Vaz, J.A.C. Bland, W. Wernsdorfer, G. Faini, E. Cambril, L.J. Heyderman, APL 83 (2003) 105.
[5] T.Y. Chen, Y. Ji, C.L. Chien, APL 84 (2004) 380.
[6] P.M. Paulus, F. Luis, M. KroK II, G. Schmid, L.J. de Jong, J. Magn. Magn. Mater. 224 (2001) 180.
[7] R. Ferré, K. Ounadjela, J.M. George, L. Piraux, S. Dubois, Phys. Rev. B 56 (1997) 14066.

[8] J.-L. Maurice, D. Imhoff, P. Etienne, O. Durand, S. Dubois, L. Piraux, J.-M. George, P. Galtier, A. Fert, J. Magn. Magn. Mater. 184 (1998) 1.
[9] K. Ounadjela, R. Ferre', L. Louail, J.M. George, J.L. Maurice, L. Piraux, S. Dubois, J. Appl. Phys. 81 (1997) 5455.
[10] H. Zeng, R. Skomski, L. Menon, Y. Liu, S. Bandyopadhyay, D.J. Sellmyer, Phys. Rev. B 65 (2002) 134426.
[11] Shihui Ge, Xiao Ma, Chao Li, Wei Li, J. Magn. Magn. Mater. 226–230 (2001) 1867.
[12] L. Piraux, S. Dubois, J.L. Duvai, K. Ounadjela, A. Fert, J. Magn. Magn. Mater. 175 (1997) 127.
[13] Y. Henry, K. Ounadjela, L. Piraux, S. Dubois, J.-M. George, J.-L. Duvail, Eur. Phys. J. B 20 (2001) 35.
[14] H. Masuda, K. Fukuda, Science 268 (1995) 1466.
[15] Y.W. Wang, L.D. Zhang, G.W. Meng, X.S. Peng, Y.X. Jin, J. Zhang, J. Phys. Chem. B 106 (2002) 2502.
[16] B.D. Cullity, Introduction to Magnetic Materials, Addison-Wesley, MA, 1972, pp. 260–264.

INSTITUTE OF PHYSICS PUBLISHING JOURNAL OF PHYSICS D: APPLIED PHYSICS

J. Phys. D: Appl. Phys. **38** (2005) 1337–1341 doi:10.1088/0022-3727/38/9/002

Magnetic states and structural transformations in $Sm(Co,Cu)_5$ and $Sm(Co,Fe,Cu)_5$ permanent magnets

A M Gabay[1], P Larson[2,3], I I Mazin[2] and G C Hadjipanayis[1]

[1] Department of Physics and Astronomy, University of Delaware, Newark, Delaware 19716, USA

[2] Center for Computational Materials Science, Naval Research Laboratory, 4555 Overlook Avenue SW, Washington, DC 20375, USA

E-mail: gabay@udel.edu

Received 22 September 2004, in final form 19 January 2005
Published 22 April 2005
Online at stacks.iop.org/JPhysD/38/1337

Abstract

We have studied the stability of $RCo_{5-x}Cu_x$ (R = Y, Sm) compounds with respect to phase separation. First principles density functional calculations imply that (i) decomposition into two phases having different x is energetically favourable and (ii) both the stable x values and the Cu atomic site preferences depend on the magnetic state of the alloys. Guided by this result, we studied the structure and magnetic properties of different $Sm(Co,Cu)_5$ and $Sm(Co,Fe,Cu)_5$ alloys. Separation into two chemically dissimilar $Sm(Co,Cu)_5$ phases is typical for the as-made $Sm(Co,Cu)_5$ alloys. We also observed in different alloys a universal correlation between the room-temperature coercivity and the magnetic state at the temperature of annealing. The coercivity increases significantly if annealed 100–140°C below the Curie temperature; in particular, for $SmCo_{2.25}Fe_{0.75}Cu_2$, the room-temperature coercivity increases from 12.3 to 37.3 kOe. The possibility of different magnetic state-dependent structure transformations is discussed. The experimental results do not support the spinodal decomposition theory, so we suggest that the coercivity increase might be caused by a change in preferred atomic site occupancies.

1. Introduction

In spite of many experimental studies, the large coercivity in bulk $Sm(Co,Cu)_5$ alloys discovered more than three decades ago [1] is still not completely understood. According to Oesterreicher *et al* [2] the magnetic hardness in these pseudobinary compounds may be of an intrinsic nature, resulting from site disorder and the high magnetic anisotropy. On the other hand, the well-known increase of coercivity in $Sm(Co,Cu)_5$ alloys upon annealing at relatively low temperatures of about 500–500 °C has been associated with spinodal decomposition into Co- and Cu-rich $Sm(Co,Cu)_5$ phases [3–5]. In the later studies [6], however, the spinodal decomposition in the $Sm(Co,Cu)_5$ alloys has been questioned.

[3] Present address: Department of Physics, Case Western Reserve University, 10900 Euclid Avenue, Cleveland, OH 44106, USA.

In the model by Mitchell and McCurrie [7], the Co and Cu microsegregation formed during alloy casting evolves with annealing into a sort of cellular structure, which is responsible for the coercivity. Recently Yamashita [8] even suggested that the coercivity in $Sm(Co,Cu)_5$ can be caused by the Co precipitates along the grain boundaries.

Though $Sm(Co,Cu)_5$ compounds do not have a direct practical application because of their relatively low magnetization, it is well established that $Sm(Co,Cu)_5$ plays a critical role in the coercivity of Sm_2Co_{17}-based magnets—the hard magnetic materials of great practical importance. Typically, when modelling coercivity in the 2 : 17 magnets, the $Sm(Co,Cu)_5$ cell-boundary constituent is considered as a single phase with a certain set of physical properties [9]. However, some experimental results [10] may be interpreted in favour of a two-phase structure.

0022-3727/05/091337+05$30.00

In this work, we tried to examine the structural transformations in $Sm(Co,Cu)_5$ and their relevance to the magnetic hardness of these alloys. We started with theoretical calculations and used their results (the predicted phase separation and possible effect of magnetic states of the alloys on their structure) to guide our experimental efforts. The latter, therefore, were focused on the structure and magnetic properties of the as-made alloys, homogenized alloys and the alloys annealed in the vicinity of their Curie temperature.

2. Calculation and experimental details

Density functional calculations for $RCo_{5-x}Cu_x$ compounds with R = Y and Sm have been performed with the full-potential, linearized augmented plane wave (LAPW) method [11] using the WIEN2k code [12] and the linearized muffin-tin orbital method [13] within the atomic sphere approximation (LMTO-ASA) using the STUTTGART-4.7 package [14]. The former method is very accurate but somewhat slow, while the latter is approximate but very fast. Details of the calculations are available elsewhere [15].

Experimental results were obtained for $SmCo_{5-x}Cu_x$ with x = 1, 1.5, 2 and also for $SmCo_{2.25}Fe_{0.75}Cu_2$. The alloys were prepared from pure components by arc-melting on a water-cooled copper hearth under an argon atmosphere. Excess of Sm was added to compensate the evaporation loss of this element. The ingots were re-melted several times to ensure homogeneity; some of them (particularly those with Fe) were additionally homogenized at 1050°C for 50 h. Alloy samples were annealed at the temperature T_A ranging from 350°C to 550°C for 50 h (unless some other time is specified). The homogenization and annealing treatments were followed by quenching in water. X-ray diffraction (XRD) data were collected with the Cu-Kα radiation. Microstructure was studied for non-etched samples by scanning electron microscopy (SEM) with a JEOL JSM-6330F instrument. The room-temperature magnetic hysteresis loops were measured for coarse powders with a Quantum Design MPMS magnetometer and a vibrating sample magnetometer (VSM). The powder samples were magnetically aligned, except those used for measuring initial magnetization curves. Thermomagnetic analysis at the field of 0.1 kOe was performed with the VSM for 100–120 mg alloy pieces.

3. Theoretical stability analysis for $Sm(Co,Cu)_5$

The stability of the $Sm(Co,Cu)_5$ compounds has been analysed as follows: consider a graph of the total energy of $RCo_{5-x}Cu_x$ as a function of x with a straight line connecting the energy values of pure RCo_5 and RCu_5. This line represents the energies of mechanical mixtures of the two binary phases. Subtracting these values from the energies calculated for $RCo_{5-x}Cu_x$, we obtain $\Delta E(x)$, the difference between the energy of $RCo_{5-x}Cu_x$ and that of the $(1/5)[(5-x)RCo_5 + xRCu_5]$ mixture for every given x. Figure 1 shows $\Delta E(x)$ calculated by different techniques for R = Sm and Y in a magnetic state where the Cu atoms prefer to occupy the 2*c* atomic sites [16]. LAPW calculations are much more costly in terms of computer time than those for LMTO-ASA; Sm calculations require special treatment for *f*-electrons [15]

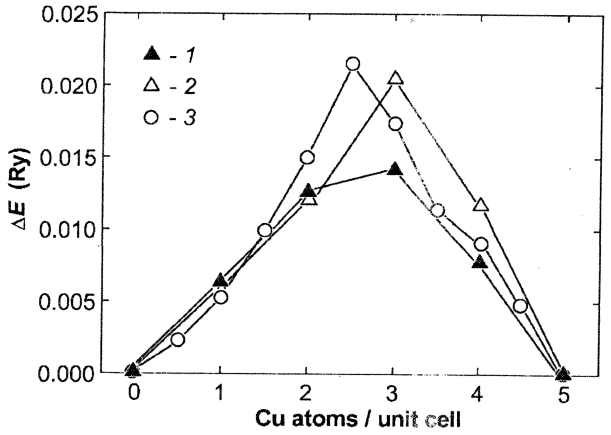

Figure 1. Deviation of the $RCo_{5-x}Cu_x$ energy from that for the $RCo_5 + RCu_5$ mixture calculated (1) by LAPW for R = Sm, (2) by LAPW for R = Y and (3) by LMTO-ASA for R = Y. All the compounds are magnetic and the Cu atoms prefer the 2*c* sites.

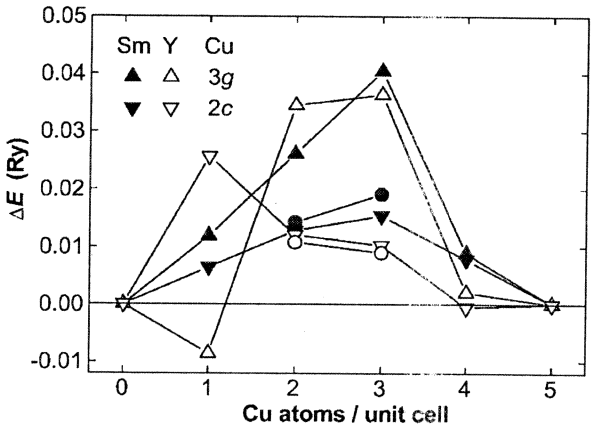

Figure 2. Deviation of the $RCo_{5-x}Cu_x$ energy from that for the RCo_5 + RCu_5 mixture calculated by LAPW for magnetic $SmCo_{5-x}Cu_x$ (●,▲,▼) and non-magnetic $YCo_{5-x}Cu_x$ (○,△,▽) with the Cu atoms preferring 3*g* sites, 2*c* sites (▲,△), or having no preferential site occupancies (●,○).

and, therefore, are even slower. Fortunately, the differences among all three sets of calculations are not qualitatively important, which allows us to use the faster method for further analysis.

The energy associated with the 3*d* magnetism of Co is substantial. Non-magnetic calculations are not meaningful in the Sm compounds since the Sm 4*f* shells retain local magnetic moments at any temperature. However, the similarity of the $\Delta E(x)$ curves for Y and Sm in the magnetic calculations suggests that the *f*-shell magnetism, as opposed to the Co *d*-shell magnetism, is not important for structural stability. Figure 2 shows the calculated $\Delta E(x)$ for magnetic $SmCo_{5-x}Cu_x$ and non-magnetic $YCo_{5-x}Cu_x$ for different preferred occupancies of the atomic sites. According to the calculations, in the magnetic regime (figures 1 and 2 for Sm) all the intermediate $RCo_{5-x}Cu_x$ compounds have total energies higher than that of a mixture of RCo_5 and RCu_5 and, therefore, are unstable upon decomposition into RCo_5 and RCu_5. In the non-magnetic regime (figure 2 for Y), the most stable compositions are RCo_4Cu_1 and RCo_1Cu_4. Interestingly, according to the calculations, the structure may

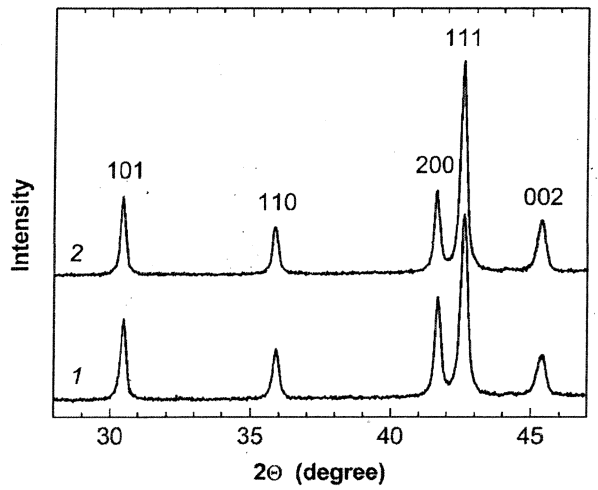

Figure 3. Powder XRD spectra of $SmCo_3Cu_2$ alloy: both as-made (1) and annealed at 350°C (2) samples have the $CaCu_5$-type structure.

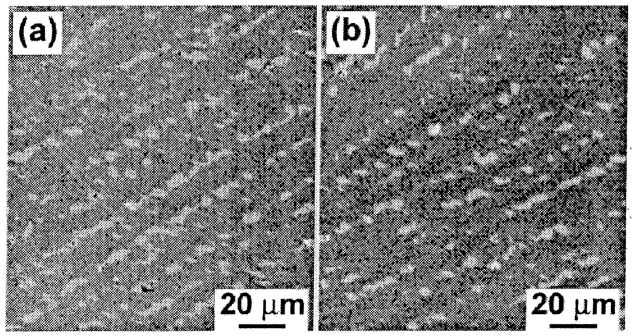

Figure 4. SEM backscattered electron images of $SmCo_3Cu_2$ samples: (*a*) the as-made alloy and (*b*) alloy annealed at 350°C have a two-phase structure.

depend on whether annealing was done below or above the Curie temperature. For instance, the RCo_4Cu_1 alloy is expected to be a single phase if annealed above the Curie temperature but a mixture of RCo_5 and RCu_5 if annealed below the Curie temperature. The calculations also suggest that atomic site preferences depend on the magnetic state of the alloy. As can be seen from figure 2, calculations in the magnetic regime suggest that the Cu atoms prefer the 2*c* sites for any x value, while in the non-magnetic regime the 3*g* sites become more preferable for $0 < x < 2$ with disordered occupancies for $2 \leqslant x \leqslant 3$.

4. Microstructure and magnetic properties of as-made and homogenized alloys

XRD characterization of the as-made $SmCo_{5-x}Cu_x$ alloys with $x = 1$, 1.5 and 2 clearly shows the presence of a single structure, identified as $CaCu_5$ (space group $P6/mmm$). The representative part of the XRD spectrum for $SmCo_3Cu_2$ is shown in figure 3 (curve 1). However, the SEM image of the backscattered electrons reveals what appears to be a two-phase structure (figure 4(*a*)). This is consistent with the reports [3, 5, 7] about a strong tendency of the as-cast $Sm(Co,Cu)_5$ alloys for microsegregation. The

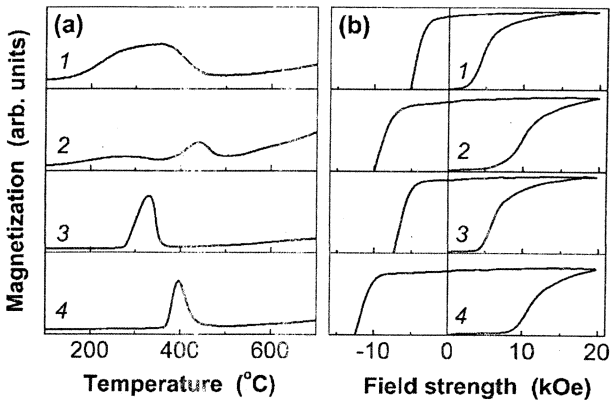

Figure 5. (*a*) Thermomagnetic curves and (*b*) magnetization curves of the $SmCo_3Cu_2$ alloy: as-made (1); annealed at 350°C (2); homogenized at 1050°C (3); homogenized at 1050°C and annealed at 350°C for 200 h (4).

resulting Co- and Cu-enriched areas have the same crystal structure and cannot be distinguished with powder XRD [7]. Homogenization at 1050°C eliminates this segregation (the corresponding SEM image is not shown), again in good agreement with [3]. The heating thermomagnetic curves shown in figure 5(*a*) illustrate the emergence of a uniform magnetic phase (curve 3) from a set of phases with a broad range of Curie temperatures (curve 1).

It is interesting to compare the effects of low-temperature annealing on the as-made and homogenized alloys. As can be seen in figures 3 and 4, XRD and TEM show no changes in the non-homogenized $SmCo_3Cu_2$ sample after annealing at 350°C. However, considerable changes can be observed in the magnetic measurements (figure 5, curves 1 and 2). As a result of annealing, the coercivity H_c increases two times and the thermomagnetic analysis suggests a split in the Curie temperatures. The highest observed Curie temperature T_C increases with annealing. Similarly, in the homogenized sample, both H_c and the only observed T_C increase with annealing (figure 5, curves 3 and 4). Note the difference in annealing times for the as-made and homogenized alloys—this reflects the fact that H_c of the as-made $Sm(Co,Cu)_5$ alloys reached its maximum with annealing in a shorter time than the H_c of the homogenized alloys.

It appears that the increase of coercivity in $Sm(Co,Cu)_5$ during the low-temperature annealing is independent of microsegregation within the single 1 : 5 structure. In our detailed examination of the effect of annealing temperature, we used non-homogenized $Sm(Co,Cu)_5$ alloys following the pattern of earlier works on the subject [3, 7]. In contrast to $Sm(Co,Cu)_5$, the as-made $SmCo_{2.25}Fe_{0.75}Cu_2$ alloy was non-uniform both chemically and structurally: in addition to the 1 : 5 phase it contained significant amounts of the Fe-enriched 2 : 17 phase and the Cu-enriched 2 : 7 phase. After homogenization of the $SmCo_{2.25}Fe_{0.75}Cu_2$ alloy at 1050°C TEM and XRD showed a chemically uniform 1 : 5 structure, while thermomagnetic analysis revealed a sharp $M(T)$ peak at the Curie temperature of the only magnetic phase. This homogenized $SmCo_{2.25}Fe_{0.75}Cu_2$ alloy was the one subjected to the low-temperature annealing.

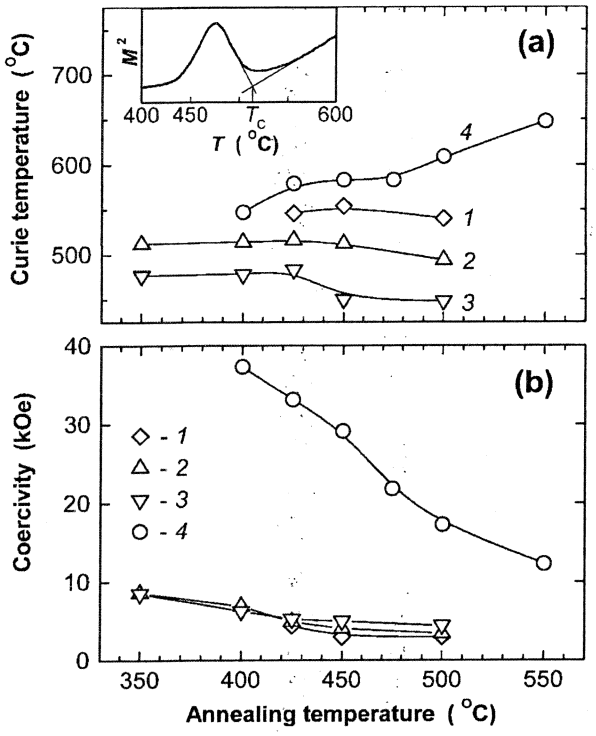

Figure 6. Effect of annealing temperature on (*a*) Curie temperature and (*b*) room-temperature coercivity for (1) $SmCo_4Cu_1$, (2) $SmCo_{3.5}Cu_{1.5}$, (3) $SmCo_3Cu_2$ and (4) $SmCo_{2.25}Fe_{0.75}Cu_2$. The inset shows an example of T_C evaluation ($SmCo_{3.5}Cu_{1.5}$, $T_A = 400°C$).

5. Effect of annealing temperature on the coercivity

Figure 6 shows the Curie temperatures and room-temperature intrinsic coercivities measured for three $SmCo_{5-x}Cu_x$ alloys ($x = 1, 1.5, 2$) and the $SmCo_{2.25}Fe_{0.75}Cu_2$ alloy after annealing treatments at different temperatures, T_A. The effect of T_A on T_C for $Sm(Co,Cu)_5$ alloys is opposite to that for $Sm(Co,Fe,Cu)_5$: in the Fe-free alloys the higher T_A results in a somewhat lower T_C, while in the Fe-added alloy T_C strongly increases with T_A. This difference may arise from the more complex metallurgical behaviour of $Sm(Co,Fe,Cu)_5$, which includes the emergence of the $Sm_2(Co,Fe)_{17}$ phase at higher annealing temperatures. A more detailed report on the structure and magnetic properties of $SmCo_{2.25}Fe_{0.75}Cu_2$ will be the subject of a separate publication; this study focuses on the annealing temperatures around T_C. In this temperature range, the coercivity of all the alloys studied changes significantly with T_A. In particular, H_c of $SmCo_{2.25}Fe_{0.75}Cu_2$ increases from 12.3 to 37.3 kOe when T_A decreases from 550°C to 400°C.

In figure 7, H_c/H_c^* (H_c^* and H_c are, respectively, the room-temperature coercivities before and after annealing) is plotted versus both T_A and the deviation of T_A from T_C. The latter plot seems to reveal a universal behaviour in all samples with the reduced coercivities increasing in a similar way, if annealed at 100–140°C below T_C. This may suggest that the magnetic states of the $Sm(Co,Cu)_5$ and $Sm(Co,Fe,Cu)_5$ influence the structural transformations, particularly those responsible for the increase in H_c. Figure 8 shows parts of the XRD scans for the $SmCo_{5-x}Cu_x$ alloys with $x = 1$, 1.5 and 2 annealed above and below the Curie temperatures. All the scans show

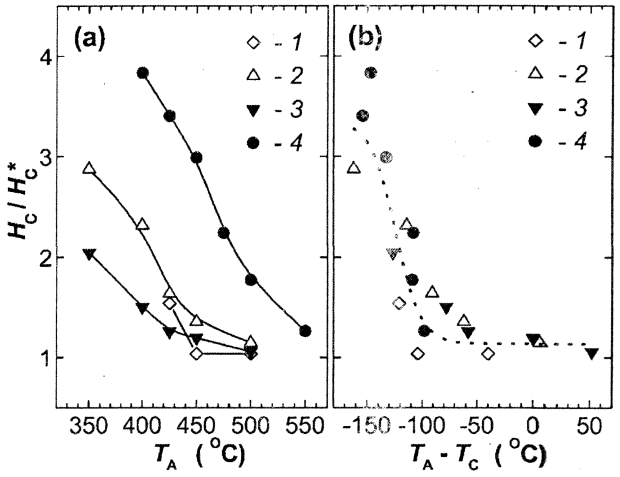

Figure 7. Reduced coercivities of (1) $SmCo_4Cu_1$, (2) $SmCo_{3.5}Cu_{1.5}$, (3) $SmCo_3Cu_2$ and (4) $SmCo_{2.25}Fe_{0.75}Cu_2$ after annealing versus (*a*) annealing temperature T_A and (*b*) deviation of T_A from the Curie temperature T_C. H_c^* is the coercivity before annealing.

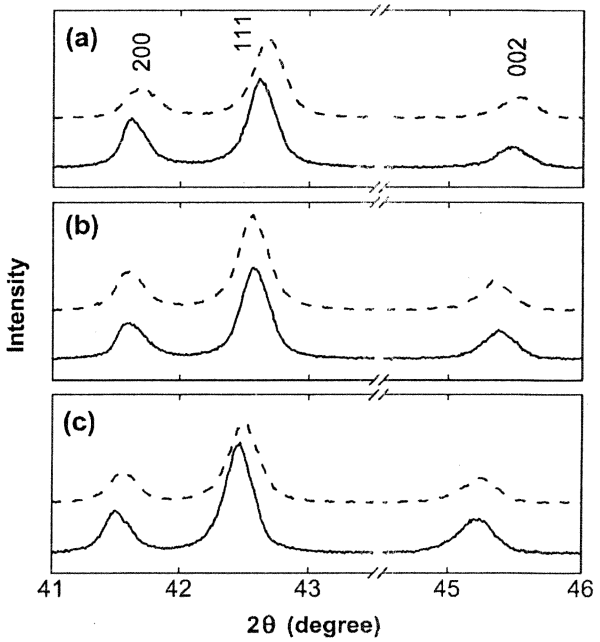

Figure 8. Experimental XRD spectra for (*a*) $SmCo_4Cu_1$, (*b*) $SmCo_{3.5}Cu_{1.5}$ and (*c*) $SmCo_3Cu_2$, annealed at 350°C (——) and at 500°C (- - - -).

what seems to be the uniform $CaCu_5$-type structure with neither a splitting nor broadening of the peaks, which could be associated with a phase separation.

6. Discussion

The electronic structure calculations predict a separation of $SmCo_{5-x}Cu_x$ into the $SmCo_4Cu_1 + SmCo_1Cu_4$ mixture or the $SmCo_5 + SmCu_5$ mixture, for the non-magnetic and magnetic states, respectively. This is consistent with the two-phase structure of the as-made alloys reported in this paper and in a number of earlier works [3, 5, 7]. However, it seems unlikely that such a separation is responsible for the

magnetic hardness of alloys, as was suggested by Mitchell and McCurrie [7]. On the contrary, the magnetic measurements data for $SmCo_3Cu_2$ summarized in figure 5 (and similar data for the other Sm–Co–Cu alloy studied in this work) show that homogenization treatment actually increases the coercivity.

The very low initial susceptibility observed in all thermally demagnetized samples (see, e.g. curves in figure 5(*b*)) indicates that domain walls are not free to move through the grains. This, in particular, rules out the hypothesis by Yamashita [8] that the magnetic hardness is caused by coherent precipitates of pure Co at the $Sm(Co,Cu)_5$ grain boundaries via increase in the magnetocrystalline anisotropy of the edge Sm ions. The initial magnetization curves suggest that the coercivity of the alloys is caused by a uniform domain wall pinning *inside* the $Sm(Co,Cu)_5$ grains.

One possible mechanism generating multiple pinning sites inside a grain is a spinodal decomposition into two $SmCo_{5-x}Cu_x$ phases with different x values, similar to that observed in as-made alloys, but of a submicrometre scale. The fact that we do not see signs of such decomposition with XRD (figure 8) does not necessarily mean that it does not occur during annealing. The phase separation in the as-made alloys was also not seen by XRD. However, the thermomagnetic analysis, which appears to be more sensitive to the phase separation than XRD (as can be seen from a comparison of curves 1 and 3 in figure 5(*a*)), also does not reveal any signs of this transformation. In the energy calculations, which predicted the decomposition, we considered only chemical energy, while in the real alloy the transformation might be suppressed due to positive changes of the elastic strain energy.

The calculations also suggested different preferred site occupancies for the Cu atoms in $SmCo_{5-x}Cu_x$ with $x = 1$, 1.5 and 2. In the magnetic state, Cu should always prefer to occupy the 2*c* sites (figure 2), while in the non-magnetic state, Cu should prefer the 3*g* sites for $x = 1$ and random occupancies for $x = 2$. It is interesting that after annealing at 350°C, the alloys with $x = 1$ and 2 have a lattice parameter a 0.14% larger than that after annealing at 500°C (for $x = 1$ those parameters are the same). It is conceivable that this difference reflects the expansion of the atomic layer, which contains the 2*c* transition-metal sites, when it is preferred by the larger Cu atoms. In the model proposed by Oesterreicher *et al* [2], the magnetic hardness in the single phase $Sm(Co,Cu)_5$ compound was explained by domain wall pinning at the local fluctuations of the exchange energy due to weakly coupled Co atoms. If this is the case, the supposed reordering of the Cu and Co atoms upon annealing below the Curie temperature may be responsible for the observed increase in the room-temperature coercivity.

7. Summary

(1) According to our first principle density functional calculations, the $RCo_{5-x}Cu_x$ compounds with R = Y, Sm are unstable against decomposition into two phases of the same structure with different x values. The calculations also suggest that the magnetic state of the alloys affects the stable x values and the Cu atomic site preferences.

(2) SEM and thermomagnetic studies confirm the two-phase structure of the as-made $Sm(Co,Cu)_5$ alloys. The high-temperature homogenization eliminates the chemical microsegregation and slightly increases the coercivity of the alloys.

(3) A more significant increase in the coercivity (in both the as-made and homogenized alloys) can be achieved by low-temperature annealing. The low initial susceptibility observed in all the samples studied implies that the coercivity is always caused by a uniform domain wall pinning inside the $Sm(Co,Cu)_5$ grains.

(4) The coercivity of different $Sm(Co,Cu)_5$ and $Sm(Co,Fe,Cu)_5$ alloys increases significantly if annealed 100–140°C below their Curie temperature. Of the two theoretically predicted effects of the alloy magnetic state on the alloy structure—phase separation and change in preferred atomic site occupancies—the latter seems to be more consistent with the results of XRD and especially thermomagnetic studies.

Acknowledgments

This work was supported by the Defense Advanced Research Projects Agency (DARPA). We wish to thank D A Papaconstantopoulos for encouragement and many interesting discussions.

References

[1] Nesbitt E A, Willens R H, Sherwood R C, Buehler E and Wernick J H 1968 *Appl. Phys. Lett.* **12** 361
[2] Oesterreicher H, Parker F T and Misroch M 1979 *J. Appl. Phys.* **50** 4273
[3] Hofer F 1970 *IEEE Trans. Magn.* **6** 221
[4] Kamino K, Kimura Y, Suzuki T and Itayama Y 1973 *Trans. JIM* **14** 135
[5] Katayama T and Shibata T 1973 *Japan. J. Appl. Phys.* **12** 319
[6] Glardon R and Kurz W 1979 *Z. Metallk.* **70** 386
Stadelmaier H H, Reinsch B and Petzow G 1998 *Z. Metallk.* **89** 114
[7] Mitchell R K and McCurrie R A 1986 *J. Appl. Phys.* **59** 4113
[8] Yamashita O 2004 *J. Phys. Chem. Solids* **65** 907
[9] Katter M 1998 *J. Appl. Phys.* **83** 6721
Streibl B, Fidler J and Schrefl T 2000 *J. Appl. Phys.* **87** 4765
Kronmüller H and Goll D 2002 *Scr. Mater.* **47** 545
[10] Popov A G, Gaviko V S, Magat L M and Ivanova G V 1990 *Phys. Met. Metallogr.* **69** 100
Gabay A M, Tang W, Zhang Y and Hadjipanayis G C 2001 *Appl. Phys. Lett.* **78** 1595
Yan A, Gutfleisch O, Handstein A, Gemming T and Müller K-H 2003 *J. Appl. Phys.* **93** 7975
[11] Singh D J 1994 *Planewaves, Pseudopotentials, and the LAPW Method* (Boston, MA: Kluwer)
[12] Blaha P, Schwar K, Madsen G K H, Kvansicka K and Luitz J 2001 WIEN2k, an augmented plane wave + local orbitals program for calculating crystal properties *Techn. Universitat Wien* ISBN 3-9501031-1-2
[13] Anderson O K, Madsen J, Poulsen U K, Jepsen O and Kollar J 1977 *Physica* B&C **86** 249
[14] Anderson O K 1994 Tight-Binding LMTO Vers. 4.7, Max-Planck-Institut fur Festkoperforschung
[15] Larson P and Mazin I I 2003 *J. Magn. Magn. Mater.* **93** 6888
Larson P, Mazin I I and Papaconstantopoulos D A 2003 *Phys. Rev.* B **67** 214405
[16] Uebayashi K, Terao K and Yamada H 2002 *J. Alloys Compounds* **346** 47

Enhanced M_r and $(BH)_{max}$ in anisotropic $R_2Fe_{14}B/\alpha$-Fe composite magnets via intergranular magnetostatic coupling

A. M. Gabay, M. Marinescu,[a] and G. C. Hadjipanayis
Department of Physics and Astronomy, University of Delaware, Newark, Delaware 19716

(Presented on 31 October 2005; published online 18 April 2006)

Composite magnets were prepared by hot pressing followed by hot deformation of blends composed of $Nd_{14}Fe_{79.5}Ga_{0.5}B_6$ or $(Nd_{0.75}Dy_{0.25})_{14}Fe_{79.5}Ga_{0.5}B_6$ ribbon powders as a high-coercivity component and Fe powder as a high-magnetization component. The addition of 15 wt % α-Fe to $(Nd_{0.75}Dy_{0.25})_{14}Fe_{79.5}Ga_{0.5}B_6$ increases the remanent magnetization of the hot-deformed magnets from 10.6 to 12.04 kG, while the maximum energy product is also increased from 27.3 to 29.5 MG Oe for hot-deformed magnets with 10 wt % α-Fe addition. Microstructure investigations of the composite magnets revealed the size of the Fe particles in the micrometer range, exceeding by far the size for effective exchange interactions. Despite a less refined microstructure, the particular layered configuration of the composite magnets gives rise to a positive magnetostatic coupling of the grains and therefore a unitary magnetic behavior with enhanced magnetic properties. The cooperative demagnetization process, together with the magnetic coupling of the grains, was pointed out through a smooth demagnetization curve and a sharp single peak of the irreversible susceptibility. © *2006 American Institute of Physics*. [DOI: 10.1063/1.2162818]

I. INTRODUCTION

The search for stronger permanent magnets is the subject of current worldwide efforts because of the continuous demand for the miniaturization of electrical devices and for more powerful electrically driven engines. For the past few years, the research for the development of advanced permanent magnets has been focused on anisotropic nanocomposite materials which, according to theoretical models, have the potential to become about two times stronger than the currently existing magnets and possibly reach the maximum energy product $(BH)_{max}$=100 or 120 MG Oe at room temperature.[1,2] These nanocomposite magnets consisting of one magnetically hard component with high uniaxial magnetocrystalline anisotropy (the most commonly $R_2Fe_{14}B$ compound, where R is rare earth) and one magnetically soft component with high saturation magnetization (most commonly Fe based) take advantage of the outstanding specific magnetic parameters of each phase. The belief so far was that this composite magnetic system, as a whole, behaves unitarily and has an enhanced remanence higher than the weighted average values of the component phases only when the component hard and soft phases are coupled through intergranular magnetic exchange interactions. Because exchange interaction has a short range, the magnetic hardening of the soft component requires the grain size of the soft magnetic phase to be twice the domain-wall width of the hard phase, which is about 8 nm for the $Nd_2Fe_{14}B$ phase. However, our latest studies[3] showed that an increased $(BH)_{max}$ can be obtained in bulk composite magnets with grain size larger than 200 nm, suggesting that the coupling effect may be due to magnetostatic interactions and not exchange.

In this work, we present our latest results on anisotropic composite magnets prepared from blends of high-coercivity rare-earth-rich melt-spun ribbon powders and relatively coarse Fe powder.

II. EXPERIMENT

The precursor components for the composite magnets used in the present study are $Nd_{14}Fe_{79.5}Ga_{0.5}B_6$ and $(Nd_{0.75}Dy_{0.25})_{14}Fe_{79.5}Ga_{0.5}B_6$ as a high-coercivity component and Fe powder as a high-magnetization component. The alloys were prepared from pure components by arc melting and then subjected to melt spinning at the wheel speed of 26 m/s. The melt-spun ribbons were crushed with a hand mortar. The Fe powder from CERAC Inc. had the particle size $\leqslant$44 μm. The crushed Nd–Fe–B ribbons and Fe powder were thoroughly mixed. The blends were named based on the weight ratio of the components, e.g., $0.85[(Nd_{0.75}Dy_{0.25})_{14}Fe_{79.5}Ga_{0.5}B_6]/0.15Fe$. The powder blends were pressed under up to 3 metric tons and then heated under vacuum up to 780–810 °C. For hot plastic deformation, the previously hot-pressed samples were heated again at 900 °C and then upset by 65%–70% of their original height at the strain rate of 0.008 s^{-1}.

The microstructure of the hot-pressed and hot-deformed magnets was studied with scanning electron microscopy (SEM) with a JEOL JSM-6330F instrument. The specimens for the microscopic studies were cut parallel to the pressure direction. The demagnetization curves were measured parallel to the pressure direction for rectangular specimens magnetized by a dc field of 50 kOe with both the vibrating-sample magnetometer and Quantum Design MPMS magnetometer. The $4\pi M(H)$ curves were corrected using demagnetization factors from Ref. 4. In order to evaluate the interphase magnetic coupling effect, irreversible susceptibility measurements have been employed.

[a]Electronic mail: mmarinescu@physics.udel.edu

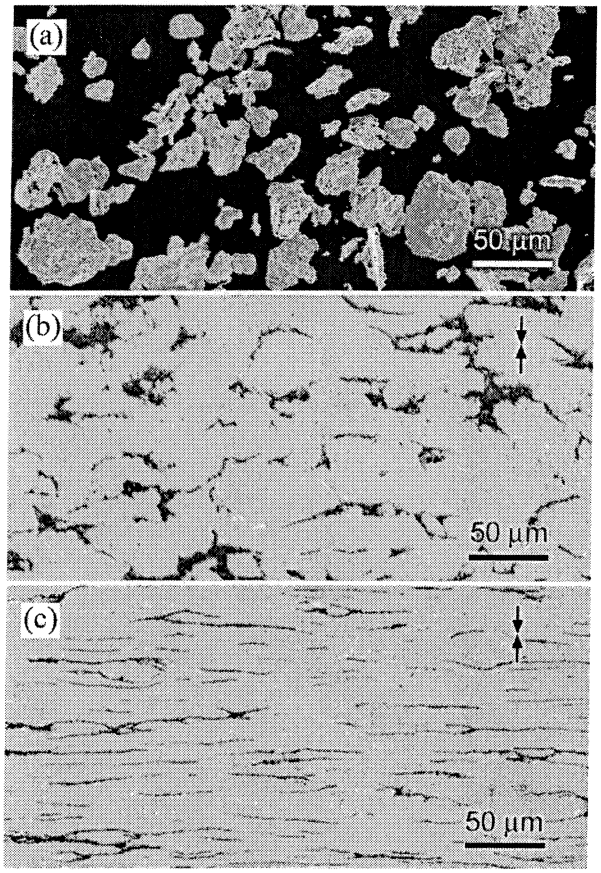

FIG. 1. (a) SEM image of Fe powder and SEM backscattered electron images of (b) hot-pressed and (c) hot-deformed $0.85[(Nd_{0.75}Dy_{0.25})_{14}Fe_{79.5}Ga_{0.5}B_6]/0.15Fe$ magnets. The arrows indicate the pressure direction.

III. RESULTS AND DISCUSSION

Figure 1 presents the SEM micrographs of the initial Fe powder and of the hot-pressed and hot-deformed $0.85[(Nd_{0.75}Dy_{0.25})_{14}Fe_{79.5}Ga_{0.5}B_6]/0.15Fe$ composites. The initial Fe powder particles are irregular with an average size of about 30 μm. After hot pressing [Fig. 1(b)] many Fe particles preserve the size and shape of the starting particles, though some of them become thin platelets oriented perpendicular to the pressure direction. Because the particles in the two starting powders, $(Nd_{0.75}Dy_{0.25})_{14}Fe_{79.5}Ga_{0.5}B_6$ and Fe, had an average size of the same order of magnitude, the particles did not agglomerate (as it usually happens when compacting blends of micron-sized magnetically hard powders and Fe nanopowders[5]). After deformation [Fig. 1(c)], all the Fe particles become thin platelets oriented perpendicular to the pressure direction. The smallest thickness of the α-Fe platelet that we observed was about 1 μm.

Hot deformation may be accompanied by a diffusion across the interface between the blended components.[6] To evaluate this effect we measured the magnetization curves of the hot-deformed magnets at 400 °C. At this temperature, the saturation magnetization of α-Fe is 191 emu/g (Ref. 7) while the 2:14:1 phase becomes paramagnetic. By subtracting the paramagnetic component from the values of the magnetization, we were able to evaluate the amount of the α-Fe phase. We have obtained that the hot-deformed magnets actually contained 3–4 wt % less α-Fe than the corresponding starting blends.

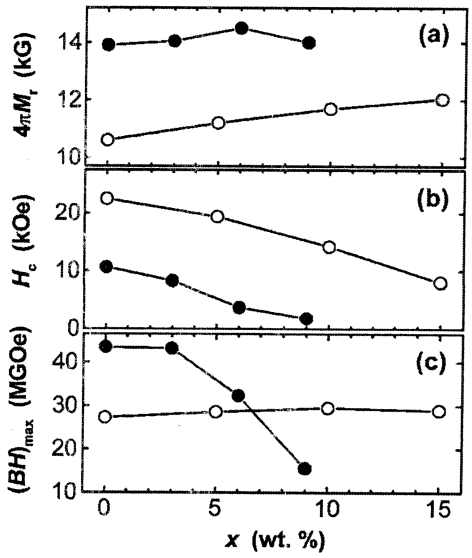

FIG. 2. (a) Remanence, (b) intrinsic coercivity, and (c) maximum energy product for $(1-x)[Nd_{14}Fe_{79.5}Ga_{0.5}B_6]/xFe$ magnets (solid circles) and $(1-x)[(Nd_{0.75}Dy_{0.25})_{14}Fe_{79.5}Ga_{0.5}B_6]/xFe$ magnets (open circles).

Figure 2 shows the variation of the remanence, coercivity, and maximum energy product for the $(1-x)[Nd_{14}Fe_{79.5}Ga_{0.5}B_6]/xFe$ and $(1-x)\times[(Nd_{0.75}Dy_{0.25})_{14}Fe_{79.5}Ga_{0.5}B_6]/xFe$ series of blends upon hot deformation at 900 °C. We observed an increase of remanence with x for both series. In the $(1-x)\times[(Nd_{0.75}Dy_{0.25})_{14}Fe_{79.5}Ga_{0.5}B_6]/xFe$ magnets, the addition of 15 wt % α-Fe to the starting blend increases $4\pi M_r$ from 10.6 to 12.04 kG, i.e., by 13.6%. The $(BH)_{max}$ is also increased from 27.3 to 29.5 MG Oe for $x=0.10$. One $0.90[(Nd_{0.75}Dy_{0.25})_{14}Fe_{79.5}Ga_{0.5}B_6]/0.10Fe$ exceptional specimen showed even a 23% increase in maximum energy product to 33.5 MG Oe. Typical demagnetization curves for the $(1-x)[(Nd_{0.75}Dy_{0.25})_{14}Fe_{79.5}Ga_{0.5}B_6]/xFe$ composite magnets are shown in Fig. 3. The nonconstricted profile of the demagnetization curves for $x=0.05-0.15$ demonstrates that the components of the composite magnets behave in a

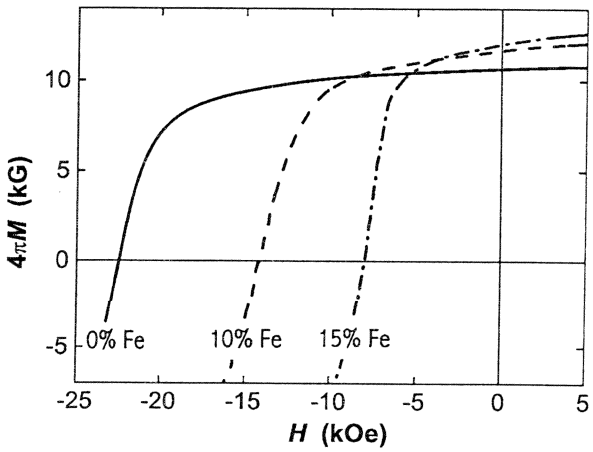

FIG. 3. Room-temperature demagnetization curves for $(Nd_{0.75}Dy_{0.25})_{14}Fe_{79.5}Ga_{0.5}B_6/Fe$ hot-deformed magnets.

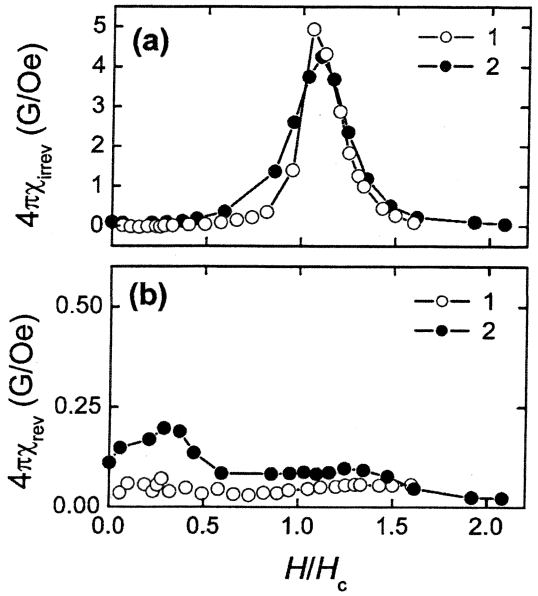

FIG. 4. Magnetic susceptibility measurements in (1) $(Nd_{0.75}Dy_{0.25})_{14}Fe_{79.5}Ga_{0.5}B_6$ (open circles) and (2) $0.90[(Nd_{0.75}Dy_{0.25})_{14}Fe_{79.5}Ga_{0.5}B_6]/0.10$ Fe (solid circles) hot-deformed magnets.

cooperative way. The intergranular exchange coupling is unlikely to be the reason for this behavior. We strongly believe that it is the magnetostatic interaction responsible for the magnetic coupling. The microstructure with the magnetically soft layers arranged perpendicularly to the direction of magnetization should favor their magnetostatic coupling with the hard magnetic matrix. The magnetic coupling of the grains within the $0.90[(Nd_{0.75}Dy_{0.25})_{14}Fe_{79.5}Ga_{0.5}B_6]/0.10$Fe hot-deformed magnets, leading to a cooperative demagnetization process along the direction of the applied pressure during hot deformation, was pointed out through the susceptibility measurements as a function of the reduced field H/H_c, where H_c is the intrinsic coercivity (Fig. 4). The irreversible susceptibility χ_{irrev} was calculated as the difference between the total susceptibility (derived from the major hysteresis loop) and its reversible component χ_{rev} (calculated as the slope of the recoil curves in the vicinity of the initial point on the major hysteresis loop). As revealed in Fig. 4, the χ_{irrev} for the specimen containing Fe powder presents a well-defined peak as a function of the magnetic field. The χ_{rev} of this specimen exhibits a peak at the low demagnetizing field, similarly to the exchange-coupled magnets containing a soft magnetic phase.[8]

The magnetostatic interactions are notoriously damaging for the coercivity. In order to compare the coercivity losses for different series of composite magnets, we plot in Fig. 5 the normalized coercivity $h_c=H_c(x)/H_c(0)$, where $H_c(x)$ and $H_c(0)$ are the coercivities of magnets with and without addition of Fe as a function of the measured α-Fe content. The coercivity loss is more rapid when the Fe powder is added to $Nd_{14}Fe_{79.5}Ga_{0.5}B_6$ powder which has the lower H_c. One can conclude thus that the coercivity of the hard magnetic component is among the most important factors controlling the performance of magnetostatically coupled composite magnets. This result could have been expected since in the magnetostatically coupled composite magnets, the coercivity of the hard phase must withstand not only the self-demagnetizing field of the hard phase but also the stray fields generated by the soft magnetic phase.

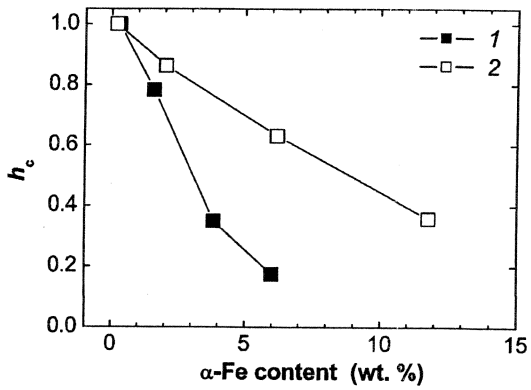

FIG. 5. Reduced coercivity of hot-deformed magnets as a function of the actual content of the α-Fe phase: (1) $(1-x)[Nd_{14}Fe_{79.5}Ga_{0.5}B_6]/x$Fe magnets and (2) $(1-x)[(Nd_{0.75}Dy_{0.25})_{14}Fe_{79.5}Ga_{0.5}B_6]/x$Fe magnets.

IV. CONCLUSION

Composite magnets obtained by hot compaction followed by hot deformation of blends consisting of a high-coercivity rare-earth-rich R–Fe–B powder and coarse Fe powder may present an enhanced M_r and improved $(BH)_{max}$ compared to the corresponding magnets without the Fe addition. An increase of M_r by 13.6% was obtained with the addition of 15 wt % α-Fe whereas $(BH)_{max}$ increased from 27.3 to 29.5 MG Oe for a 10 wt % addition of α-Fe. Microstructure investigations revealed the size of the Fe particles in the micrometer range, exceeding by far the size for effective exchange interactions. Despite a less refined microstructure, the particular layered configuration of the composite magnets gives rise to a positive magnetostatic coupling of the grains and therefore a unitary magnetic behavior with enhanced magnetic properties.

ACKNOWLEDGMENTS

This work was supported by the Department of Energy (DOE) and Defense Advanced Research Projects Agency (DARPA).

[1]E. F. Kneller and R. Hawig, IEEE Trans. Magn. **27**, 3588 (1991).
[2]R. Skomski and J. M. D. Coey, Phys. Rev. B **48**, 15812 (1993).
[3]A. M. Gabay, Y. Zhang, and G. C. Hadjipanayis, Appl. Phys. Lett. **85**, 446 (2004).
[4]P. V. Sharma, Geophysics **33**, 132 (1968).
[5]Q. Zeng, Y. Zhang, M. J. Bonder, G. C. Hadjipanayis, and R. Radhakrishnan, IEEE Trans. Magn. **39**, 2974 (2003).
[6]C. D. Fuerst and E. G. Brewer, J. Appl. Phys. **76**, 6232 (1994).
[7]*American Institute of Physics Handbook* (McGraw-Hill, New York, 1972), pp. 5–145.
[8]P. G. McCormick, J. Ding, E. H. Feutrill, and R. Street, J. Magn. Magn. Mater. **157/158**, 7 (1999).

Submicrometer Laminated Fe/SiO_2 Soft Magnetic Composites—An Effective Route to Materials for High-Frequency Applications**

By *Yuwen Zhao,* Xiaokai Zhang,* and *John Q. Xiao**

With the ever-increasing rotational speed of motors and generators and further demands for miniaturization in power transformers, inductors, and direct current/direct current (DC/DC) convertors,[1,2] magnetic-core materials with low energy losses and high flux densities, permeabilities, and operating frequencies[3–7] are in high demand. It is well known that as the operating frequency (f) increases, the eddy-current loss ($W_e \propto f^2$) increases much more rapidly than the hysteresis loss ($W_e \propto f$) such that the total core energy loss is dominated by W_e at about $f > 100$ kHz.[8] Eddy current not only deteriorates the overall magnetic properties, but also generates tremendous heat through the Joule effect, resulting in difficulties in the design and engineering of the devices. To mitigate the energy loss associated with eddy current, it is essential to eliminate the electrical conducting path or significantly increase the resistivity of the materials. For applications at frequencies below 1 kHz, laminated silicon steels which also have high magnetic-flux densities are typically used. But, the eddy-current loss can still be significant due to high-frequency components produced by pulse-width modulations in typical alternating-current (AC) drives. Further reducing the thickness of the silicon steel sheet becomes either technically impractical or very costly, limiting the use of laminated cores for higher-frequency applications. At the medium frequency range (1 kHz to 1 MHz), insulated iron-powder cores achieved by consolidating Fe powders coated with polymers or other insulating materials can be used. In addition, Fe-based amorphous alloys[9,10] also possess good magnetic and frequency properties. However, the poor mechanical properties of Fe-based amorphous alloys limit their applications.[11] Soft ferrites can also be used at this frequency; however, their low magnetic-flux densities (smaller than 0.5 T) are undesirable. As the frequency approaches the 100 MHz to 1 GHz range, many soft magnetic materials show ferromagnetic resonant behaviors that limit the operating frequency. In this communication, we report a novel and simple method to fabricate soft magnetic Fe/SiO_2 composites that have laminated structures with lateral dimensions of a few to several hundred micrometers and a submicrometer thickness. The composites show frequency-independent permeability spectra up to about 50 MHz—that is, about two orders of magnitude higher than the parent Fe-based powders.

The starting material is sponge-like or quasi-spherical agglomerated polymer-coated Fe powder (Hoeganaes Inc., TC-80) with an average particle size of ~150 μm (Fig. 1a). The consolidated samples have good frequency performance up to about 100 kHz because of the insulating treatment with about 0.75 % polymer and phosphate.[12] The quoted initial permeability is 80, and coercive force is about 4.7 Oe (1 Oe = 79.58 A m^{-1}). X-ray diffraction (XRD) data indicate a body-centered cubic (bcc) Fe structure (Fig. 2a). Bulk samples compacted from the original powders under static pressure of about 1.1 GPa without thermal treatment and without addition of lubricant have also shown a flat permeability spectrum up to about 100 kHz but with values of about 50, as shown in Figure 3 (curve 1). The lower permeability is attributed to a lower compaction density of about 65 % ideal density (7.2 g cm^{-3}) achieved under our compaction conditions.

We have discovered that, by deforming these polymer-coated Fe powders in a well-controlled manner, we can produce Fe thin sheets with lateral dimension of the order of a hundred micrometers and with submicrometer thicknesses, as shown in Figure 1b. (Hereafter, we will refer to these sheets as submicrometer laminates.) We have also found that it is not possible to produce Fe submicrometer laminates using Fe powder without the polymer coating. The polymer coating (consisting of thermoplastic resins, such as polyphenylene ether or polyetherimide)[13,14] behaves as an inhibitor for cold-welding between the squeezed Fe particles during the deformation process. This seemingly simple process provides an effective method to create submicrometer laminates, which may find many applications.

The controlled-deformation process produces more-textured crystalline structures in submicrometer laminates, as evidenced by the more pronounced (200) diffraction peak in Figure 2b. This texture is further enhanced after compaction (Fig. 2c). It is known that in silicon steel, the [001] direction is preferred along the cold-rolling direction,[15] and the [011] direction is perpendicular to the sheets. The mechanical deformation (see Experimental section) in our experiments induces the strain in the sheet plane. Deformation along the strain direction, [001], is preferred for the laminates, similar to the cold-rolling case. This implies a (100) texture in the sheet plane, as observed experimentally.

The permeability spectrum of the consolidated parent Fe/polymer powders is shown in Figure 3a (curve 1). The permeability decreases rapidly above 200 kHz due to the induced eddy current inside each 150 μm particle. To confirm this conclusion, we coated the Fe/polymer powders with a SiO_2 layer and measured the permeability of the consolidated Fe/polymer/SiO_2 powder (curve 2 in Fig. 3a). Its permeability spectrum shows the same trend, and the quality-factor curves almost overlap each other (curves 1,2 in Fig. 3b), indicating

[*] Dr. Y.-W. Zhao, Prof. J. Q. Xiao, X. K. Zhang
Department of Physics and Astronomy, University of Delaware
Newark, DE 19716 (USA)
E-mail: ywzhao@udel.edu; jqx@udel.edu

[**] The authors are grateful to P. Gerald for his assistance in SEM studies. This work is supported by the US Defense Advanced Research Program Agency (DARPA) through the Air Force Research Laboratory under Grant No. F33615-01-2-2166, AFOSR F49620-03-1-0351, and ARO DEPSCOR MAGNET W911NF-04-1-0264.

DOI: 10.1002/adma.200401096

ADVANCED MATERIALS

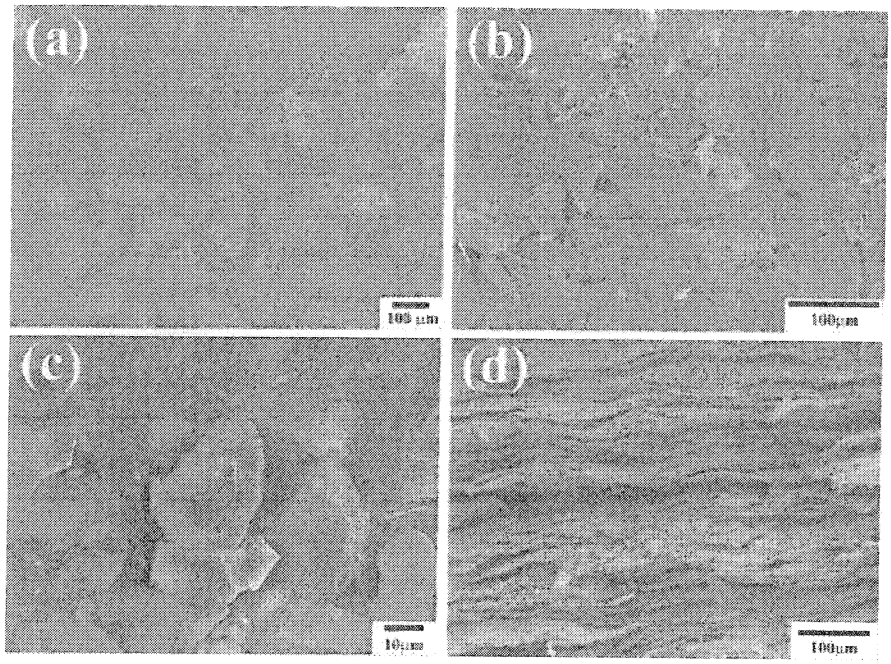

Figure 1. Scanning electron microscopy (SEM) images of a) original Fe-based powders; powders b) after controlled mechanical deformation and c) after subsequent coating with amorphous silica; d) cross-section of compacted sample.

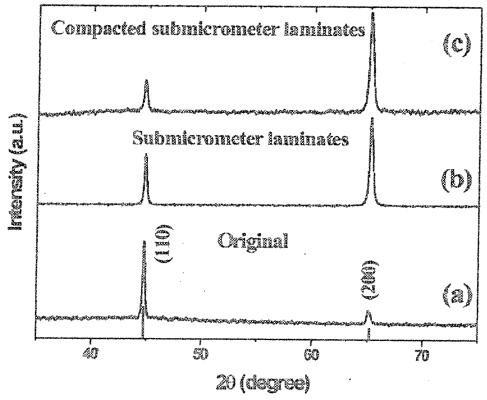

Figure 2. XRD graphs of a) original Fe-based powders, b) Fe submicrometer laminates, and c) subsequently compacted submicrometer laminates. Vertical bars indicate bcc Fe peak positions from Joint Committee on Powder Diffraction Standards (JCPDS) Card No. 87-0722.

that the large particle size and the resistivity of the particles dictate the frequency dependence of the permeability. During the mechanical deformation to achieve submicrometer laminates, the original polymer and the phosphate insulating coating are partially destroyed and partially redistributed. Consolidating these Fe sheets results in electrically conductive bulk samples. Interestingly, the permeability shows similar frequency behavior with the parent compound (curve 3 in Fig. 3a), indicating that the eddy current is still suppressed below 100 kHz due to the residual insulating polymer and newly formed oxide layer. The slightly lower permeability is due to the deterioration of the magnetic properties after the mechanical work. The coercive force H_c increased from 5.8 to 16.6 Oe and magnetization at 1 T (M_{1T}) decreased from 206 to 186 emu g^{-1}. This is understandable because of the oxidation and mechanical strain. Although increased coercive force will increase hysteresis loss (W_h), W_e dominates in the high frequency regime as shown by[8]

$$W = W_h + W_e = k_1 Af + \frac{k_2 B^2 t^2}{\rho} f^2 \quad (1)$$

where k_1 and k_2 are constants, B is the magnetic flux density, A is the area of the DC-hysteresis loop, ρ is the resistivity, t is the sample thickness, and f is the frequency.

To improve the frequency responses, we coated the Fe submicrometer laminates with SiO_2 using a base-catalyzed sol–gel method. As expected, magnetization M_{1T} decreased slightly from 186 to 172 emu g^{-1}, and the coercivity remained unchanged. The permeability spectrum (curve 4 in Fig. 3a) shows an almost two orders of magnitude improvement in terms of operating frequency over the parent compounds and uncoated submicrometer laminates. It indicates that the eddy current has been effectively suppressed between the submicrometer laminates and inside each laminate. The eddy currents inside each laminate are governed by the laminate thickness t and the skin depth δ, defined as[15,16,17]

$$\delta = \frac{1}{\sqrt{\pi \mu_r \mu_0 f / \rho}} \quad (1)$$

where μ_r is the relative permeability of the material and μ_0 is the vacuum permeability. Assuming $\rho = 10$ μΩ cm and $\mu = 300$ for Fe, we estimate $\delta = 9.2$ μm and 1.3 μm at $f = 1$ MHz and 50 MHz, respectively. These values are much lower than the thicknesses of conventional silicon steel laminates (several tens to hundreds of micrometers), but are much larger than or approaching the thicknesses of our laminates at 1 MHz and 50 MHz. Therefore, we expect to see strong eddy-current effects above 50 MHz, which is nicely demonstrated in our experimental results (curve 4 of Fig. 3a).

It is equally obvious that the volume of the non-magnetic materials should be minimized as long as they can provide sufficient electrical insulation. We have recently reported[7] that by coating 100 nm FeNi particles with thin layers (~3 nm) of

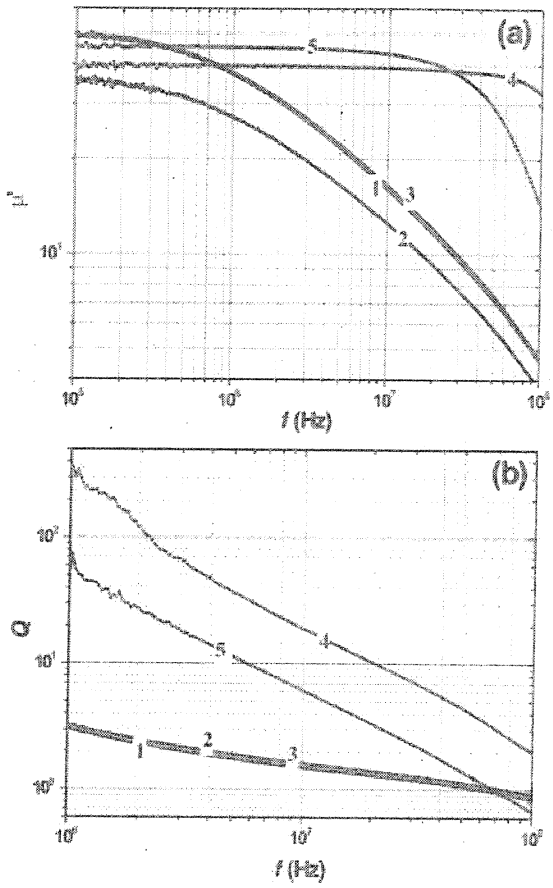

Figure 3. a) Real part of permeability (μ') and b) quality factors (Q) versus frequency (f) for consolidated samples made of original powders (curve 1), original powders coated with silica (curve 2), submicrometer laminates without coating (curve 3), silica-coated submicrometer laminates (curve 4), and laminates subsequently annealed at 500 °C under Ar atmosphere for 5 h (curve 5).

amorphous silica, flat permeability spectra can be obtained up to at least 100 MHz. In this regard, the coating thickness in the current experiment is less than 3 nm. The laminated structure was not affected during this soft wet-chemistry coating process, as evidenced in Figure 1c.

A significant improvement in the quality factors ($Q = \mu'/\mu''$, where μ' and μ'' are the real and imaginary components of the permeability) has also been observed (Fig. 3b), resulting from eddy-current suppression in submicrometer laminated Fe cores. The μ' values are lower than for those made of the original powders because of strain accumulated during the mechanical deformation and silica coating. Post-thermal annealing under an Ar atmosphere can release the strain to a certain extent and thus increase the μ' value, but this slightly deteriorates the frequency performance (curve 5 in Fig. 3a). Interestingly, the sample became conductive after the thermal treatment. One plausible cause for this is that the Fe fuses through some pores associated with the silica-coating layer, which usually has a porous structure. Another possible reason is the formation of Fe silicate. The induced conduction is unlikely due to polymer burn-out, since we observed similar behaviors in other SiO_2-coated Fe-containing materials which do not have polymer coatings.

To further explore the energy-loss mechanisms, we have studied the energy loss per cycle ($P = W/f$) versus frequency at induction levels of 100 G (Fig. 4a). The two curves show nearly linear behaviors, indicating the hysteresis and eddy-current losses are major loss mechanisms[18] for cores made of both original polymer-coated Fe powders and silica-coated Fe submicrometer laminates.

From Figure 4a, it can be seen that the slope of the linear fit for silica-coated submicrometer laminates is much smaller than the original powder core, indicating much smaller eddy-current core loss. Due to instrument limitations, we were not able to extend this measurement to MHz frequencies at higher induction levels. However, from the DC-hysteresis data (Fig. 4b), we can see that submicrometer laminates also have

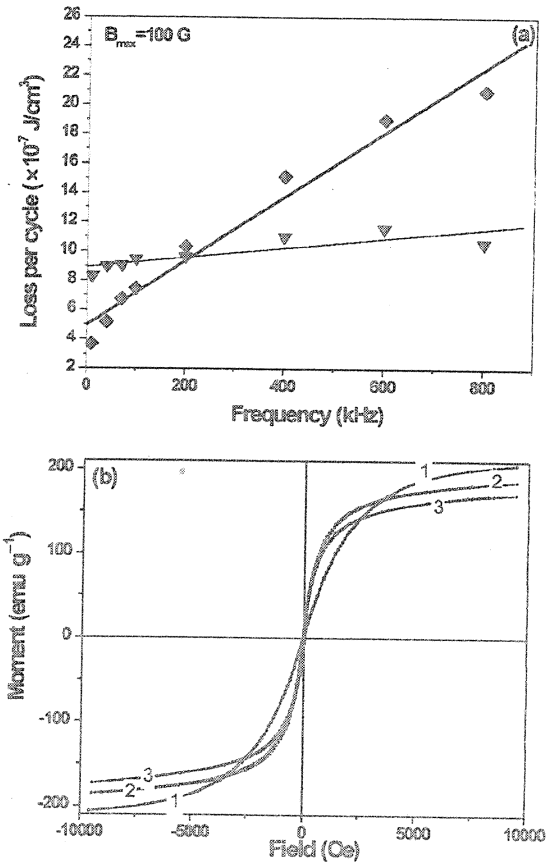

Figure 4. a) Energy loss per cycle versus frequency measured at an induction (B_{max}) level of 100 G with linear fittings for cores made of original powders (diamonds and thick line) and for silica-coated submicrometer laminates (triangles and thin line). b) DC-hysteresis loops for original powders (curve 1), submicrometer laminates (curve 2), and silica-coated submicrometer laminates (curve 3).

ADVANCED MATERIALS

very high saturation fields, similar to the parent powders. This implies that these submicrometer laminated cores can be used in high-power applications where excitation fields are large.

In conclusion, we have successfully fabricated Fe/SiO_2 submicrometer laminates that have lateral dimensions of a few to several hundred micrometers and submicrometer thicknesses. The sheet structure is retained during the consolidation, giving rise to laminated soft Fe cores. High-frequency measurements show that the maximum operating frequency can be increased to about 50 MHz, a more than two orders of magnitude improvement over the parent commercial powders. We ascribe these observations to the combination of submicrometer-scale lamination and the silica coating which effectively prevents eddy-current power loss at high frequencies.

Experimental

Sample Fabrication: Fe thin sheets were produced by mechanically deforming polymer-coated Fe powders (TC80, Hoeganaes, Inc). After deformation, 10 g Fe thin sheets were dispersed into 200 ml 2-propanol and sonicated for 10 min. 40 mL tetraethoxysilane and 20 mL of a 25 vol.-% NH_3 in H_2O solution were added to the above dispersion, and the mixture was vigorously stirred for 1 h to complete the hydrolysis reaction. By means of magnetic decantation, the silica-coated Fe laminates were separated from the supernatant solution. The coated powders were washed twice with 100 mL ethanol and then once with 100 mL acetone to remove any unreacted organic chemicals, and were finally dried in a desiccator.

Compaction: The original Fe powders and silica-coated Fe laminate powders were compacted into toroid samples under static pressure of about 1.1 GPa without addition of any lubricant.

Characterization: The crystalline structures and morphologies were characterized using a Philips 3100 X-pert X-ray diffractometer and a JEOL JSM-6335F scanning electron microscope. Direct-current magnetic properties were measured using a Vibrating Sample Magnetometer (Lakeshore, Inc.). High-frequency magnetic properties were characterized using a HP 4294A Precision Impedance Analyzer with 16454A magnetic test fixtures (Agilent Technologies) and an AMH-401A hysteresis-loop tracer (Walker Scientific Inc.).

Received: July 9, 2004
Final version: October 20, 2004

[1] a) R. F. Krause, J. H. Bularzik, H. R. Kokal, *J. Mater. Eng. Perform.* **1997**, *6*, 710. b) M. Yamaguchi, Y. Miyazawa, K. Kaminishi, H. Kikuchi, S. Yabukami, K. I. Arai, T. Suzuki, *J. Magn. Magn. Mater.* **2004**, *268*, 170. c) Y. Hayakawa, A. Makino, H. Fujimori, H. A. Inoue, *J. Appl. Phys.* **1997**, *81*, 3747.

[2] M. E. McHenry, M. A. Willard, H. Iwanabe, R. A. Sutton, Z. Turgut, A. Hsiao, D. E. Laughlin, *Bull. Mater. Sci.* **1999**, *22*, 495.

[3] T. Kasagi, T. Tsutaoka, K. Hatakeyama, *IEEE Trans. Magn.* **1999**, *35*, 3424.

[4] J. Moulin, Y. Champion, L. K. Varga, J. M. Greneche, F. Mazaleyrat, *IEEE Trans. Magn.* **2002**, *38*, 3015.

[5] T. Zhao, Q. F. Xiao, Z. D. Zhang, M. Dahlgren, R. Grossinger, K. H. J. Buschow, F. R. de Boer, *Appl. Phys. Lett.* **1999**, *75*, 2298.

[6] Y. W. Zhao, T. Zhang, J. Q. Xiao, *J. Appl. Phys.* **2003**, *93*, 8014.

[7] Y. W. Zhao, C. Y. Ni, D. Kruczynski, X. K. Zhang, J. Q. Xiao, *J. Phys. Chem. B* **2004**, *108*, 3691.

[8] J. R. Brauer, Z. J. Cendes, B. C. Beihoff, K. P. Phillips, *IEEE Trans. Ind. Appl.* **2000**, *36*, 1132.

[9] A. Inoue, H. Koshiba, T. Itoi, A. Makino, *Appl. Phys. Lett.* **1998**, *73*, 744.

[10] T. Itoi, A. Inoue, *Appl. Phys. Lett.* **1999**, *74*, 2510.

[11] M. Komatsubara, K. Sadahiro, O. Kondo, T. Takamiya, A. Honda, *J. Magn. Magn. Mater.* **2002**, *242*, 212.

[12] F. G. Hanejko, H. G. Rutz, G. W. Ellis, in *Proc. of the 1997 Int. Conf. on Powder Metallurgy and Particulate Materials*, Metal Powder Industries Federation, Princeton, NJ 1997.

[13] H. G. Rutz, C. Oliver, F. G. Hanejko, B. Quin, *US Patent 5 268 140*, **1993**.

[14] M. Nillius, P. Jansson, *US Patent 6 485 579*, **2002**.

[15] R. M. Bozorth, *Ferromagnetism*, IEEE, New York **1978**.

[16] G. Bertotti, *Hysteresis in Magnetism, for Physicists, Materials Scientists, and Engineers*, Academic, San Diego, CA **1998**.

[17] D. M. Pozar, *Microwave Engineering*, 2nd ed., Wiley, New York **1998**.

[18] X. M. Cheng, X. K. Zhang, D. Z. Zhang, S. H. Lee, A. Duckham, T. P. Weihs, R. C. Cammarata, J. Q. Xiao, C. L. Chien, *J. Appl. Phys.* **2003**, *93*, 7121.

New, Highly Ion-Conductive Crystals Precipitated from Li_2S–P_2S_5 Glasses**

By *Fuminori Mizuno*, *Akitoshi Hayashi*, *Kiyoharu Tadanaga*, and *Masahiro Tatsumisago**

Rechargeable solid-state batteries have been developed as next-generation high-performance power sources, and in particular, all-solid-state lithium secondary batteries with high energy densities have been intensively investigated. Several solid-state lithium batteries using inorganic glassy electrolytes, such as lithium phosphorus oxynitride (Lipon, $Li_{2.9}PO_{3.3}N_{0.46}$), have been reported to show excellent cell performance over thousands of cycles at room temperature.[1–3] Since inorganic glassy electrolytes are essentially non-flammable, the safety and reliability of batteries incorporating them would be an improvement over commercial lithium-ion batteries containing liquid electrolytes. However, oxide-based glassy electrolytes such as Lipon have to be utilized as thin films to compensate for their low ionic conductivities, and their limited cell capacity is one of the disadvantages of thin-film batteries. Therefore, the development of highly conductive solid electrolytes is imperative to create large-sized, all-solid-state batteries with high capacity.

[*] Prof. M. Tatsumisago, F. Mizuno, Dr. A. Hayashi, Dr. K. Tadanaga
Department of Applied Materials Science, Graduate School of Engineering
Osaka Prefecture University
1-1 Gakuen-cho, Sakai
Osaka 599-8531 (Japan)
E-mail: tatsu@ams.osakafu-u.ac.jp

[**] This work was supported by a Grant-in-Aid for Scientific Research on Priority Areas from the Ministry of Education, Culture, Sports, Science and Technology of Japan. We thank Idemitsu Kosan Co. for supplying the high-purity Li_2S reagent.

DOI: 10.1002/adma.200401286